Technical Report CERC-94-1
January 1994

(2)

US Army Corps
of Engineers
Waterways Experiment
Station

Three-Parameter Characterization of Shallow-Water Directional Wind Wave Spectra

by Charles E. Long
Coastal Engineering Research Center

Prepared for Headquarters, U.S. Army Corps of Engineers

Technical Report CERC-94-1
January 1994

Three-Parameter Characterization of Shallow-Water Directional Wind Wave Spectra

by Charles E. Long
Coastal Engineering Research Center
U.S. Army Corps of Engineers
Waterways Experiment Station
3909 Halls Ferry Road
Vicksburg, MS 39180-6199

Final report

Approved for public release; distribution is unlimited

Prepared for U.S. Army Corps of Engineers
Washington, DC 20314-1000

Under Civil Works Research Unit 32484

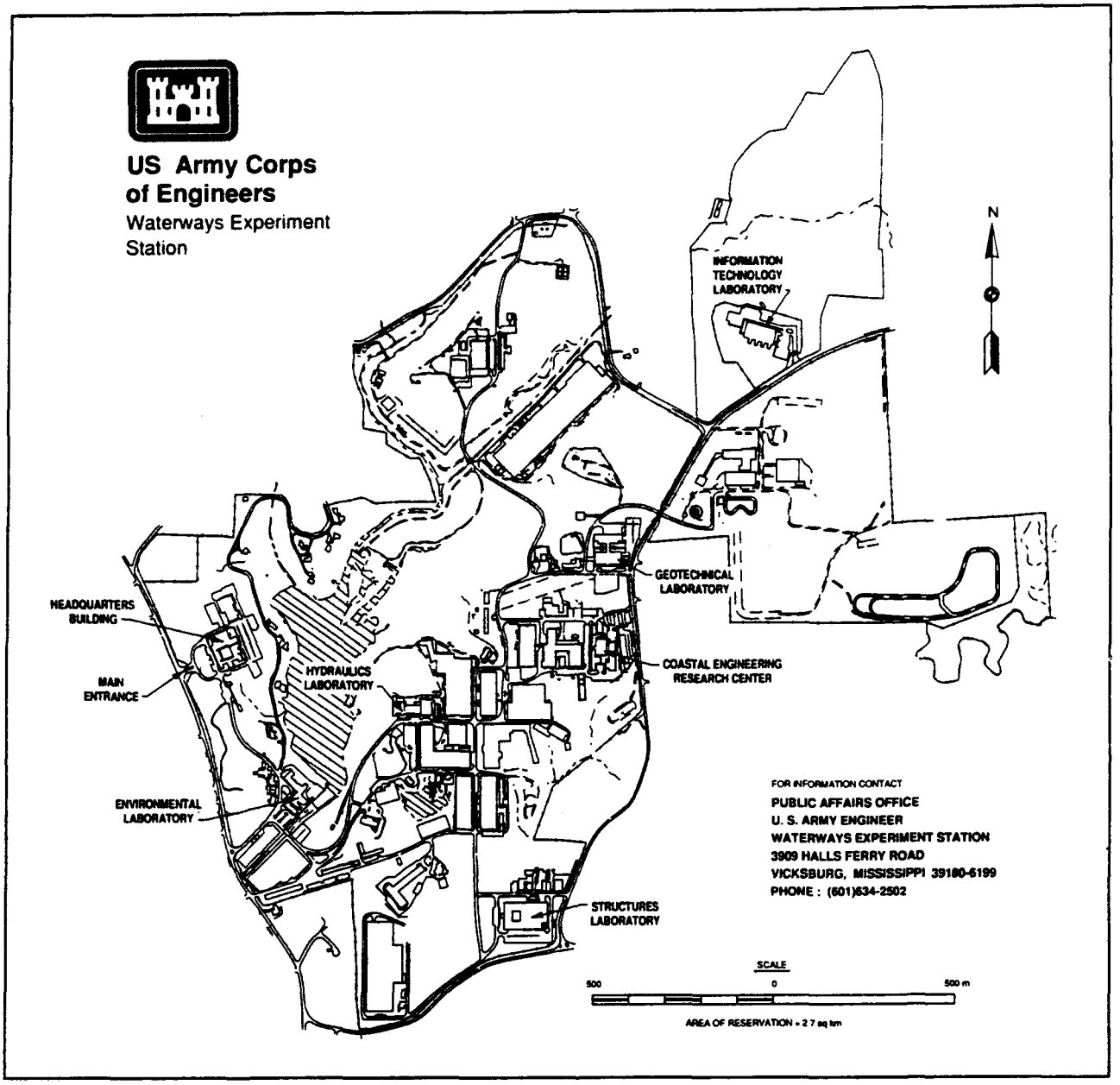

Waterways Experiment Station Cataloging-in-Publication Data

Long, Charles E.
Three-parameter characterization of shallow-water directional wind wave spectra / by Charles E. Long ; prepared for U.S. Army Corps of Engineers.
129 p. : ill. ; 28 cm. — (Technical report ; CERC-94-1
Includes bibliographic references.
1. Ocean waves — Statistics. 2. Wind waves — Statistics. 3. Water waves — Statistics. I. United States. Army. Corps of Engineers. II. Coastal Engineering Research Center (U.S.) III. U.S. Army Engineer Waterways Experiment Station. IV. Title. V. Series: Technical report (U.S. Army Engineer Waterways Experiment Station) ; CERC-94-1.
TA7 W34 no.CERC-94-1

Contents

Preface

This report describes results and some consequences of classifying shallow-water wind wave energy spectra in terms of characteristic wave height, frequency, and direction. The work was motivated by the need to quantify the variability in natural energy distributions when only three parameters are used to define wave conditions. A special, high-resolution directional wave gauge is used for this purpose. This effort was authorized by Headquarters, U.S. Army Corps of Engineers (HQUSACE), under Civil Works Coastal Flooding and Storm Protection Program Research Work Unit 32484, "Directionality of Waves in Shallow Water." Funds were provided through the Coastal Engineering Research Center (CERC), U.S. Army Engineer Waterways Experiment Station (WES), under the program management of Ms. Carolyn M. Holmes, CERC. Messrs. John H. Lockhart, Jr., John G. Housley, Barry W. Holliday, and David A. Roellig were HQUSACE Technical Monitors.

This report was prepared by Dr. Charles E. Long at CERC's Field Research Facility (FRF) in Duck, NC, under the direct supervision of Mr. William A. Birkemeier, Chief, FRF, and Mr. Thomas W. Richardson, Chief, Engineering Development Division, CERC. General supervision was provided by Dr. James R. Houston and Mr. Charles C. Calhoun, Jr., Director and Assistant Director, CERC, respectively.

The directional wave gauge and its data processing software were designed by Dr. Joan M. Oltman-Shay while at Oregon State University working through an Intergovernmental Personnel Agreement. Physical maintenance of the gauge was provided by the FRF dive team consisting of Messrs. Birkemeier, Michael W. Leffler, H. Carl Miller, Eugene W. Bichner, and Brian L. Scarborough. Gauge calibration was maintained by Mr. Kent K. Hathaway, FRF. Data acquisition and storage were performed by Mr. Clifford F. Baron, FRF. This document was edited by Ms. Janean Shirley, Information Technology Laboratory, WES. The contributions of all of these individuals are gratefully acknowledged.

At the time of publication of this report, Director of WES was Dr. Robert W. Whalin. Commander was COL Bruce K. Howard, EN.

1 Introduction

Descriptions of ocean wind wave conditions in coastal engineering studies are often restricted, either by common practice or lack of instrumentation, to time series of three characteristic parameters: a wave height, a frequency associated with the most energetic waves, and a propagation direction that is typical of the most energetic waves. Knowledge of these three parameters for a given time is sufficient to employ a great deal of the guidance in the *Shore Protection Manual* (SPM) (1984), perhaps the most widely referenced treatise on coastal engineering practice. In cases where wind wave energy is concentrated in a narrow band of frequencies and a narrow range of directions, a three-parameter characterization of sea state is reasonable, and engineering computations based on SPM guidance may be considered fair estimates of natural processes. However, it is known from at least one detailed study of shallow-water wind waves that energy is commonly spread over broad ranges of frequency and direction (Long and Oltman-Shay 1991). In these cases, a three-parameter definition of wave conditions is likely to lead to considerable errors in engineering estimates. The intent of this report is to elucidate and quantify some of the possible errors.

Quantification is achieved from high-resolution empirical observations of wind wave frequency-direction energy spectra obtained in shallow water. A set of 6,759 spectra from regular observations over a 5-year time span is classified and grouped by ranges of characteristic wave height, frequency, and direction. The number of constituent spectra in these groups illustrates the variety of spectra in the database and provides some measure of their frequency of occurrence. Properties of the constituent spectra in each group are compared to corresponding properties of a unimodal, monochromatic wave train, which is the fundamental wave field defined by just one height, frequency, and direction. Spectral properties include mean spectral shape, a measure of variability of spectral shape, estimates of longshore energy flux, and estimates of radiation stress tensor components. All of these properties are germane to a definition of nearshore wave climate and to fundamental wave properties used to model wave forces on structures, wave-generated currents, and wave-induced sediment transport.

Because this study is based on empirical observations from a single site, it is emphasized strongly at the outset that all quantification is specific to that single site. Conclusions reached here can be applied qualitatively to other

sites having comparable geometries and boundary conditions, but should not be construed to be universally applicable to all sites.

This report is organized into six chapters. Chapter 2 describes the experiment site, the directional wave gauge, the spectral classification scheme, and the distribution of constituent spectra among the classes. Chapter 3 describes characteristic spectral shapes and their variability within classes. Chapter 4 shows comparisons of estimates of longshore energy flux from constituent directional spectra and from corresponding unidirectional wave trains for each of the classes. Chapter 5 does a similar analysis for estimates of components of the radiation stress tensor. Chapters 4 and 5 both discuss quantifiable bias errors and the magnitudes of residual errors that occur when a three-parameter definition of sea state is used. Chapter 6 summarizes salient results and makes suggestions for future work.

Though this report emphasizes differences in certain computations when two forms of sea state description (complete spectrum versus three parameters) are used, it also provides one form of reduction of a rather large spectral database into meaningful classes of spectral shapes. These shapes represent energy distributions that are of use to nearshore modelers seeking boundary conditions for nearshore wave transformation processes or the results of nearshore wave generation processes. As discussed in Chapter 3, rather distinctive spectral shapes arise from this analysis that suggest important surf zone processes during periods of high wave energy.

2 Data Set

Experiment Site

Data used in this study were acquired at the Field Research Facility (FRF) of the Coastal Engineering Research Center (CERC), U.S. Army Engineer Waterways Experiment Station. The FRF is located on the Outer Banks of North Carolina near the village of Duck (Figure 1). The layout, function, and capabilities of the FRF are described by Birkemeier et al. (1985). Of relevance to this study are the continental shelf bathymetry, which acts to steer the waves that propagate across it, and the general nature of the local wind climate, which generates the higher-frequency waves observed at this site.

As shown in Figure 1, the coastline in the vicinity of the FRF is nearly straight for several tens of kilometers north and south. It is oriented such that a shore-normal line (directed seaward) is very nearly 70 deg from true north. Waves and onshore winds can approach this site along an easterly 180-deg arc from 340 deg to 160 deg true. The adjacent continental shelf is wide, relatively shallow, and of somewhat complex bathymetry. The direction of nearest approach of the 100-m isobath (approximately the 50-fathom line in Figure 1), which indicates the shelf break, is approximately due east, or about 20 deg south of the shore-normal line, and about 80 km distant. Long wind waves and swell generated in the deep Atlantic Ocean tend to refract at the shelf break and approach the FRF site from this direction. A typical bottom slope for the shelf is 1 m/km, but this is interrupted by numerous features of 1- to 10-km horizontal scales and 10-m vertical scales positioned irregularly across the shelf. These features act primarily through refraction as wave scattering lenses, and may account for some of the broad directional spreading observed at this site (Long and Oltman-Shay 1991).

The site is subject to a variety of wind conditions, which give rise to a diverse set of directional wave conditions. Windless days are rare. Light winds with speeds less than about 10 m/sec are very common, and produce short, high-frequency waves of low intensity, usually on a likewise low-intensity background swell arriving from the deep Atlantic. For the data set used in this study, the primary source of high-energy waves is the wind associated with passing fronts, many of which have embedded low-pressure cells. Frontal systems are usually oriented northeast-southwest and migrate from west to east. Frontal winds thus tend to begin by blowing from the southwest, and then shift to the northeast as the front passes. Though the southwest winds

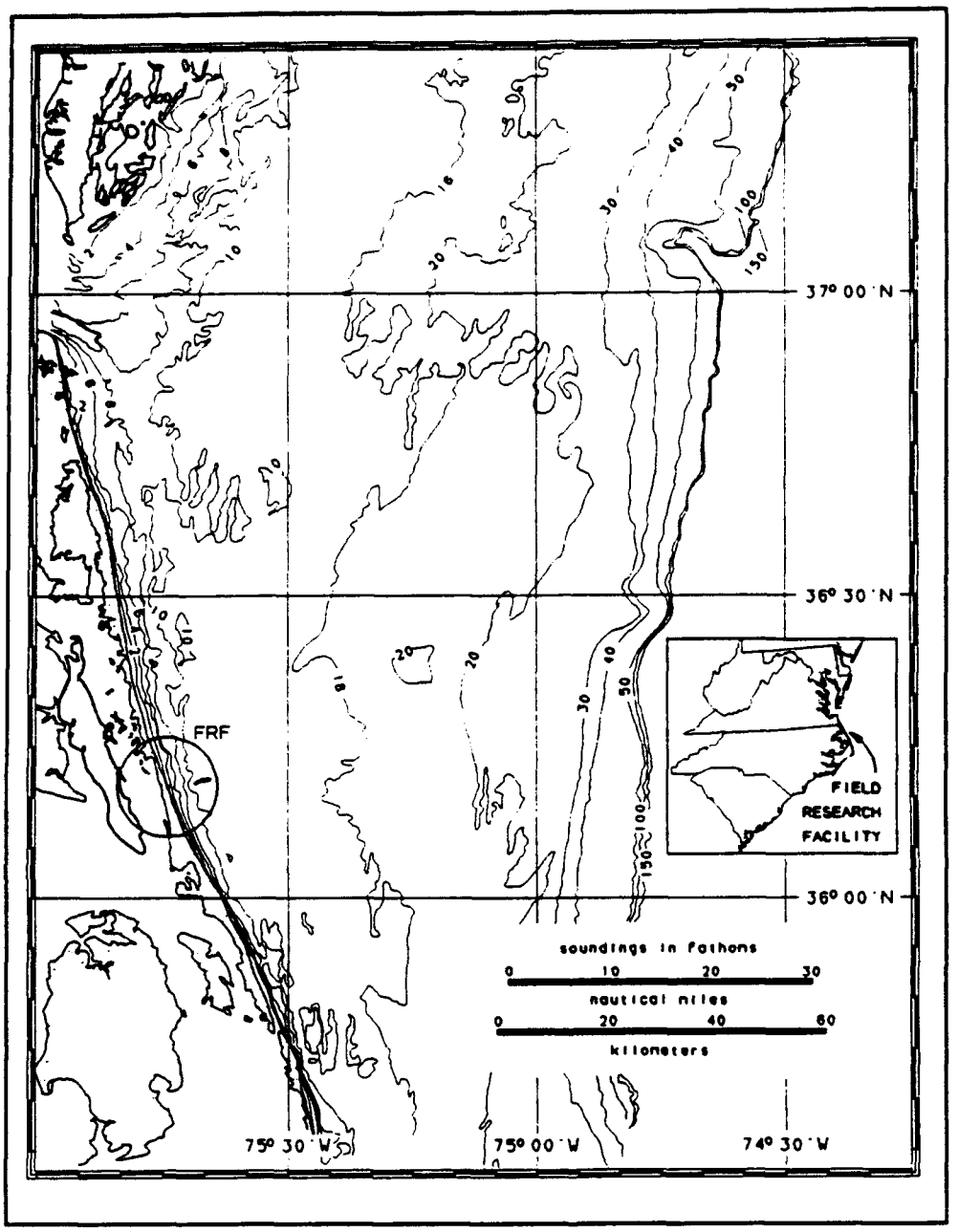

Figure 1. FRF location and offshore bathymetry

have an offshore blowing component that tends to oppose arriving waves, there is also a southerly component that generates waves propagating northward along the coast. The shallow nearshore bathymetry tends to refract these waves onshore. Consequently, newly generated waves from the southeast are frequently observed when a frontal system approaches the FRF site.

Another source of high-energy waves is the long-period, well-sorted swell that radiates from distant hurricanes. Though no hurricanes passed over the FRF during the period of this study, several made landfall well south of this site and others have migrated northward past this site, but well offshore.

These waves are distinguished from those associated with fronts in that wave energy is distributed over narrow ranges of frequency and direction.

Directional Wave Gauge

The primary instrument used in this study is a high-resolution, linear array directional wave gauge. It consists of two parts: an array of sensors that sample sea-surface displacement at several points in (horizontal) space and an algorithm that converts these data into estimates of the frequency and directional distribution of wave energy. The array consists of nine pressure gauges mounted near the bottom along the 8-m isobath about 900 m offshore and to the north of the FRF research pier (Figure 2). Spacing between the gauges follows the array-design guidance of Davis and Regier (1977). The 8-m water depth is shallow enough that relatively noise-free wave signals can be detected up to a frequency of about 0.32 Hz. Waves of that frequency in 8 m of water have a wavelength of about 15 m. The minimum gauge spacing in the array is 5 m and spacings increment in units of 5 m, so that these high-frequency waves are well-sampled. The overall length of the array is 255 m.

Signals from each of the pressure sensors are sampled at 2 Hz for 2 hr 16 min (16,384-point data records). Pressure signals are windowed in 15 half-lapped segments of 17 min duration and then digitally Fourier transformed to the frequency domain. Transformed pressure record segments are converted to transformed sea-surface displacement record segments out to the 0.32-Hz cut-off frequency using the pressure response function of linear wave theory. Raw cross-spectral estimates for each unique pair of gauges are then computed for each segment. Smooth cross-spectral estimates are computed by averaging over the 15 segments and then further averaging over 10 adjacent frequency bands. The final discrete frequency bandwidth is 0.00977 Hz and each smoothed cross-spectral estimate has about 200 degrees of freedom following Welch's method as described by Oppenheim and Schafer (1975).

Wave energy directional distributions are found by forming a matrix of cross-spectral estimates for each discrete frequency band and then applying the Iterative Maximum Likelihood Estimation (IMLE) algorithm derived by Pawka (1982, 1983) as a refinement to the ocean wave Maximum Likelihood Estimation method described by Davis and Regier (1977). The convergence parameters used by Pawka (1983) were used here identically. There is no formal estimate of error for IMLE, and tests of verity must be done on a case-by-case basis with synthetic data. Preliminary tests of the FRF array indicate that peaks of directional distributions can be resolved to within about 5 deg and that spectral estimates within a directional distribution vary with a standard deviation of about 30 percent when subjected to random noise appropriate for 200 degrees of freedom. Energy estimates for this study were computed in discrete, 2-deg arcs for the full 180-deg wave approach horizon.

The final result of these computations is a regular gridded array of wave energy density as a function of discrete frequency and direction. The frequen-

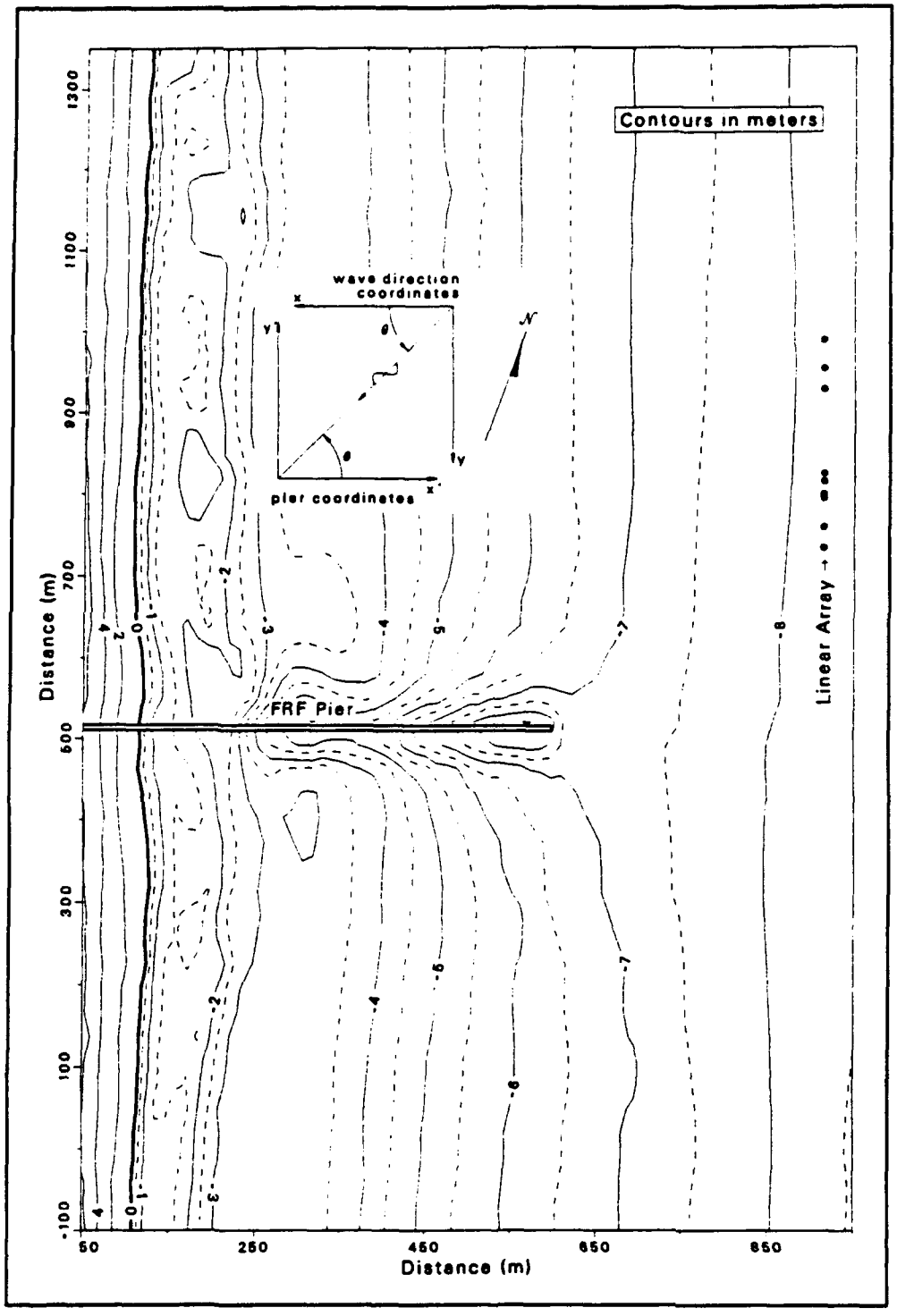

Figure 2. FRF linear array and nearshore bathymetry

cy dimension is in 28 bands of width 0.00977 Hz covering the general wind wave frequency range of 0.05 to 0.32 Hz. The direction dimension is in 91 discrete bins of 2-deg width covering the 180-deg range of incident wave approach angles. One of these arrays is generated each time a data acquisition process known as a collection occurs.

Data collection at the FRF occurs at least four times daily, at 0100, 0700, 1300, and 1900 Eastern Standard Time (EST). At times of high energy, typically when characteristic wave heights exceed 2 m, additional collections occur at 0400, 1000, 1600, and 2200 EST. With the exception of the first two months, this collection pattern was followed for the full duration of this data set, extending from September 1986 through August 1991. September and October 1986 were the months of the SUPERDUCK experiment (Crowson et al. 1988), during which time collections were 3 hr 59 min in duration, centered at times of high and low tide. For the frequency-direction spectra, these long records were processed as two collections of 2 hr 16 min, with an overlapping 34 min of data shared between the two collections.

Excepting occasional breaks for array maintenance and repair, and two gaps of several months, data coverage was continuous. One gap, from November 1986 to January 1987, occurred after SUPERDUCK and is omitted from this analysis because data collections were reduced to 34 min in duration, too short to be statistically consistent with the longer records used in the bulk of this study. The second gap extended from December 1987 through August 1988, beginning when a fleet of fishing trawlers seriously damaged the array and ending after repair parts were obtained and sufficient fair weather was available for extensive diving operations.

Altogether, the working data set used in this study consists of 6,759 discrete frequency-direction spectra. Because part of this study involves grouping and averaging various members of this data set, it is noted that some aliasing will be present due to the data gaps and the odd sampling pattern during SUPERDUCK. Aliasing in this context means that the time axis of the sampling is not uniform. Consequently, some classes of spectra may be over- or under-represented. This condition is considered acceptable for this preliminary study where the intent is to employ the maximum possible number of observations. Additional aliasing by higher sampling rates during high wave conditions is not a problem in this study because wave height is one of the grouping parameters and the 2-m criterion for higher sampling occurs at one of the height class boundaries.

Parameter Definitions

The main objective of this study is to classify and group the observed spectra by characteristic wave height, period, and direction. Many ways to define representative parameters with these names are found in the literature, especially where frequency-direction spectra are used. The specific parameters used in this study are defined here.

Figure 3 is representative of spectra obtained from the FRF array. The three-dimensional surface depicts the discrete frequency-direction spectrum

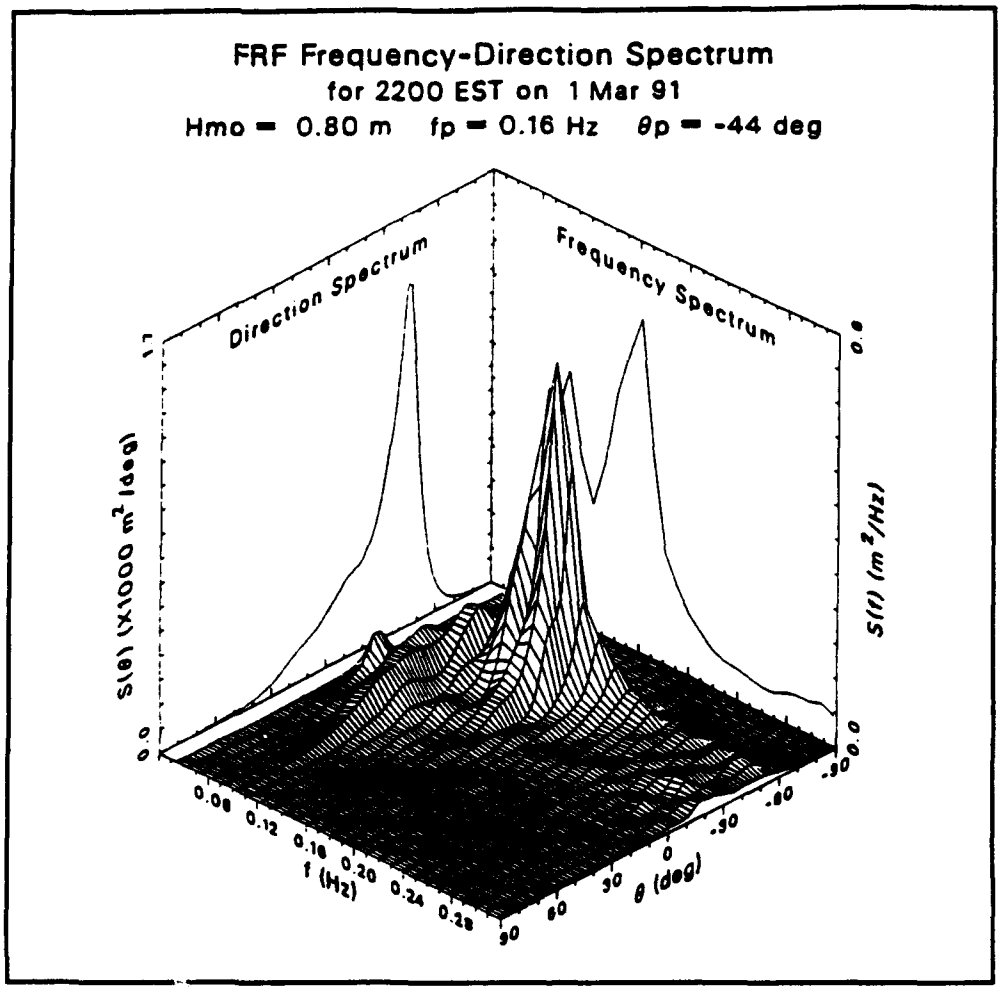

Figure 3. Representative frequency-direction spectrum

denoted[1] $S(f_n,\theta_m)$, where f_n is the n^{th} of $N = 28$ discrete frequencies (f) that increment in units of $\Delta f = 0.00977$ Hz, and θ_m is the m^{th} of $M = 91$ discrete directions that increment in units of $\Delta\theta = 2$ deg. Direction is defined such that θ represents the direction from which waves arrive, measured counterclockwise from shore-normal. The frequency spectrum in the right panel of Figure 3 is the conventional spectrum that one would obtain with data from a single wave staff or surface-corrected pressure gauge. The frequency spectrum is related to the frequency-direction spectrum by

$$S(f_n) = \sum_{m=1}^{M} S(f_n,\theta_m)\,\Delta\theta \qquad (1)$$

[1] For convenience, symbols and abbreviations are listed in the notation (Appendix D).

The direction spectrum in the left panel of Figure 3 is the directional analogue of the frequency spectrum, representing the total energy in each direction bin. The direction spectrum is related to the frequency-direction spectrum by

$$S(\theta_m) = \sum_{n=1}^{N} S(f_n,\theta_m)\ \Delta f \tag{2}$$

Because the frequency-direction spectra are to be classified, characteristic parameters representing wave height, frequency, and direction are deduced from the three-dimensional part of Figure 3.

Wave height

In this study, characteristic wave height is the conventional energy- or spectrum-based height H_{mo}. It is defined as

$$H_{mo} = 4\sigma \tag{3}$$

where σ is the standard deviation of sea surface displacement, which is the square root of the variance of sea surface displacement within the bounding frequency and direction limits employed in spectral computation. In terms of the frequency-direction spectrum, the variance is

$$\sigma^2 = \sum_{n=1}^{N} \sum_{m=1}^{M} S(f_n,\theta_m)\ \Delta\theta\ \Delta f \tag{4}$$

Frequency

Characteristic frequency f_p is defined here as the frequency associated with the peak or maximum value of $S(f_n,\theta_m)$. A more conventional definition is the frequency associated with the peak of $S(f_n)$, primarily because there are many more observations of frequency spectra than of frequency-direction spectra. These two peak frequencies can differ if wave energy is concentrated near some direction at one frequency and more directionally spread at a second frequency. If the frequency spectrum shows equal amounts of energy at these two frequencies, the frequency-direction spectrum will show a stronger peak at the first frequency, and $S(f_n,\theta_m)$ will be classified with f_p equal to the first frequency.

This distinction is important because the more conventional definition of f_p would associate the frequency-direction spectrum with the second frequency, and would subsequently alter statistical properties of groups of spectra identified by classes of frequency. The definition of f_p used in this study is justi-

fied, however, because similarities in shapes of the three-dimensional spectra are sought here. The frequency for which energy is most concentrated in the three-dimensional spectrum is thus the appropriate parameter. It is also most appropriate in engineering studies where directionality and groupiness properties are included, because waves of extreme height are more likely to occur at this frequency.

Direction

In the same manner and for the same reasons as characteristic frequency is defined, characteristic direction θ_p is identified as the direction at which $S(f_n,\theta_m)$ is a maximum. It is noted that in some numerical models, like CERC's Wave Information Studies (Corson, Resio and Vincent 1980), and in the treatment of data from some low-resolution directional wave gauges (Howell 1992), a characteristic direction is identified as the mean direction, which is the zeroth moment of a directional distribution function, usually that occurring at the frequency of the peak of $S(f_n)$. This second definition can vary, sometimes dramatically, from the θ_p used in the present study, but, again, the present definition is simpler and assures that constituent spectra in a direction class all have the greatest concentration of energy at the same direction. It is likely that future studies, involving model testing or gauge intercomparisons, will consider mean direction as a characterizing parameter.

Classification Scheme

With the characteristic parameters defined, the complete set of frequency-direction spectra can be classified in a parameter space having axes (H_{mo},f_p,θ_p), and statistical properties of constituent spectra within a class can be computed. To gain statistical confidence, and to maintain a reasonable overall number of resulting classes, the full ranges of each of the three parameters are subdivided into small numbers of intervals so that any spectrum can be identified with a specific height, frequency, and direction class.

Height classes

Within the present data set, H_{mo} varied from 0.15 m to 4.70 m. Two constraints affect how wave height class boundaries are defined. First, it is wave energy that a spectrum represents, so that classification should be by energy content, which varies as H_{mo}^2, and not just wave height. Second, there are far more observations at small H_{mo} than at large, suggesting that class boundaries should be closer together at small wave heights to get a more even number of cases in each of the height classes. Both of these constraints are satisfied by using a geometric distribution of class boundaries instead of a simple linear distribution.

A geometric distribution means that the ratio of one height class boundary to the previous height class boundary is constant. When squared to represent energy, this scheme results in a constant percentage change of energy across all classes. In this study, eight height classes were used. The geometric distribution results in nine height class boundaries, at H_{mo} = 0.15, 0.23, 0.35, 0.55, 0.84, 1.29, 1.99, 3.06, and 4.70 m. As noted before, one of the boundaries occurs very near to 2 m so that some of the biasing effects of higher spectral sampling above this wave height are isolated to the two highest wave height classes.

Frequency classes

All spectra were defined in terms of 28 discrete frequency bands ranging from about 0.054 Hz to about 0.318 Hz. This range is divided into seven classes, each having a nominal bandwidth of about 0.04 Hz. All classes contain four possible discrete peak frequencies except the lowest-frequency class, which contains only three. The class boundaries occur at f = 0.054, 0.083, 0.122, 0.161, 0.200, 0.240, 0.279, and 0.318 Hz. For plotting purposes, the classes are identified by nominal band-center frequencies of 0.06, 0.10, 0.14, 0.18, 0.22, 0.26, and 0.30 Hz.

Direction classes

The 180-deg arc that represents the possible range of θ_p is divided into 19 bins. Each bin, except the first and last, has a range of 10 deg, and is centered on an azimuth that is an integer multiple of 10 deg from shore-normal. The first and last bins only have ranges of 5 deg because they terminate at 90 deg and -90 deg, respectively. The bin boundaries thus follow the pattern 90 deg, 85 deg, 75 deg, 65 deg,..., 5 deg, -5 deg,..., -65 deg, -75 deg, -85 deg, -90 deg. For plotting purposes, direction classes are assigned nominal values of 90, 80, 70,..., 10, 0, -10,..., -70, -80, and -90 deg. Though the first and last bins are only 5 deg wide, it turns out that no spectra fall into those classes, so the analysis is not compromised.

Class Distribution of Spectra

With eight wave height ranges, seven frequency ranges, and nineteen direction ranges, there are a total of 1,064 possible classes with which to characterize the 6,759-case spectral database. If these spectra were uniformly distributed across all possible classes, there would be roughly six cases per class, enough to do some simple statistics. Of course, the spectra are not distributed uniformly, so it is of interest to see how the spectra are distributed. If the total number of spectra that fall into a given class is divided by the total number of cases in the database and multiplied by 100 percent, a set of empirical distribution functions can be computed.

Figure 4 is one way to display the three-dimensional distribution of cases in the wave height, peak frequency, and peak direction domains. There is one subplot for each wave height class. Within each subplot is a three-dimensional surface that shows as a percentage the number of all cases that fall into a particular frequency and direction class. The header for each subplot shows the percentage of all cases that fall into the corresponding wave height class. Side panels in each subplot show percentages of all cases associated with a particular frequency class (right panels) or direction class (left panels) within a wave height class. All parts of all subplots are drawn to the same scale.

The wave height class with the lowest energy has too few cases to be visible at the scale shown, but also represents so little energy as not to be important dynamically. The next three wave height classes show two important features of the wave climate at the FRF. One is the pervasive, low- to mid-frequency swell that tends to arrive from south of shore-normal (negative peak directions), suggesting generation somewhere in the deep Atlantic and refraction at the shelf break (Figure 1). The pervasiveness is reflected in the high percentage of cases represented by these classes. The other feature is the set of spectra associated with the initial stages of wind wave generation. These cases tend to have peaks at middle to high frequencies and are distinguished by having high approach angles from both the north (initial stages of northeasterly storms) and the south (possibly refracted waves generated by the southwesterly winds of approaching fronts). Spectra with high frequency peaks very seldom occur at near-normal incidence.

At still higher energies, there are three dominant characteristics. First, there are very few high-frequency peaks, indicating continued sea-state growth. Second, there are fewer peak directions in the southerly quarter, showing the increasing dominance of northeast winds in wave generation. Third, the most frequent cases are of low peak frequency and more centered at shore-normal incidence, indicating the presence of refracted, locally generated long waves. The two classes containing the highest wave heights do not contain a high percentage of cases, but are very important dynamically because they represent the peak conditions of storms that incur great changes to nearshore bathymetry, increased beach erosion, and structural damage. These two classes are characterized by low-frequency peaks at normal to slightly north of normal incidence.

This simple interpretation of the distribution surfaces of Figure 4 is consistent with identifiable physical processes, and suggests that meaningful insight can be gained by a three-parameter characterization of frequency-direction spectra. However, it is far from complete. Considerable variation in the structure of spectral shapes within a wave height, peak frequency, and peak direction classification is quite probable. These variations can be very important dynamically, so the next step is to examine frequency-direction spectral shape within individual three-parameter classifications.

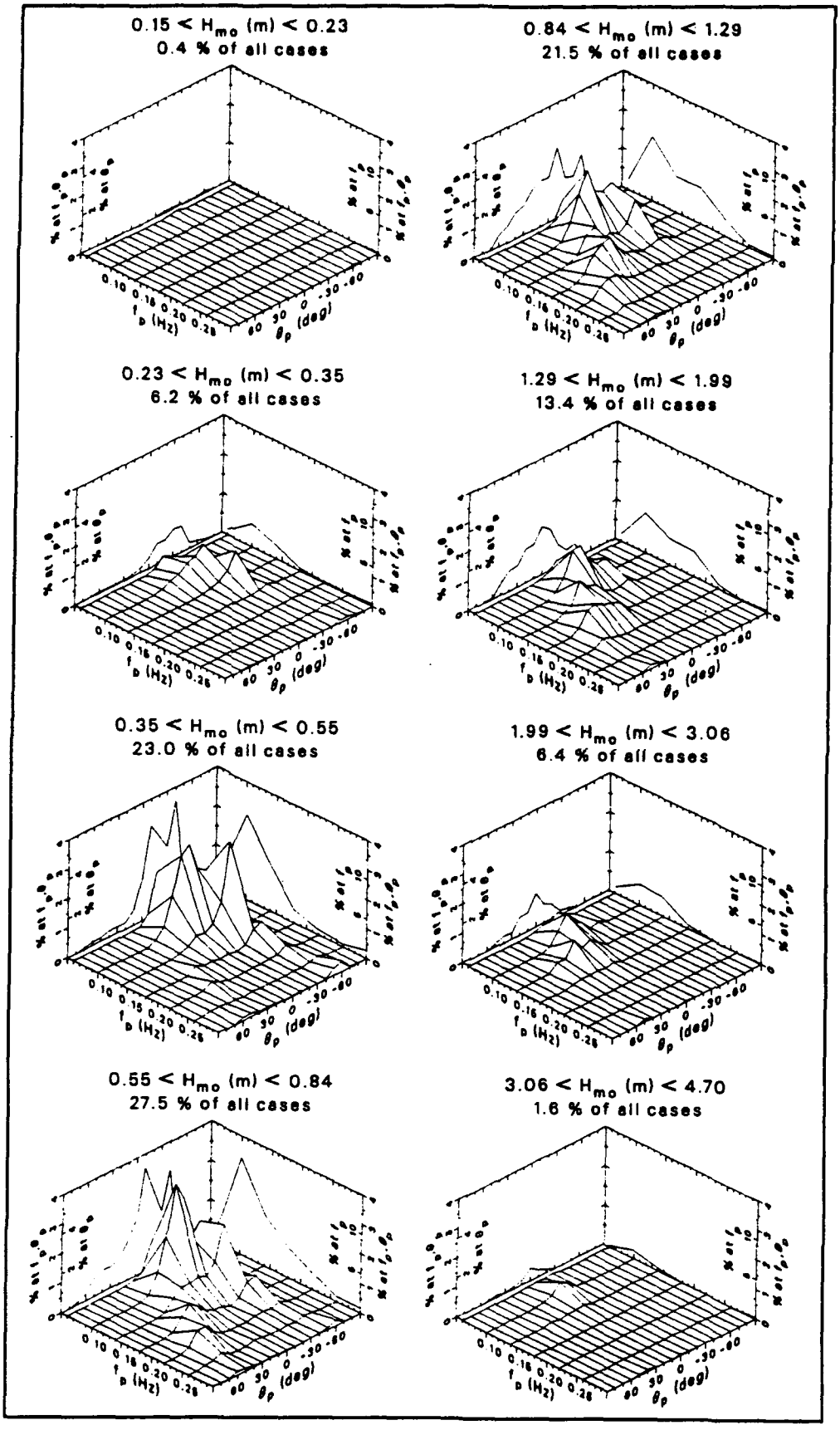

Figure 4. Distribution of spectral cases in parameter space

3 Characteristic Spectra

More insight into spectral structure beyond the gross climatological interpretation afforded by simply counting cases is gained by examination of statistical properties of constituent spectra within each wave height, peak frequency, and peak direction class. Of particular interest are the frequency and directional energy distributions that are typical or characteristic of each classification. The goal is to provide meaningful definitions of characteristic spectra as whole entities, thus extending the work of Long and Oltman-Shay (1991), who examined only the first year of data, and who looked only at directional distributions of energy independently of the frequency-direction spectral context from which they came.

Mean Spectra

Perhaps the easiest way to obtain a characteristic spectrum from a set of constituent spectra is to compute an average spectral density for each frequency band and direction bin in the frequency-direction plane. If there are K constituent spectra in a particular height-period-direction class, a first attempt at an average spectrum $\bar{S}(f_n,\theta_m)$ can be defined mathematically as

$$\bar{S}(f_n,\theta_m) = \frac{1}{K}\sum_{k=1}^{K} S_k(f_n,\theta_m) \tag{5}$$

where $S_k(f_n,\theta_m)$ is the k^{th} constituent spectrum in the class.

If a mean spectrum can be computed, it is reasonable that some measure of variability, such as the standard deviation, can also be computed. Variability among constituent members of a class of spectra can arise from two primary causes. One cause is variation in spectral shape from such properties as secondary spectral peaks or the amount of directional spread. The other cause is variation in energy content. Even though constituent spectra are classified by energy content by way of H_{mo}, there is a finite range of energies within a class. Because of the geometric spacing of height class boundaries, the total energy, which is proportional to H_{mo}^2, can vary by a factor of about 2.4 across

one height class. The present interest is in variability of spectral shape, so it is desired to minimize the influence of energy content in the analysis. One way to isolate spectral shape from energy content is to normalize each constituent spectrum by its own volume, which, by Equation 2, is the variance of sea surface displacement σ^2. Normalized spectra are defined by

$$S_k'(f_n,\theta_m) = \frac{1}{\sigma_k^2} S_k(f_n,\theta_m) \tag{6}$$

where σ_k^2 is the variance contained in the k^{th} constituent spectrum in a class. Normalized spectra are dimensionless and have unit volume, so that comparing normalized spectra emphasizes spectral shape, as desired. Note that by Equations 3 and 4, $\sigma_k^2 = H_{mo,k}^2/16$, where $H_{mo,k}$ is the characteristic wave height associated with the constituent spectrum $S_k(f_n,\theta_m)$.

The remainder of the analysis discussed in this report will be based on normalized spectra. Though the normalized spectra are individually independent of energy content, classification by characteristic wave height is retained because, as will be seen, spectral shapes associated with low energy are distinctively different from those with high energy.

The mean of a set of K constituent normalized spectra within a class is

$$\overline{S'}(f_n,\theta_m) = \frac{1}{K} \sum_{k=1}^{K} S_k'(f_n,\theta_m) \tag{7}$$

Standard Deviation Spectra

To show the variability in spectral shape, a standard deviation is computed for each frequency band and direction bin of the constituent spectra. From K normalized spectra, the result is a standard deviation spectrum $S_\sigma'(f_n,\theta_m)$ computed following the conventional definition of standard deviation by

$$S_\sigma'(f_n,\theta_m) = \sqrt{\frac{\sum_{k=1}^{K} S_k'^2(f_n,\theta_m) - K\overline{S'}^2(f_n,\theta_m)}{K-1}} \tag{8}$$

Computation of a standard deviation requires a set of more than one constituent spectrum. In this study, mean and standard deviation spectra are computed only for those classes having at least three constituent spectra. Consequently, some of the very sparsely populated classes are eliminated.

The standard deviation spectrum is a surface that shows variability of normalized spectral densities as a function of frequency and direction. A useful parameter that gives a bulk measure of spectral variability is the volume of the standard deviation spectrum V_σ defined by

$$V_\sigma = \sum_{n=1}^{N} \sum_{m=1}^{M} S'_\sigma(f_n,\theta_m)\ \Delta\theta\ \Delta f \qquad (9)$$

When V_σ is small, the volume of the standard deviation spectrum is small, and the interpretation is that the constituent spectra making up the mean spectrum are all rather alike. When V_σ is large, the volume of the standard deviation spectrum is large, suggesting that the constituent spectra have rather different shapes.

Sample Case

Figure 5 illustrates the mean (upper graph) and standard deviation (lower graph) spectra for one of the height-frequency-direction classes, the bounding parameters for which are shown in the plot header. Representative frequency and direction spectra, computed using Equations 1 and 2, respectively, are shown in the side panels of the plots.

The mean spectrum in Figure 5 is characterized by a broad, rather skewed directional distribution near the peak frequency, and narrow, relatively low-energy directional distributions at the higher frequencies. This shape, which is the mean or expected shape from 95 constituent spectra, is only grossly approximated by a unidirectional, monochromatic wave field having the same peak frequency and peak direction. A unidirectional, monochromatic wave field would be represented in spectral form in Figure 5 as a spike having unit volume with base dimensions $\Delta f \times \Delta\theta$ centered at the peak frequency and peak direction of the mean spectrum. Lacking other knowledge beyond the height, period, and direction characterizing parameters, a unidirectional, monochromatic spectrum would be the only way to represent this class of spectra. As will be seen in Chapters 4 and 5, direction sensitive wave processes, such as energy flux and radiation stress, tend to have very different values when computed from a unidirectional, monochromatic spectrum as compared to a representative mean spectrum like that shown in Figure 5.

Of some concern is the size and shape of the standard deviation spectrum shown in Figure 5. Both the mean and standard deviation spectral graphs are drawn to the same scales, and it is evident that the standard deviation spectrum is shaped somewhat like the mean spectrum and is about the same size, as can be seen visually and as measured by V_σ, which is slightly larger than unity. It would be preferred that the standard deviation spectrum be small at all frequencies and directions, indicating that the mean spectrum is clearly representative of its class, but this evidently is not the case here.

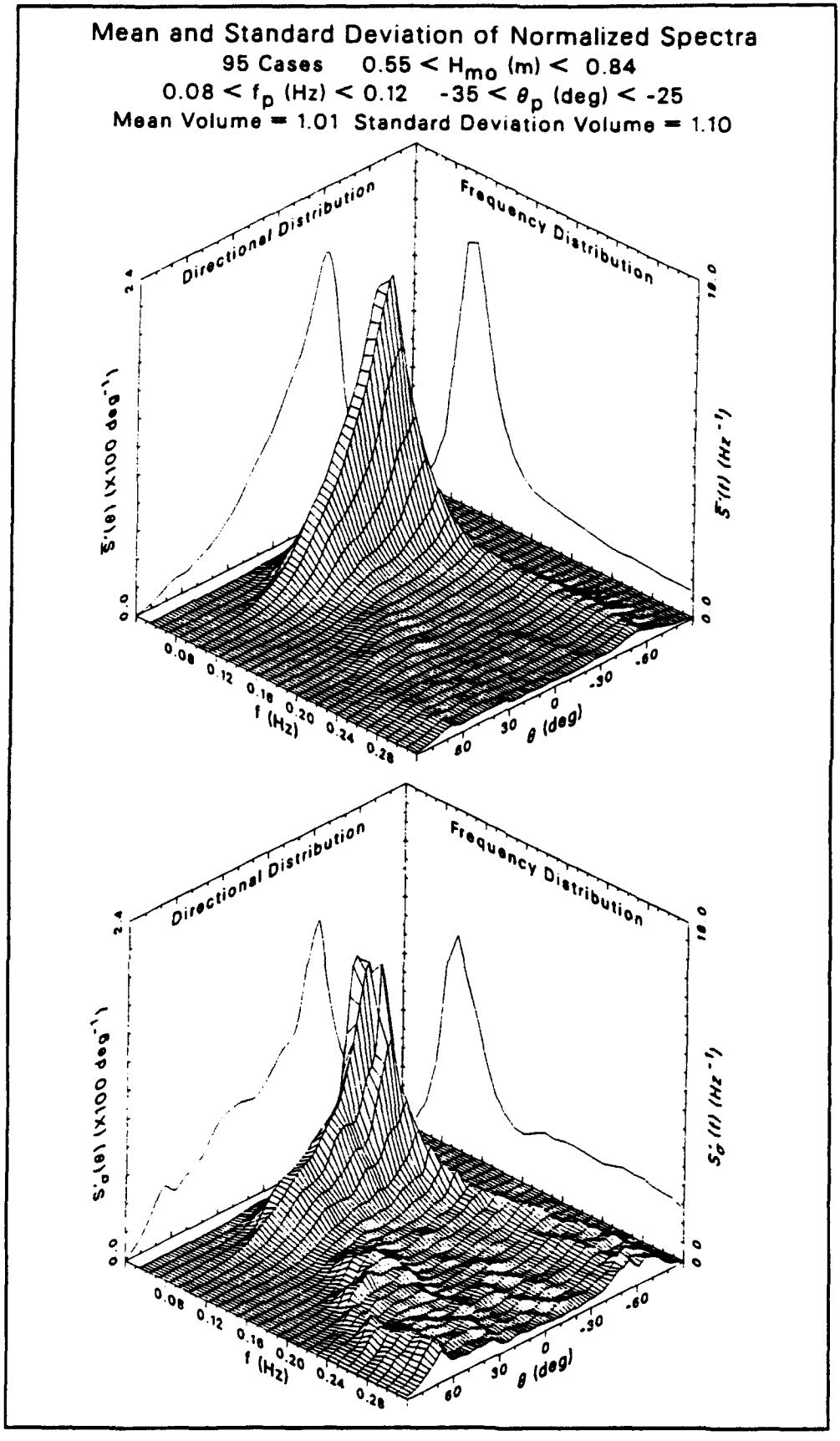

Figure 5. Examples of mean and standard deviation spectra

There are two probable main reasons why the standard deviation spectrum is so large. One reason is that there may be constituent spectra having the general shape of the mean spectrum in Figure 5, but displaced slightly along the frequency or direction axes within the bounding frequencies and directions of the classification scheme. In the classification used here, each direction class encompasses five of the discrete direction bins that define a constituent spectrum, and the peak direction of a constituent spectrum could fall in any one of those five bins. Likewise, the frequency classes include four discrete frequency bands that define a constituent spectrum, and the peak frequency of a constituent spectrum could reside in any one of those bands. Collectively, within a class, there are 20 possible unique frequency-direction locations that could represent a constituent spectral peak. When the constituent spectra are steep-sided, the standard deviation computation could involve a number of small values and a number of large values, depending on how the constituent spectral peaks are distributed in the class ranges of frequency and direction, and this can give rise to a large standard deviation. When this reason is the cause of a large standard deviation, the resulting mean spectrum is a quite reasonable representation of the constituent members, being somewhat smoother and of slightly broader spread, but still retaining the fundamental constituent shape.

The other reason is that the constituent spectra may have significant structural differences that are not reflected by the characteristic frequency and direction designations. These differences may include broad versus narrow directional or frequency distributions of energy, or the existence of significant secondary peaks or side lobes in some of the constituent spectra that are lacking in others. This type of behavior can be severe in that the mean spectrum does not represent any one of the constituent spectra very well.

That both reasons are extant in the present analysis is made evident by Figure 6, which shows, in somewhat compact form, 12 of the 95 constituent spectra that make up the mean and standard deviation spectra of Figure 5. Most of the individual spectra in Figure 6 have broad, somewhat skewed directional distributions near the low-frequency peaks and at least the beginnings of directionally narrow, high-frequency tails, like the mean spectrum of Figure 5. However, the top, left-most spectrum clearly has secondary structure in the forms of a secondary peak at a frequency and a direction well away from the primary peak used to classify this case, and a low-energy, high-frequency tail along a set of directions that are very different from those of the high-frequency tail predominant in the mean spectrum of Figure 5. Clearly, the mean spectrum of Figure 5 does not represent this case as well as it does the other cases shown in Figure 6.

One way to deal with this problem is to make further distinctions about details of spectral structure, essentially by adding classifications for such things as characteristic directional spread and number of dominant modes, and redoing the analysis. Such a procedure is beyond the scope of the present enterprise, however, because the effort here is to ascertain some of the consequences of a three-parameter characterization of frequency-direction spectra. The present problem is one such consequence; averages of constituent spectra

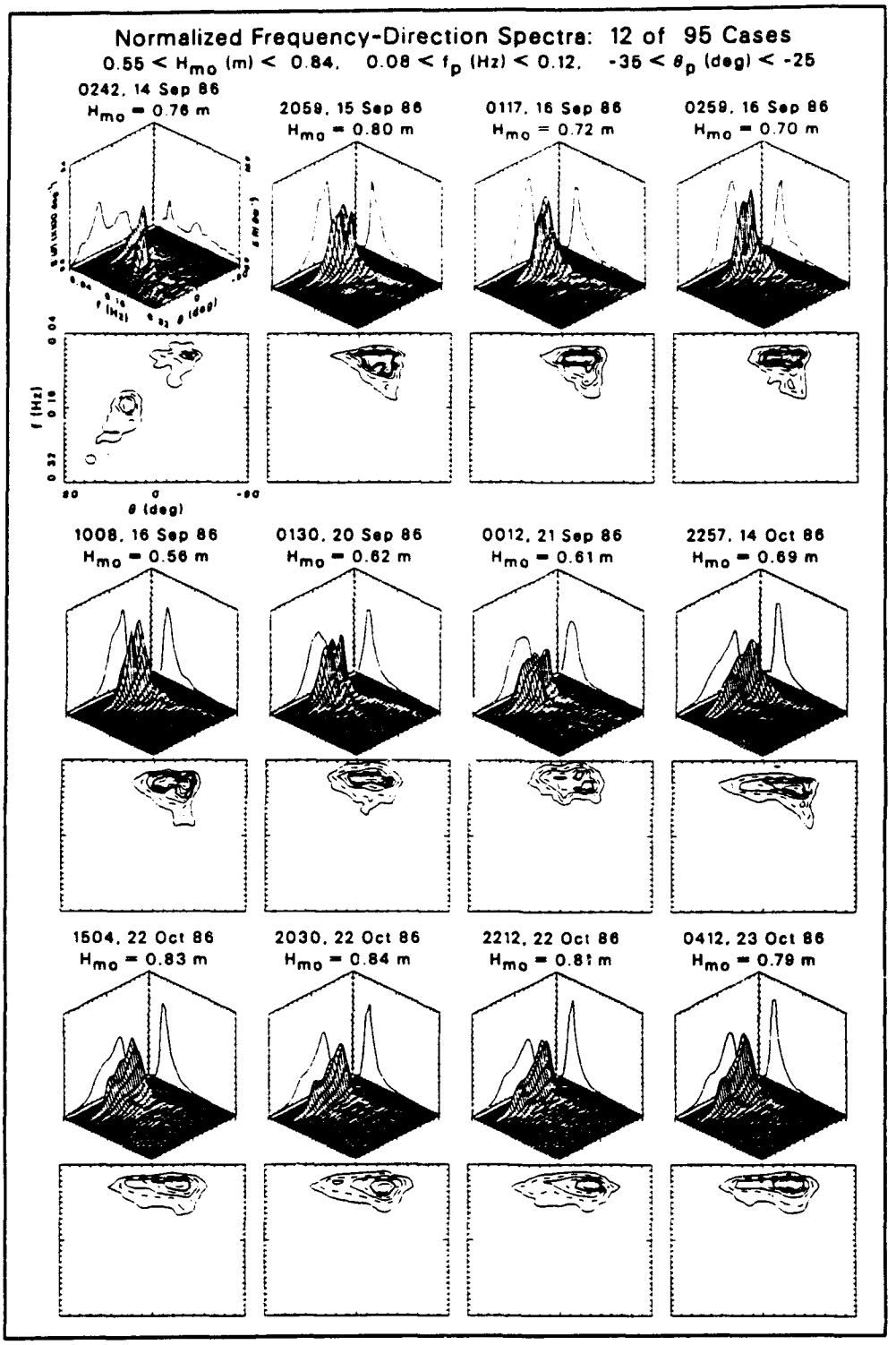

Figure 6. Some constituent spectra for the class shown in Figure 5

within height-frequency-direction classes to construct a spectrum characteristic of the class may not represent some of the constituent spectra very well. Nonetheless, the mean spectra, being derived from measured spectra, are probably better representations of constituent spectra than are unidirectional,

monochromatic spectra. A quantification of this statement is computed for some specific applications in Chapters 4 and 5.

General Set of Classes

The behavioral properties described for the single class of spectra represented by Figures 5 and 6 are common to all of the spectral classes analyzed in this study. Mean spectra for all classes having at least three constituent spectra are illustrated in Appendix A. Corresponding standard deviation spectra are illustrated in Appendix B. The variability of constituent spectra as expressed by the volumes of the standard deviation spectra V_σ is illustrated for all classes in Figure 7. Empty classes, those having fewer than three constituents, are plotted as having $V_\sigma = 0$ in Figure 7.

For classes that are not empty, Figure 7 shows that the V_σ are all of order one, ranging from about 0.3 to about 1.1, and tend to be largest for spectra with low peak frequencies in intermediate wave height classes. The examples of mean, standard deviation, and constituent spectra shown in Figures 5 and 6 represent a case where V_σ is large. Of interest is the character of a class where V_σ is smaller.

High-Energy Case

Figure 8 illustrates the mean and standard deviation spectra for a class where V_σ is about half that for the class illustrated in Figure 5. The class shown in Figure 8 is one of the most important classes because it represents conditions of very high energy. The mean spectrum is characterized by a directionally broad, low-frequency peak and a distinctive, directionally bimodal, high-frequency tail. This general structure was also observed by Long (in preparation) in a study of the evolution of directional spectra during individual storm events. Though derived from the same data set, the present result is notable because it suggests that, with minor variations, the same general structure appears in the same ranges of frequency and direction for many storms.

Spectral variation for this case is depicted in the lower graph in Figure 8. The shape of the standard deviation spectrum is roughly like that of the mean spectrum, with the exception of one strong peak at low frequency and centered near the shore-normal direction. The source of this peak is shown in Figure 9, which shows all 10 of the constituent spectra in this class. The strong peak in Figure 8 is due primarily to the last (right spectrum, bottom row) constituent spectrum shown in Figure 9. All the other spectra in Figure 9 are of quite similar structure, having the directionally broad, low-frequency peaks and directionally bimodal, high-frequency tails of the mean spectrum of Figure 8. Consequently, most of the variance shown in the lower graph of Figure 8 is due to relatively minor variations in amplitude and

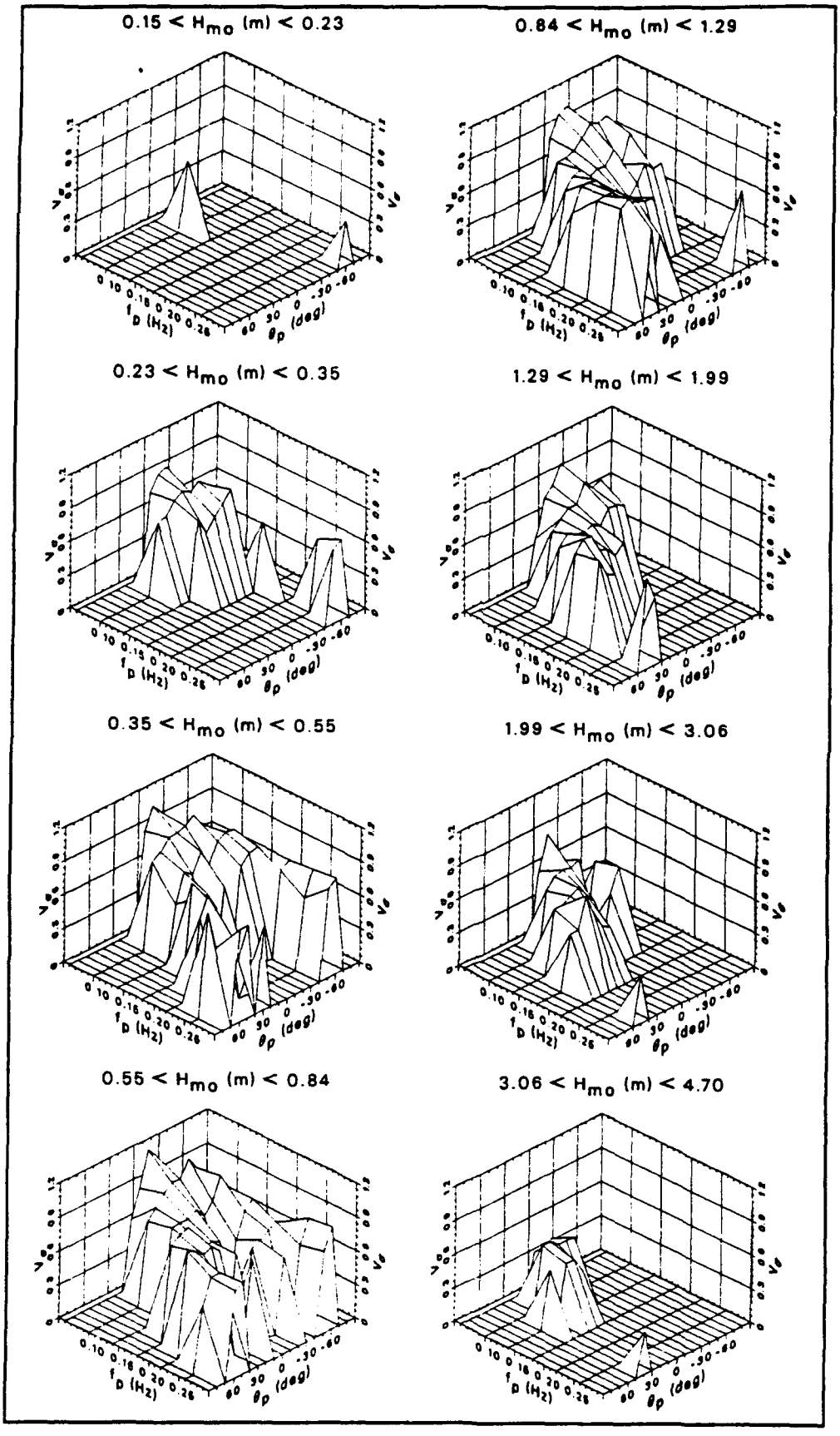

Figure 7. Volumes of standard deviation spectra for all spectral classes

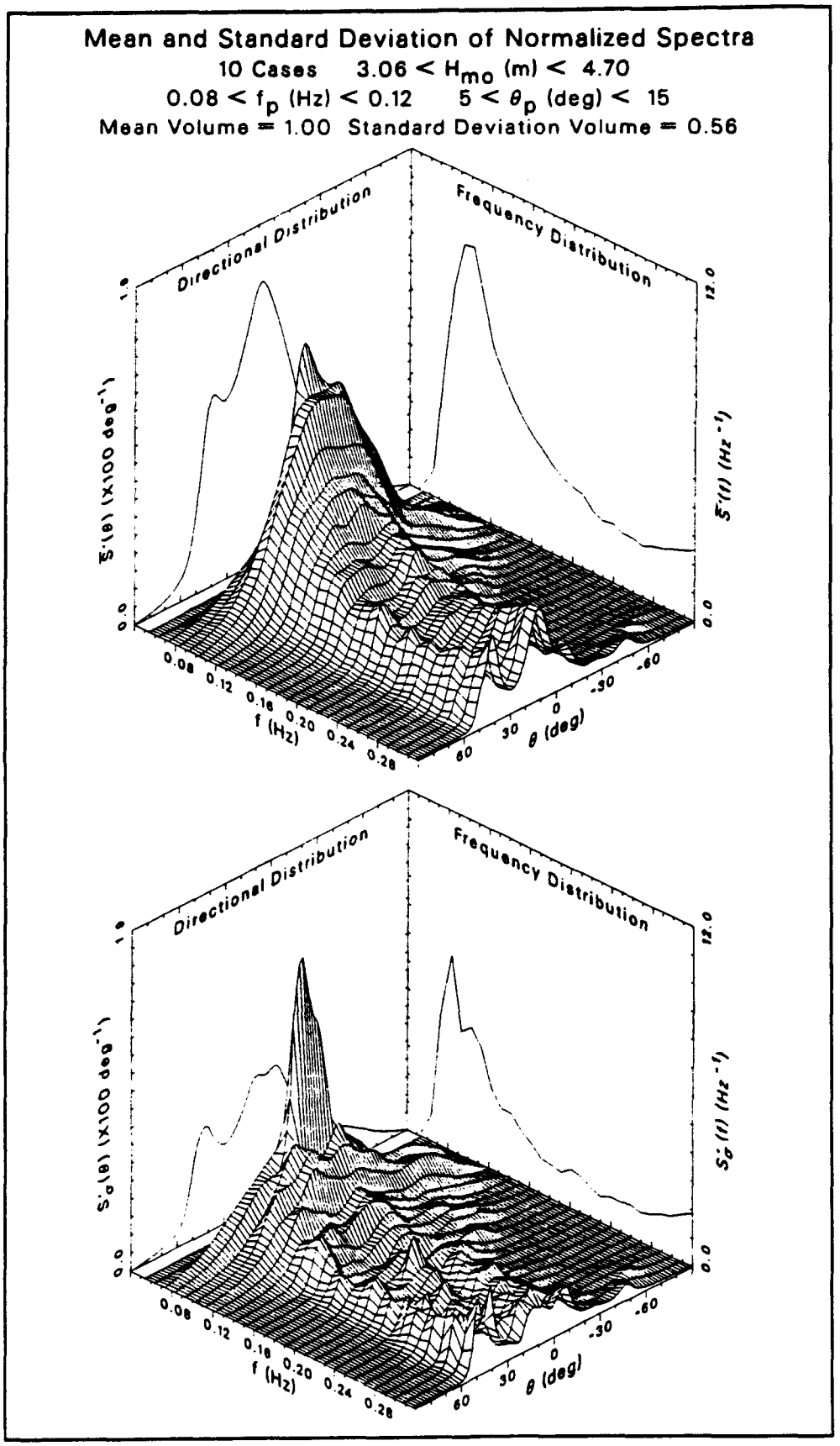

Figure 8. Mean and standard deviation spectra for a high-energy case

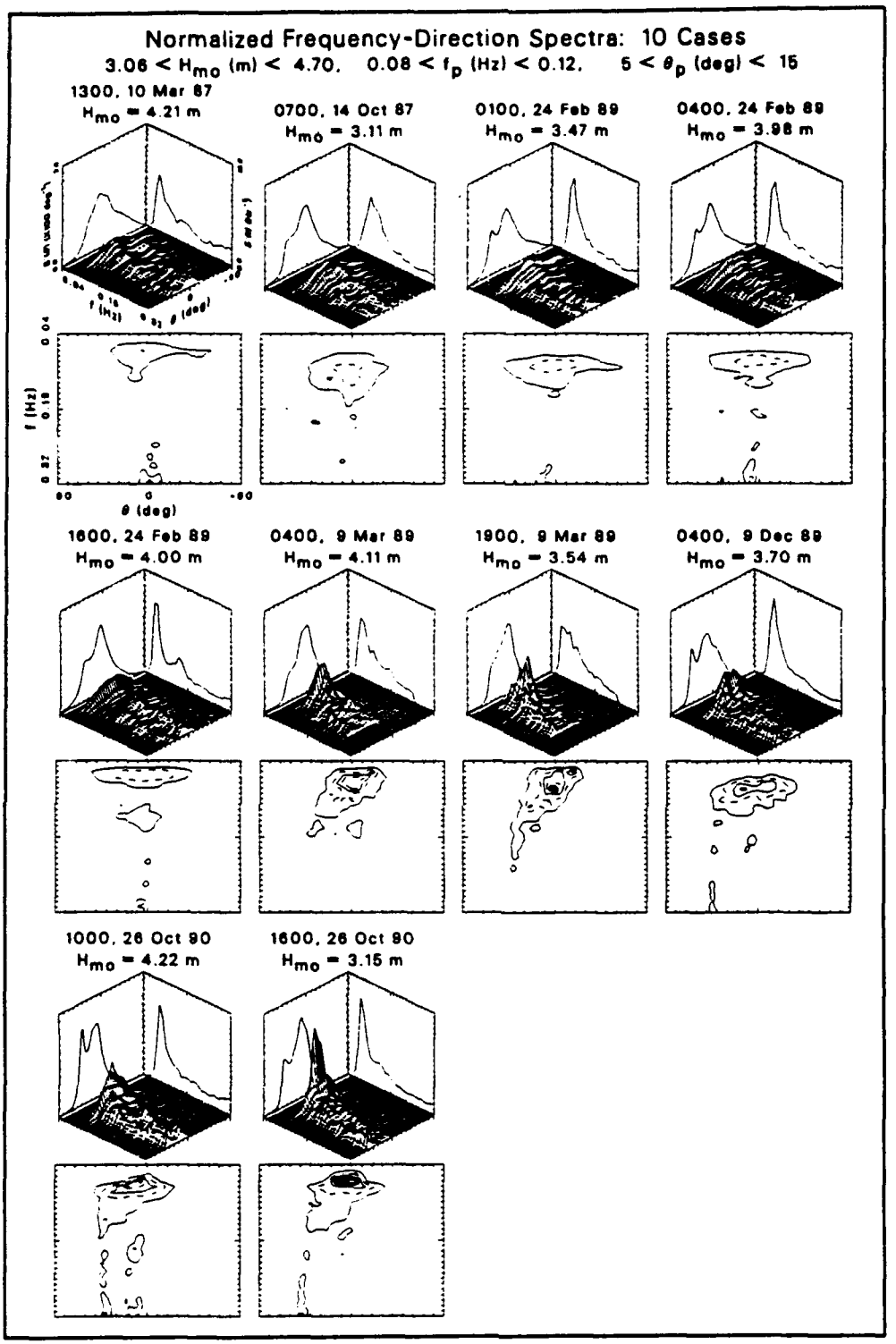

Figure 9. Constituent spectra for the class shown in Figure 8

frequency-direction location of the structural elements of the constituent spectra. This result means the characteristic spectrum $\overline{S^T}(f_n,\theta_m)$ in the upper graph of Figure 8 represents very well the major structural components of the constituent spectra for this class.

Discussion

One of the primary results of this study is the set of characteristic spectra discussed in this chapter and illustrated in Appendix A. Analysis of variability and its causes suggests that the characteristic spectra reflect at least the gross structures of the constituent spectra in a class. Hence, the characteristic spectra are much to be preferred over unidirectional, monochromatic spectra for engineering computations related to this and similar sites because they are more like the spectra of naturally occurring wave fields.

A modeler seeking seaward boundary conditions for a nearshore processes model or landward results for a model of wave transformation across the continental shelf can use these characteristic spectra as guides or templates of real wave properties. A model that produces results near to these characteristic spectra, within the variability quantified in this chapter and in the standard deviation spectra illustrated in Appendix B, can be judged as being valid within the range of natural variability. Consequently, the characteristic mean and standard deviation spectra found here should be of considerable aid in model testing and development.

Up to this point in this report, it has only been emphasized that the characteristic spectra found here are significantly different in shape from the unidirectional, monochromatic wave spectra that are the commonly used models for a three-parameter definition of wave conditions. Quantitative differences in properties used in modeling and engineering computations are needed to emphasize the importance of using the characteristic spectra instead of unidirectional, monochromatic waves, or, alternatively, the extent to which estimates using unidirectional, monochromatic waves can be corrected to reflect natural conditions with higher fidelity. Examples of these types of computations are given in the following two chapters.

4 Longshore Energy Flux

As a useful example of the sensitivity of engineering computations to choice of spectral definition, longshore energy fluxes are estimated and compared. The relevance of longshore energy flux is in its use as part of a model for longshore sediment transport contained in the SPM (1984). That model asserts that longshore sediment transport is directly proportional to longshore energy flux, so that any errors in estimating longshore energy flux translate directly into estimation errors of longshore sediment transport.

Definitions

In terms of a discrete frequency-direction spectrum $S(f_n,\theta_m)$, a general expression for longshore energy flux P_l is

$$P_l = \rho g \sum_{n=1}^{N} \sum_{m=1}^{M} C_g(f_n,d)\, S(f_n,\theta_m) \cos\theta_m \sin\theta_m\, \Delta\theta\, \Delta f \qquad (10)$$

where ρ is water density, g is gravitational acceleration, and $C_g(f_n,d)$ is wave group velocity appropriate to frequency f_n and water depth d. Equation 10 expresses the amount of longshore-directed wind wave energy flux through the point of spectral observation per unit of longshore distance.

To concentrate on the directional sensitivity of estimates of longshore energy flux, it is convenient to normalize both sides of Equation 10 with the expression $\rho g \sigma^2 \sqrt{gd}$. Division by ρg, which varies insignificantly, eliminates the leading coefficient of Equation 10. Division by $\sqrt{gd}$, which varies only nominally due to a tide range of about 1 m in the 8-m water depth, results in a dimensionless group velocity. Division by σ^2 converts the frequency-direction spectrum to the normalized form $S'(f_n,\theta_m)$ defined by Equation 6 and used in Chapter 3. The result of the normalization is a dimensionless longshore energy flux P_l', which has the form

$$P_l' = \sum_{n=1}^{N} \sum_{m=1}^{M} \frac{C_g(f_n,d)}{\sqrt{gd}} S'(f_n,\theta_m) \cos \theta_m \sin \theta_m \, \Delta\theta \, \Delta f \qquad (11)$$

In this chapter, estimates of P_l' are made from three spectral representations. One is a monochromatic, unidirectional representation for which entities are identified by the subscript *mu*. Another is the set of estimates from observed frequency-direction spectra, which served as the constituent spectra in the definitions of characteristic spectra in Chapter 3. Entities derived from observed frequency-direction spectra are identified by the subscript *fd*. The third set of estimates is derived from the characteristic spectra found in Chapter 3 and displayed in Appendix A. Entities associated with characteristic spectra are identified with an overbar on the subscript *fd*.

When a monochromatic, unidirectional spectrum is employed, Equation 11 is reduced to a much simpler form. A normalized monochromatic, unidirectional spectrum in discrete frequency-dimension space has a non-zero magnitude equal to $1/\Delta\theta\Delta f$ at only one discrete frequency $f_n = f_p$ and one discrete direction $\theta_m = \theta_p$. Consequently, there is only one non-zero value within the double summation of Equation 11, and the normalized monochromatic, unidirectional measure of longshore energy flux is

$$P_{l,mu}' = \frac{C_g(f_p,d)}{\sqrt{gd}} \cos \theta_p \sin \theta_p \qquad (12)$$

When both sides of Equation 12 are multiplied by $\rho g \sigma^2 \sqrt{gd}$, and it is noted that $\sigma^2 = \frac{1}{2}\left[\frac{H}{2}\right]^2$ for monochromatic, unidirectional waves, where H is actual wave height, the dimensional form of longshore energy flux defined in the SPM is recovered, i.e.,

$$P_{l,mu} = \frac{1}{2} \rho g \left[\frac{H}{2}\right]^2 C_g(f_p,d) \cos \theta_p \sin \theta_p \qquad (13)$$

Within a height-frequency-direction classification, there are K occurrences of the parameter set (H_{mo},f_p,θ_p). For the k^{th} occurrence, the monochromatic, unidirectional estimate of longshore energy flux is

$$P_{l,mu,k}' = \frac{C_g(f_{p,k},d_k)}{\sqrt{gd_k}} \cos \theta_{p,k} \sin \theta_{p,k} \qquad (14)$$

where $f_{p,k}$, $\theta_{p,k}$, and d_k are, respectively, the peak frequency, peak direction, and water depth associated with the k^{th} case. A parameter that represents the set of K monochromatic, unidirectional estimates within a class as a whole is the mean of the set, defined by

$$\overline{P'_{l,mu}} = \frac{1}{K} \sum_{k=1}^{K} P'_{l,mu,k} \tag{15}$$

A standard deviation of the set of monochromatic, unidirectional estimates within a class could be defined here, but it has been found to be small relative to other measures of variability. Consequently, it is not used in this analysis.

When dealing with a group of constituent frequency-direction spectra within a (H_{mo},f_p,θ_p) classification, the k^{th} spectrum produces an estimate of normalized longshore energy flux defined by

$$P'_{l,jkl,k} = \sum_{n=1}^{N} \sum_{m=1}^{M} \frac{C_g(f_n,d_k)}{\sqrt{gd_k}} S'_k(f_n,\theta_m) \cos\theta_m \sin\theta_m \Delta\theta \Delta f \tag{16}$$

which follows directly from Equation 11. The average estimate from a group of K constituent spectra within a class is defined by

$$\overline{P'_{l,jkl}} = \frac{1}{K} \sum_{k=1}^{K} P'_{l,jkl,k} \tag{17}$$

When Equation 16 is substituted into Equation 17, a triple summation occurs. Because each summation is a linear combination of terms, the summation over index k can be moved inside the summations over indexes n and m with the result that the sum over k acts on the product of dimensionless group velocity and constituent spectrum. Because the depth variations are small in this data set, the dimensionless group velocity does not change very much through its dependence on depth. Hence, the summation over k acts primarily to average the constituent spectra. The average of K constituent spectra is, by the definition of Equation 7, identical to the mean or characteristic spectrum of a class, as discussed in Chapter 3. An expression that should be very nearly equivalent to Equation 17, but in terms of a characteristic spectrum is

$$P'_{l,jkl} = \sum_{n=1}^{N} \sum_{m=1}^{M} \frac{C_g(f_n,d)}{\sqrt{gd}} \overline{S'}(f_n,\theta_m) \cos\theta_m \sin\theta_m \Delta\theta \Delta f \tag{18}$$

where the overbar on the subscript indicates the derivation from a mean spectrum.

To estimate the variability of longshore energy flux estimates from a set of K constituent spectra, a standard deviation has been computed for each class. For the K members of a class, the standard deviation is defined as

$$P'_{l,\theta,\sigma} = \sqrt{\frac{\sum_{k=1}^{K} P'^{2}_{l,\theta,k} - K\overline{P'_{l,\theta}}^{2}}{K-1}} \qquad (19)$$

Longshore Flux Estimates

Figures 10 to 13 show estimates of P'_l from the unidirectional, monochromatic formulation of Equation 14 (+'s), the frequency-direction spectral formulation of Equation 16 (x's), and the constituent frequency-direction spectral class averages of Equation 17 (solid dots) for all of the (H_{mo},f_p,θ_p) classes defined in Chapter 2. Each figure has two main subplots. Each subplot contains all estimates for the indicated wave-height class. Each subplot has seven horizontal axes, about which are plotted all estimates of P'_l as functions of θ_p for the indicated frequency class within a wave-height class. Estimates of $P'_{l,mu,k}$ and $P'_{l,\theta,k}$ are not averaged, but are simply grouped by class so that most of the overall data set is used. Estimates that fall into classes for which there are fewer than three constituent members are not plotted. Estimates of $\overline{P'_{l,\theta}}$ are class averages, and are plotted along the direction axis at their class-center directions.

Because of the simple form of Equation 14 for the monochromatic, unidirectional estimates, the grouping of +'s that show these estimates should follow a simple sinusoidal pattern with values of zero at θ_p = 90, 0, and -90 deg, a maximum at θ_p = 45 deg, and a minimum at θ_p = -45 deg. Examination of Figures 10 to 13 shows this to be generally true. The amplitudes of the sinusoidal patterns decrease with increasing frequency because the frequency-dependent group velocity decreases with increasing frequency. Within a frequency classification (i.e., along one of the horizontal axes within a height-specific subplot), there is some minor variation in the values of the sinusoidal curves because observed, tidally varying depths were used in the computations, and because each frequency classification includes a small range of frequencies, all of which affect the ratio $C_g(f_{p,k},d_k)/\sqrt{gd_k}$ in Equation 14.

In distinct contrast, the sets of x's that denote the frequency-direction spectral estimates form clouds of points having considerable variation, and

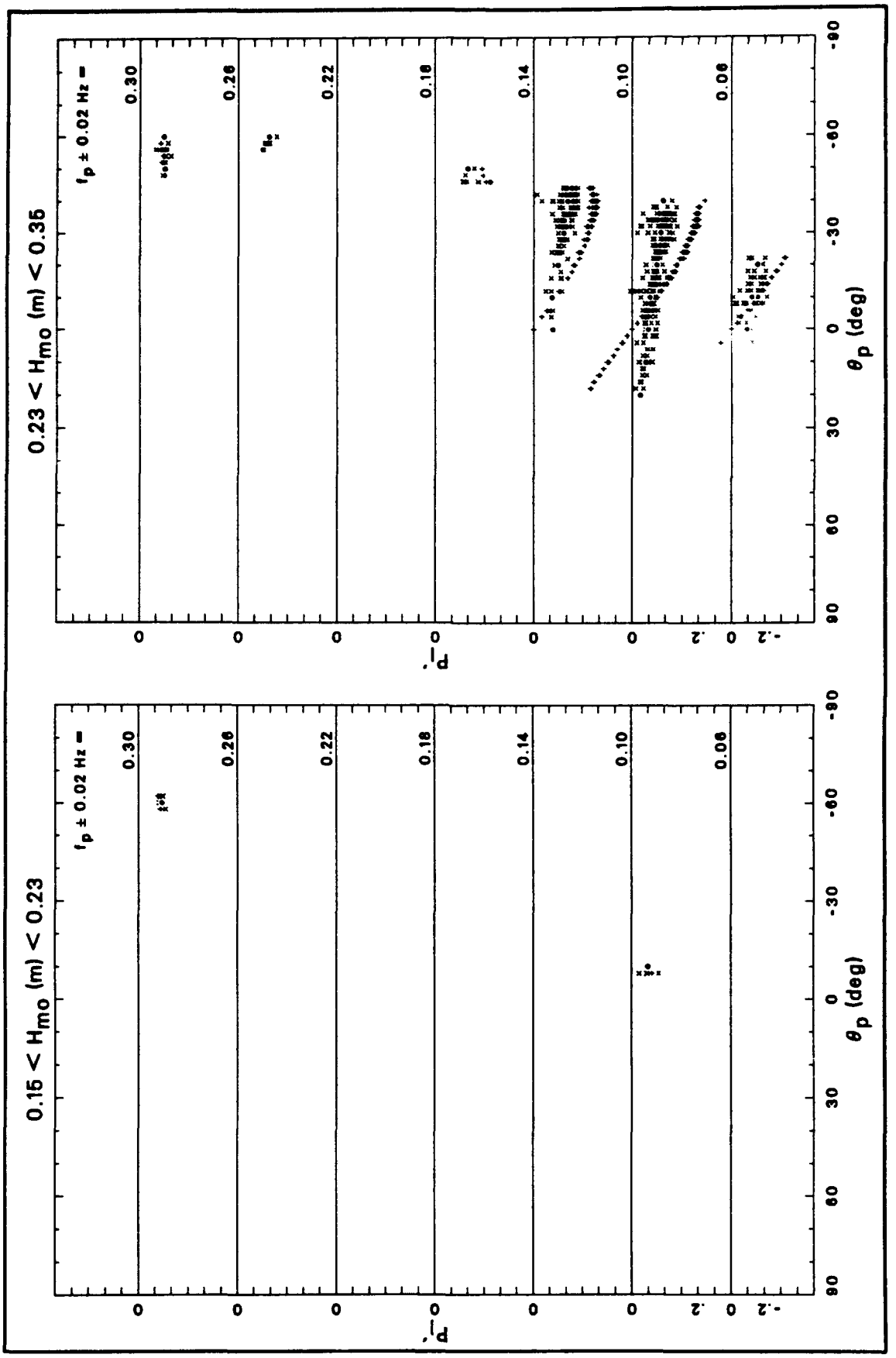

Figure 10. Longshore energy flux estimates for wave heights between 0.15 and 0.35 m

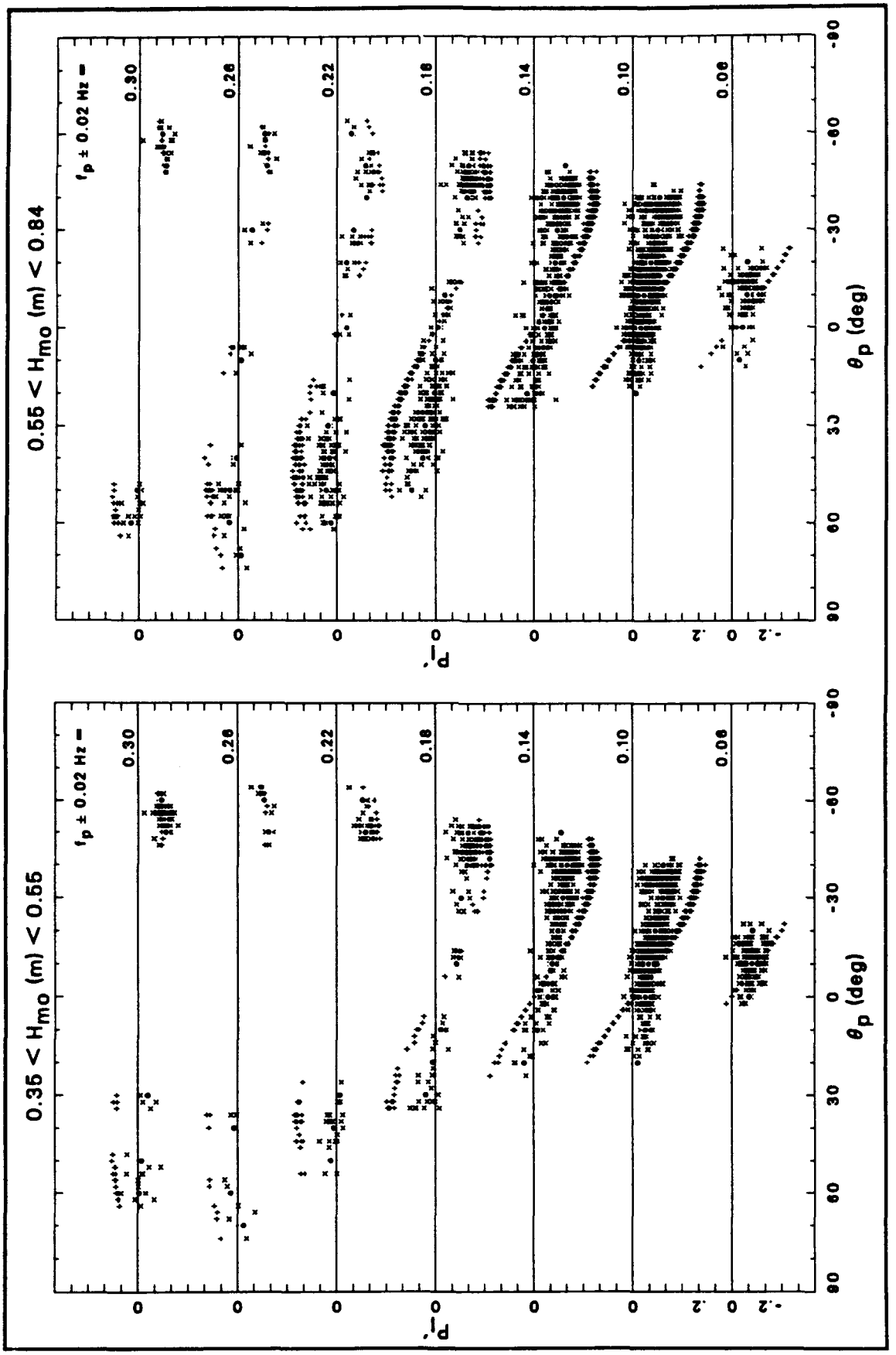

Figure 11. Longshore energy flux estimates for wave heights between 0.35 and 0.84 m

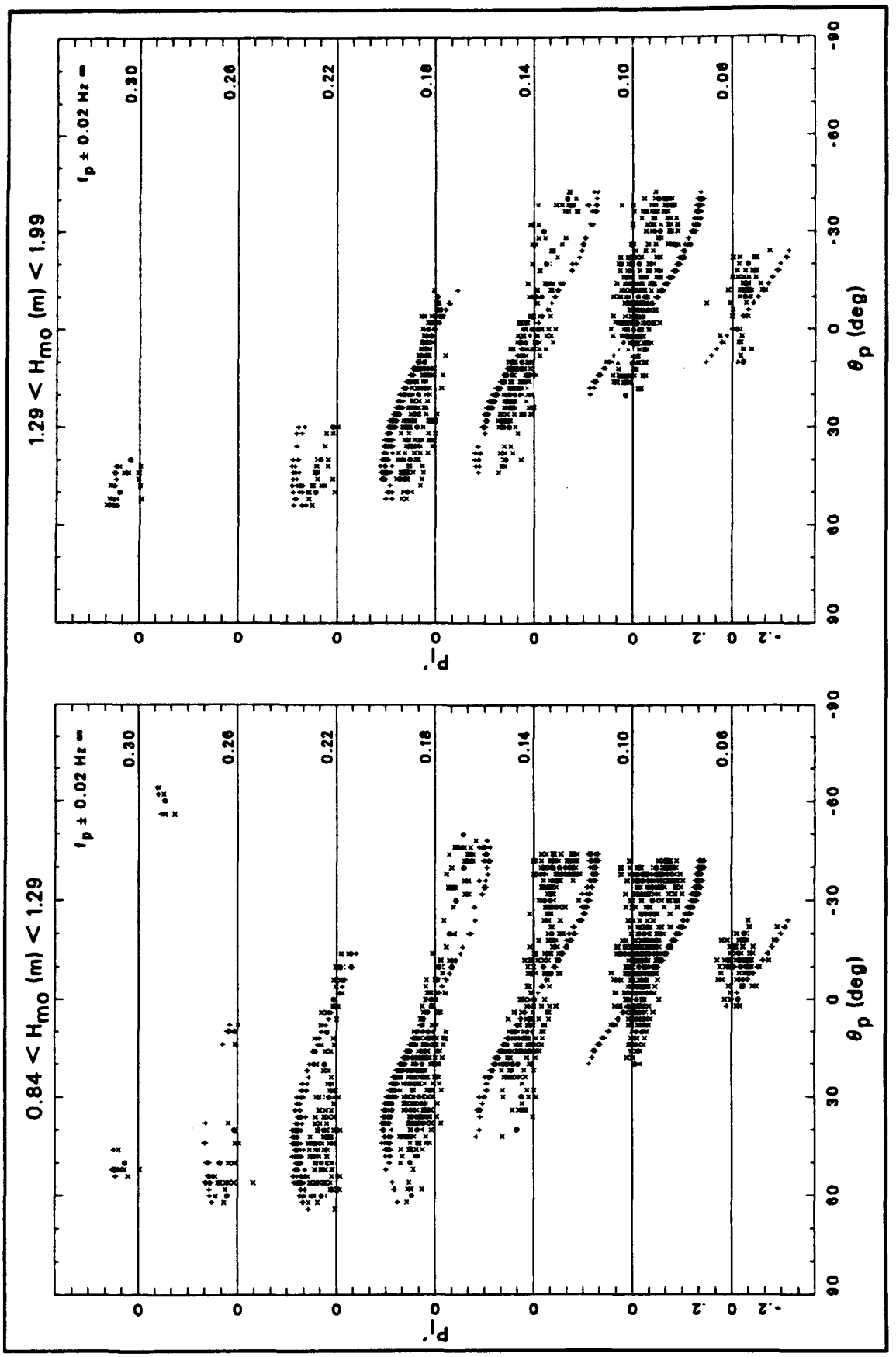

Figure 12. Lc gshore energy flux estimates for wave heights between 0.84 and 1.99 m

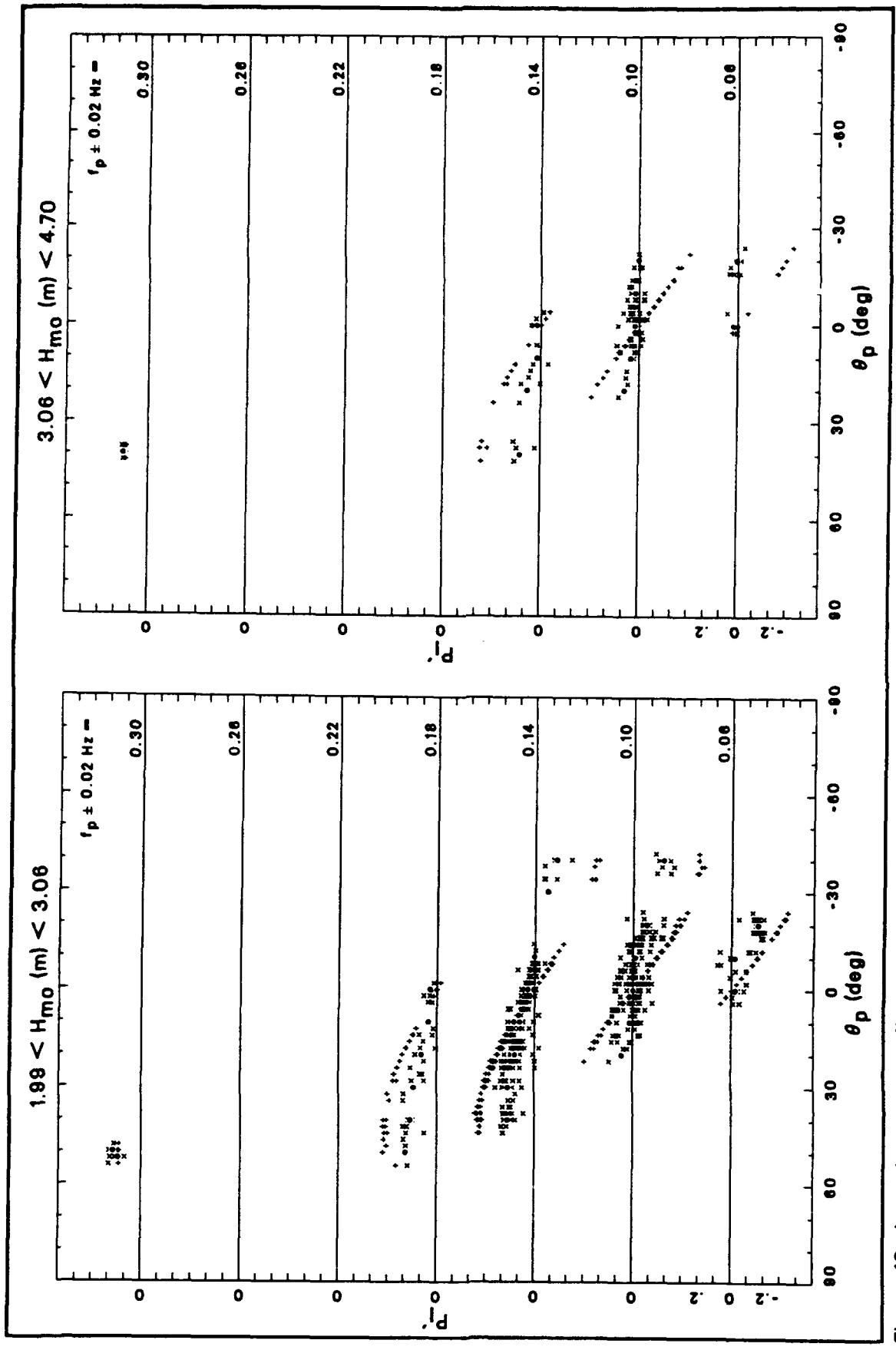

Figure 13. Longshore energy flux estimates for wave heights between 1.99 and 4.70 m

following general patterns that align with the monochromatic, unidirectional estimates at very few places. The solid dots that represent estimates from characteristic spectra fall within the clouds of x's from the constituent spectra, as is expected from the discussion leading to Equation 18.

These results mean that highly resolved spectra give very different results from those of simple, unidirectional, monochromatic representations of sea state. Important questions that naturally arise from these results relate to the severity of the differences and the extent to which corrections can be made in those instances where well-resolved spectra are not available and only characteristic height, frequency, and direction are known.

Error Analysis

To evaluate the differences in the various estimates of longshore energy flux, three sets of estimators are compared. First, characteristic spectrum estimates $P'_{l,\vec{H}}$ are compared to the means $\overline{P'_{l,\vec{H}}}$ and standard deviations $P'_{l,\vec{H},\sigma}$ from constituent spectra in their classes to see how well class groupings of measured spectra compare. Second, characteristic spectrum estimates are compared to means $\overline{P'_{l,mu}}$ from monochromatic, unidirectional estimates in their classes to see if there is any general trend in estimate differences. Finally, differences of characteristic spectrum estimates from means of monochromatic, unidirectional estimates are computed class by class to define empirical correction functions.

Figure 14 shows a correlation of $P'_{l,\vec{H}}$ with class statistical properties from constituent frequency-direction spectra in the form $\overline{P'_{l,\vec{H}}} \pm P'_{l,\vec{H},\sigma}$ for all classes. Symbols distinguish wave height classes, and, because high-energy cases are more important, solid symbols have been used to denote classes for which characteristic wave heights exceed 2 m. It is evident in Figure 14 that $P'_{l,\vec{H}}$ correlates very well with $\overline{P'_{l,\vec{H}}}$, meaning that computations using characteristic spectra are good estimators of the expected or mean longshore energy fluxes for all classes.

Also evident in Figure 14 is that there is considerable variation in energy flux estimates within classes as indicated by the lengths of the standard deviation lines. Standard deviations are reasonably uniform (for the purposes of this study), having nominal dimensionless values of ± 0.05 for the entire range of flux estimates. This result means that longshore energy flux estimates computed with characteristic spectra will have an associated, uncorrectable uncertainty of this size. The uncertainty cannot be expressed as a percentage because longshore fluxes can be zero. The effect of the uncertainty is worst near $P'_l = 0$ because varying the estimate within the range of uncertainty can cause flux estimates to change sign. This effect is especially bad for high-energy cases, several of which are located near the origin of

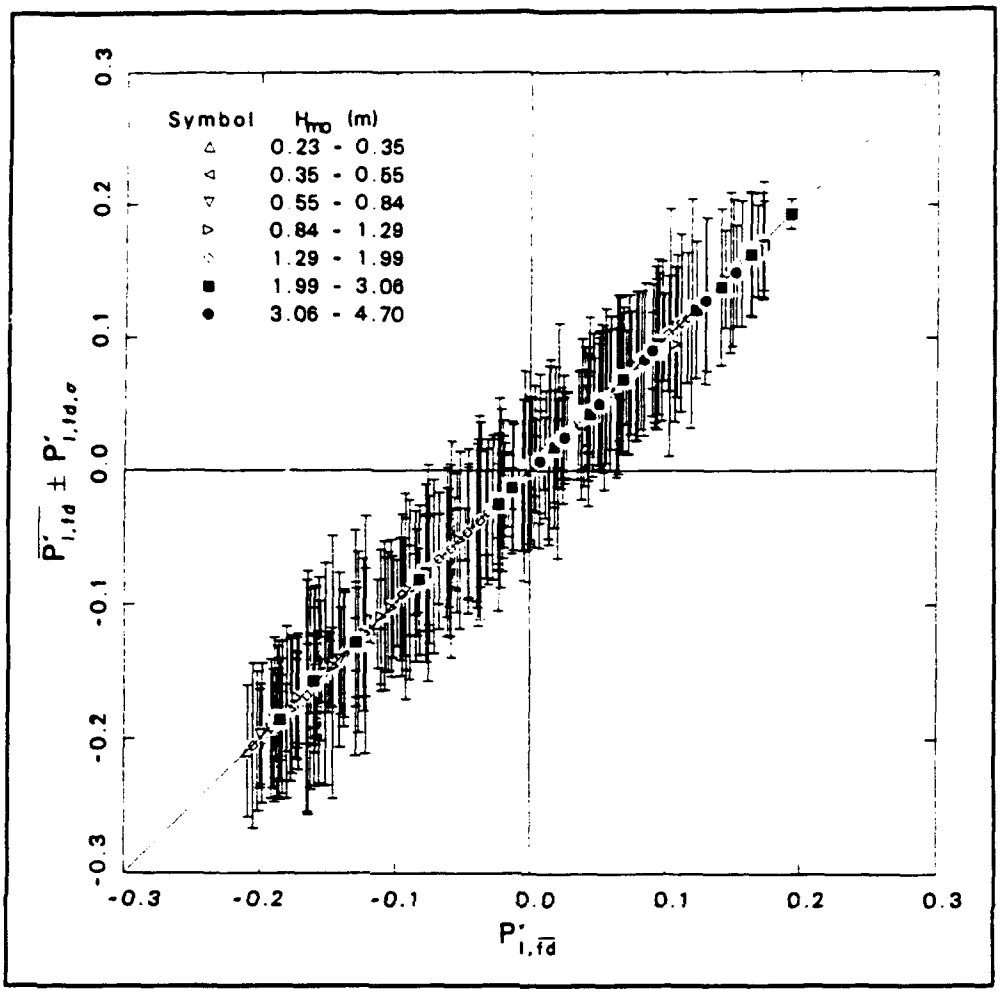

Figure 14. Correlation of P_l' estimates from characteristic spectra with those of class averages of constituent spectra

Figure 14. If used in a sediment transport model, the effect of changing sign on the longshore energy flux in high-energy conditions would result in a large volume of sediment being moved the wrong way, which may be an unacceptable result in an engineering application. This result suggests that a more refined method of spectral classification may be justified. Though the result is disquieting, it has the advantage that a magnitude can be assigned to the uncertainty in longshore flux estimates from characteristic spectra.

Even more disquieting are estimates of longshore energy flux from class averages using monochromatic, unidirectional wave models. Figure 15 illustrates the correlation of $\overline{P'_{l,mu}}$ with $P'_{l,\overline{fd}}$ for all classes. Standard deviations for the monochromatic, unidirectional estimates are not shown because they are very small relative to the symbol sizes used in Figure 15. Again, solid symbols denote high-energy classes. Though there is a vague pattern to the scatter of symbols (monochromatic, unidirectional estimates tend to be larger than those from characteristic spectra), there is not enough correlation to suggest that an accurate correction could be devised based on this representation of the

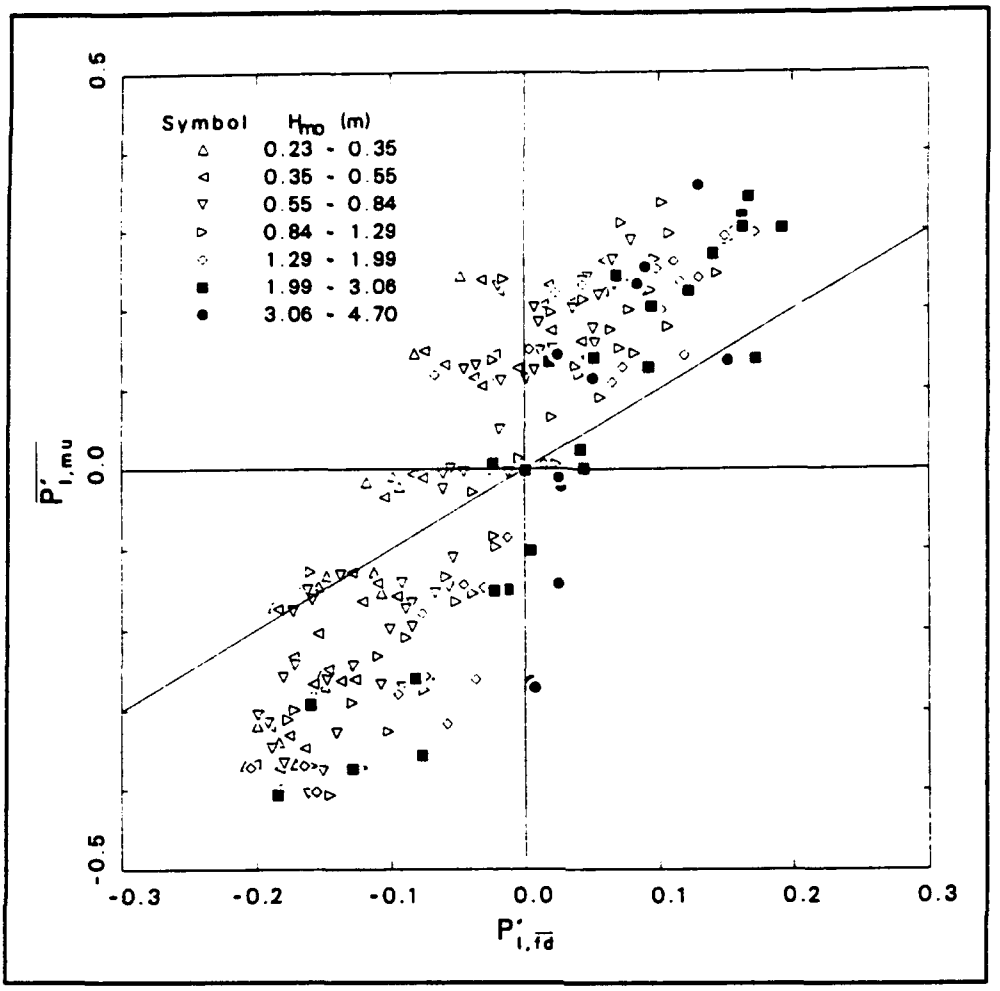

Figure 15. Correlation of longshore energy flux estimates from characteristic spectra with those of class averages of monochromatic, unidirectional spectra

data set as a whole. The differences are substantial. Several of the high-energy symbols fall in one of the two quadrants (upper left and lower right) indicating results of opposite sign. Other high-energy symbols have characteristic spectral values near zero while the monochromatic, unidirectional estimates have values very different from zero.

All is not lost, however. Examination of Figures 10 to 13 indicates that the differences between the rather clean pattern of monochromatic, unidirectional estimates and the likewise clean pattern of characteristic spectral estimates follow a systematic pattern that is a function of the characterizing parameter set (H_{mo}, f_p, θ_p). This pattern is called a bias, and is plotted in Figure 16 as $\overline{P'_{l,mu}} - P'_{l,\overline{fd}}$ as a function of direction-class center direction for all wave height and frequency classes, following the pattern used in Figures 10 to 13. Where data are available in Figure 16, it appears that the bias has broad tendencies to be small near peak directions of 0 deg, with a maximum near 45 deg, and a minimum near -45 deg. Subtleties in its behavior do not make it amenable to analytic description, however, so the empirical

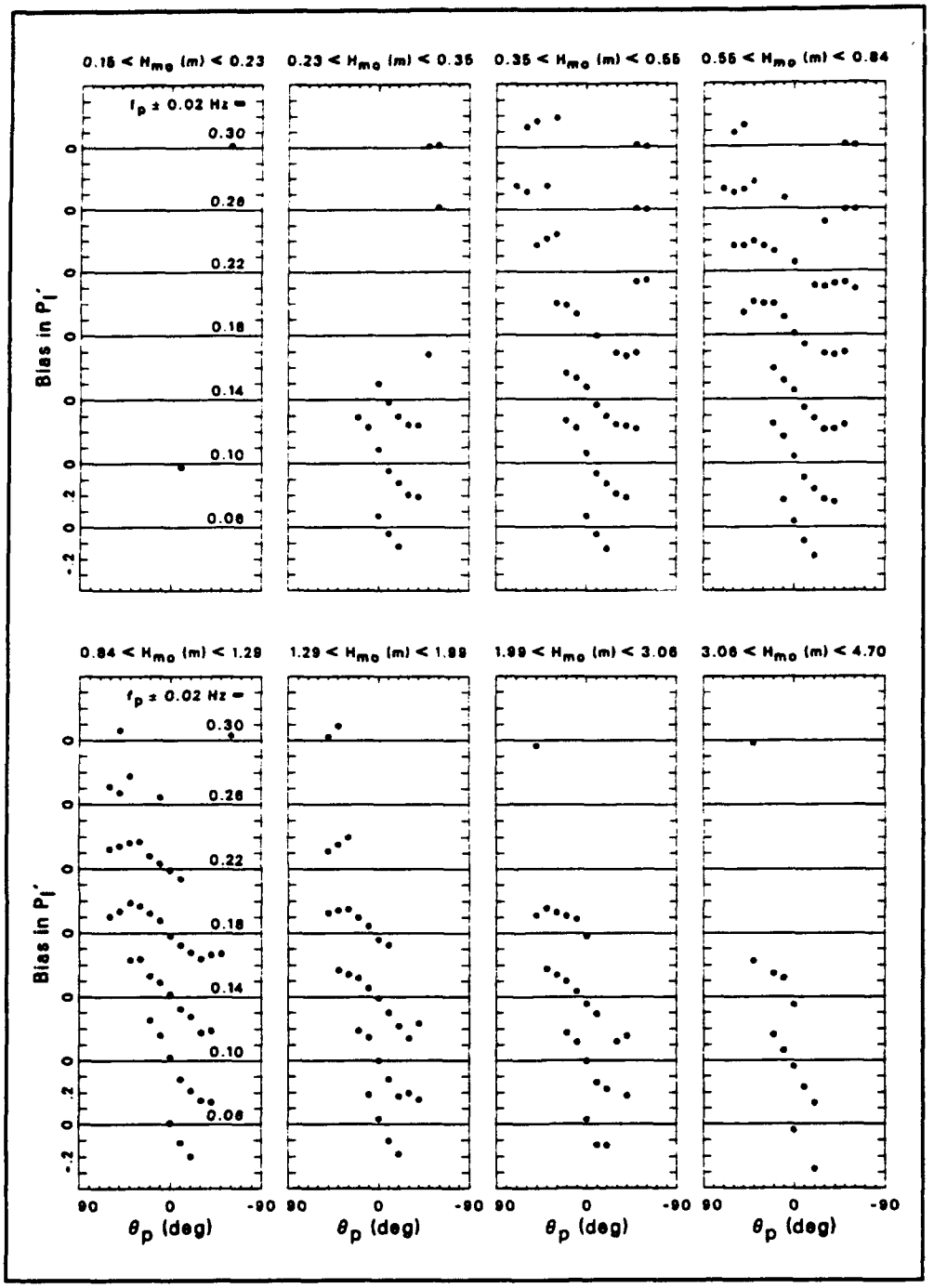

Figure 16. Bias in P_l' estimates

function approximated by the whole of Figure 16 is considered here to be defined only graphically. Nonetheless, its systematic nature is clearly evident.

Method of Correction

The results of the last section show that an estimate of longshore energy flux from a monochromatic, unidirectional representation of a wave field defined only by the parameters (H_{mo}, f_p, θ_p) is rather poor when compared to estimates based on averages of highly resolved, naturally occurring, frequency-direction spectra. Without correction, engineering computations based on monochromatic, unidirectional estimates are likely to be in serious error, especially at times of high energy. However, because the bias function is reasonably well-behaved, as shown in Figure 16, and the uncertainty associated with estimates based on characteristic spectra is quantifiable, as shown in Figure 14, it is possible to formulate an improved estimate that includes a measure of statistical error. The objective is to provide a better estimate of longshore energy flux in those instances when all that is known are three characteristic wave field parameters.

The improved estimate consists simply of a monochromatic, unidirectional estimate from which bias has been subtracted and to which is affixed an estimate of uncertainty. The mathematical expression of this estimate is, for dimensionless estimates

$$\hat{P}'_l = \frac{C_g(f_p,d)}{\sqrt{gd}} \cos\theta_p \sin\theta_p - bias(H_{mo},f_p,\theta_p) \pm 0.05 \qquad (20)$$

where $bias(H_{mo},f_p,\theta_p)$ is found graphically from Figure 16, and $\hat{P}'_l$ indicates a computational estimate. A dimensional estimate $\hat{P}_l$ is computed by multiplying both sides of Equation 20 with the normalization factor $\rho g \sigma^2 \sqrt{gd}$, and noting that $\sigma^2 = H_{mo}^2/16$. The dimensional result in terms of the three characteristic parameters H_{mo}, f_p, and θ_p, assuming water density ρ and depth d are known, is

$$\hat{P}_l = \rho g \frac{H_{mo}^2}{16} \sqrt{gd} \left[\frac{C_g(f_p,d)}{\sqrt{gd}} \cos\theta_p \sin\theta_p - bias(H_{mo},f_p,\theta_p) \pm 0.05 \right] \qquad (21)$$

Equation 21 represents the optimum estimate of longshore energy flux based on three known parameters because removal of the bias converts the estimate to the expected or most probable value for each class. The remaining uncertainty represented by the standard deviation estimate can not be reduced further because of the constraints imposed by the present method of analysis. An engineer wishing to compute longshore energy flux can use Equation 21 with the knowledge that it gives the most probable estimate and, further, can determine the effect of uncertainty in the estimate on engineering computations.

There are two major points to keep in mind before employing Equation 21. First, it is a result of the particular type of analysis done in this report. If the set of characterizing parameters is different (e.g., using root-mean-square wave height instead of H_{mo}, or mean wave direction instead of θ_p), the consequences of spectral averaging, spectral grouping, and variance estimates are likely to be different. This situation may require making additional assumptions about relationships among characterizing parameters, or may invalidate the use of Equation 21 altogether. Second, the results shown here are very specific to observations at the FRF. Application at sites having similar forcing and boundary conditions will likely produce meaningful results that, at least, will provide some guidance. Application of Equation 21 at dissimilar sites is not recommended because climatological relationships between spectral parameters and true spectral shapes is generally not known. If such relationships are known, an analysis like the present one would prove useful.

As a final observation for this chapter, it is noted that the uncertainty in the estimate of longshore energy flux in Equation 21 can be reduced if additional parameters are used to classify the basic spectra in the database. Measures of such things as directional spread, and the existence and strengths of multimodal peaks in the spectra would result in smaller variations in the statistics of mean spectra, as discussed in Chapter 3. Consequent estimates of longshore energy flux would then vary less within classes, and better estimates could be computed. The utility of this approach is limited, however, because measures of these additional parameters are not widely done in field studies, so the requisite information is often lacking. When such parameters become more commonly available, it would be most useful to perform a more refined analysis of the present data set, and develop an estimator for longshore energy flux that has a smaller confidence interval.

5 Radiation Stresses

Another direction-sensitive entity used in modeling and computation of nearshore processes is the radiation stress tensor, which has three unique components that arise when solutions from linear wave theory are applied to the nonlinear terms in the theoretical equations for the conservation of momentum. Spatial divergences of radiation stresses, which reach maxima in the surf zone, are primary causes of wave-driven currents. These divergences are computed from differences of radiation stress components at various points in space. It is essential that correct radiation stress values are used for proper computation of nearshore currents, as well as processes resulting from nearshore currents, such as sediment transport.

The procedure in this chapter is the same as in Chapter 4. Governing equations are defined and estimates of radiation stress terms by three methods are compared. Finally, methods are suggested for making optimal estimates when the only information available is the characteristic parameter set (H_{mo}, f_p, θ_p).

Definitions

The radiation stress tensor can be represented by a two-dimensional, symmetric matrix with components given the general symbol S_{ij}. Because of symmetry, there are three unique components S_{11}, S_{12} (which equals S_{21}), and S_{22}. The term S_{11} is often called S_{xx} and represents the onshore flux of onshore wave momentum. The term S_{12} is often called S_{xy} and represents the onshore flux of longshore wave momentum. The alongshore flux of longshore wave momentum is represented by S_{22} or S_{yy}. Based on the work of Longuet-Higgins and Stewart (1964), Horikawa (1988) shows a compact formulation for the radiation stresses for unidirectional, monochromatic waves, and Thornton and Guza (1989) show the form of S_{12} when the wave energy distribution is in the form of a discrete frequency-direction spectrum $S(f_n, \theta_m)$. Combining these various expressions results in a general equation for the radiation stresses in terms of a discrete spectrum. This equation is

$$S_{ij} = \rho g \sum_{n=1}^{N} \sum_{m=1}^{M} W_{ij}(f_n,\theta_m,d)\ S(f_n,\theta_m)\ \Delta\theta\ \Delta f \qquad i,j = 1,2 \qquad (22)$$

where $W_{ij}(f_n,\theta_m,d)$ is a dimensionless weighting function defined by

$$W_{ij}(f_n,\theta_m,d) = \left[\ e_i(\theta_m)\ e_j(\theta_m) + \delta_{ij}\ \right] \frac{C_g(f_n,d)}{C(f_n,d)} - \tfrac{1}{2}\delta_{ij} \qquad (23)$$

Within the weighting function, $e_1(\theta_m) = \cos\theta_m$, $e_2(\theta_m) = \sin\theta_m$, and δ_{ij} is the Kronecker delta function, which is equal to 1 when $i = j$, and equal to 0 otherwise. $C(f_n,d)$ is wave phase speed from the dispersion relation of linear wave theory.

As with estimates of longshore energy flux discussed in Chapter 4, it is useful to eliminate variations of total wave energy within a wave-height class from calculations of radiation stresses, so that results will give a stronger indication of directional sensitivity. If both sides of Equation 22 are divided by $\rho g\sigma^2$, and it is noted that division by σ^2 converts the frequency-direction spectrum to the normalized form of Equation 6, an expression for dimensionless radiation stresses S'_{ij} is found. That expression can be written

$$S'_{ij} = \sum_{n=1}^{N} \sum_{m=1}^{M} W_{ij}(f_n,\theta_m,d)\ S'(f_n,\theta_m)\ \Delta\theta\ \Delta f \qquad i,j = 1,2 \qquad (24)$$

When used with monochromatic, unidirectional waves, Equation 24 reduces to a simpler form. Discrete spectra representing such waves are zero everywhere except at $f_n = f_p$ and $\theta_m = \theta_p$, at which point $S'(f_p,\theta_p) = 1/\Delta\theta\Delta f$. Using these relationships in Equation 24, and letting $S'_{ij,mm}$ represent a dimensionless, monochromatic, unidirectional radiation stress estimate, results in

$$\begin{aligned} S'_{ij,mm} &= W_{ij}(f_p,\theta_p,d) \\ &= \left[\ e_i(\theta_p)\ e_j(\theta_p) + \delta_{ij}\ \right] \frac{C_g(f_p,d)}{C(f_p,d)} - \tfrac{1}{2}\delta_{ij} \end{aligned} \qquad (25)$$

To distinguish the k^{th} such estimate among a set of K occurrences in a class, the additional subscript k is attached to the radiation stress estimate and to the parameters upon which it depends. The result is

$$S'_{ij,mn,k} = \left[e_i(\theta_{p,k})\, e_j(\theta_{p,k}) + \delta_{ij} \right] \frac{C_g(f_{p,k}, d_k)}{C(f_{p,k}, d_k)} - \frac{1}{2}\delta_{ij} \tag{26}$$

An average of K such estimates within a class is

$$\overline{S'_{ij,mn}} = \frac{1}{K} \sum_{k=1}^{K} S'_{ij,mn,k} \tag{27}$$

A (H_{mo}, f_p, θ_p) class grouping also contains K constituent frequency-direc- spectra, of which the k^{th} member is $S'_k(f_n, \theta_m)$. A radiation stress estimate d on this constituent spectrum is

$$S'_{ij,fd,k} = \sum_{n=1}^{N} \sum_{m=1}^{M} W_{ij}(f_n, \theta_m, d_k)\, S'_k(f_n, \theta_m)\, \Delta\theta\, \Delta f \tag{28}$$

Statistics of a group of K such estimates include a mean $\overline{S'_{ij,fd}}$ and standard deviation $S'_{ij,fd,\sigma}$ of the set. The mean is defined by

$$\overline{S'_{ij,fd}} = \frac{1}{K} \sum_{k=1}^{K} S'_{ij,fd,k} \tag{29}$$

and the standard deviation is

$$S'_{ij,fd,\sigma} = \sqrt{\frac{\sum_{k=1}^{K} S'^{\,2}_{ij,fd,k} - K\,\overline{S'_{ij,fd}}^{\,2}}{K - 1}} \tag{30}$$

To compare the statistics of Equations 29 and 30 with the results of a statistically averaged or characteristic spectrum, as defined in Chapter 3, one can compute

$$S'_{ij,fd} = \sum_{n=1}^{N} \sum_{m=1}^{M} W_{ij}(f_n, \theta_m, d)\, \overline{S'}(f_n, \theta_m)\, \Delta\theta\, \Delta f \tag{31}$$

It is anticipated that $S'_{ij,E}$ will correlate well with $\overline{S'_{ij,E}}$ because the nominal 8-m water depth at the site of the FRF directional wave gauge is large relative to the tide range. Consequently, total water depth does not vary greatly, and depth-dependent functions, like the ratio of group velocity to wave phase speed in W_{ij}, do not change much from observation to observation. Averages of radiation stress estimates from constituent spectra should thus behave like estimates from averaged spectra.

Most of the discussion of estimate comparisons and error analysis in this chapter will be related to S_{12} (or S_{xy}) because it is typical of radiation stress components, and treatment of the other components follows the same pattern. Summary statements for the other components will be given in this chapter based on supporting figures found in Appendix C.

Estimates of S_{xy}

For the computation of S'_{xy}, the weighting function W_{ij} can be replaced in Equation 24 and following equations by its trigonometric function content with the delta functions evaluated. This process results in the general form of S'_{xy} from Equation 24 as

$$S'_{xy} = \sum_{n=1}^{N} \sum_{m=1}^{M} \frac{C_g(f_n,d)}{C(f_n,d)} S'(f_n,\theta_m) \cos\theta_m \sin\theta_m \Delta\theta \Delta f \qquad (32)$$

Note that this equation is much like that for longshore energy flux, the difference being that dimensionless spectra are weighted by ratio of group velocity to phase speed for S'_{xy}, and by ratio of group velocity to $\sqrt{gd}$ for P'_l. When the replacement and evaluation process is applied to Equations 25 to 31, the resulting equations relate various ways to compute S'_{xy} and its statistics, and have the same trigonometric and delta function dependence as Equation 32.

S'_{xy} Distributions

Figures 17 to 20 show estimates of S'_{xy} from three methods of computation. Unidirectional, monochromatic estimates from Equation 26 are shown as +'s. Estimates based on Equation 28, using individual constituent spectra, are shown as x's. Solid dots represent results from Equation 31 using the characteristic spectra defined in Chapter 3. Results from all height, frequency, and direction classes are shown following the same display pattern used in Figures 10 to 13.

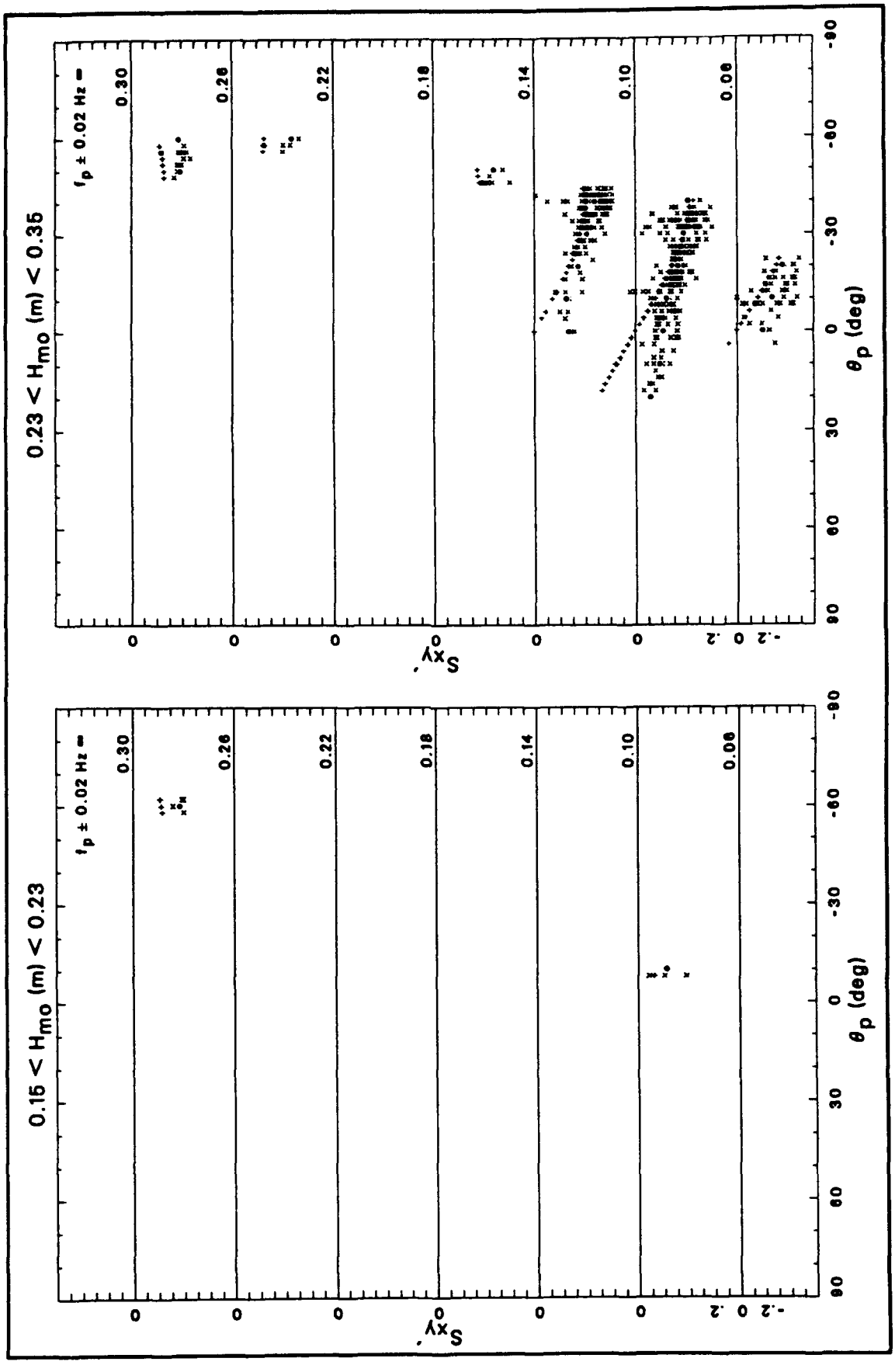

Figure 17. Estimates of S_{xy}' for wave heights between 0.15 and 0.35 m

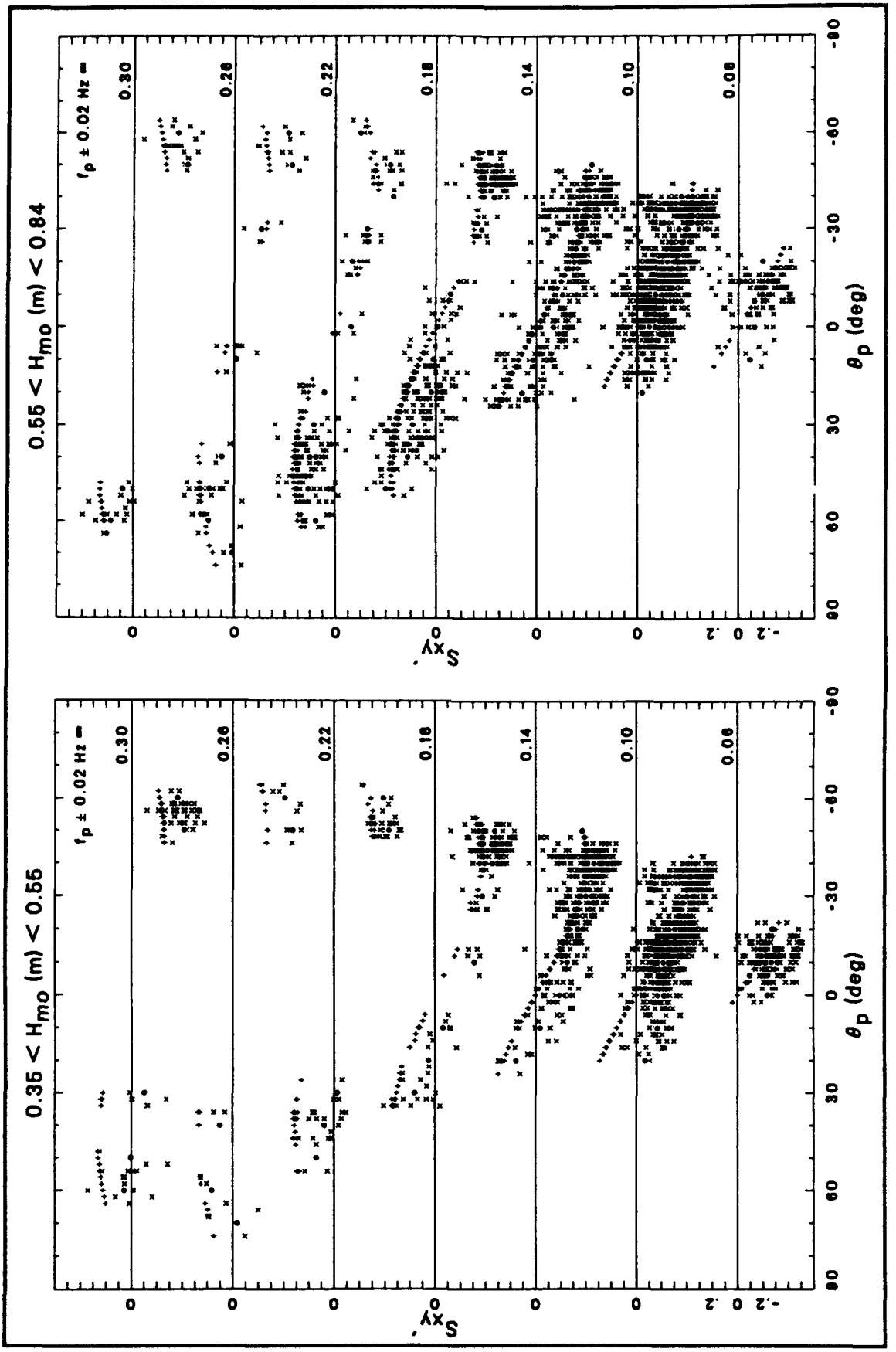

Figure 18. Estimates of S_{xy}' for wave heights between 0.35 and 0.84 m

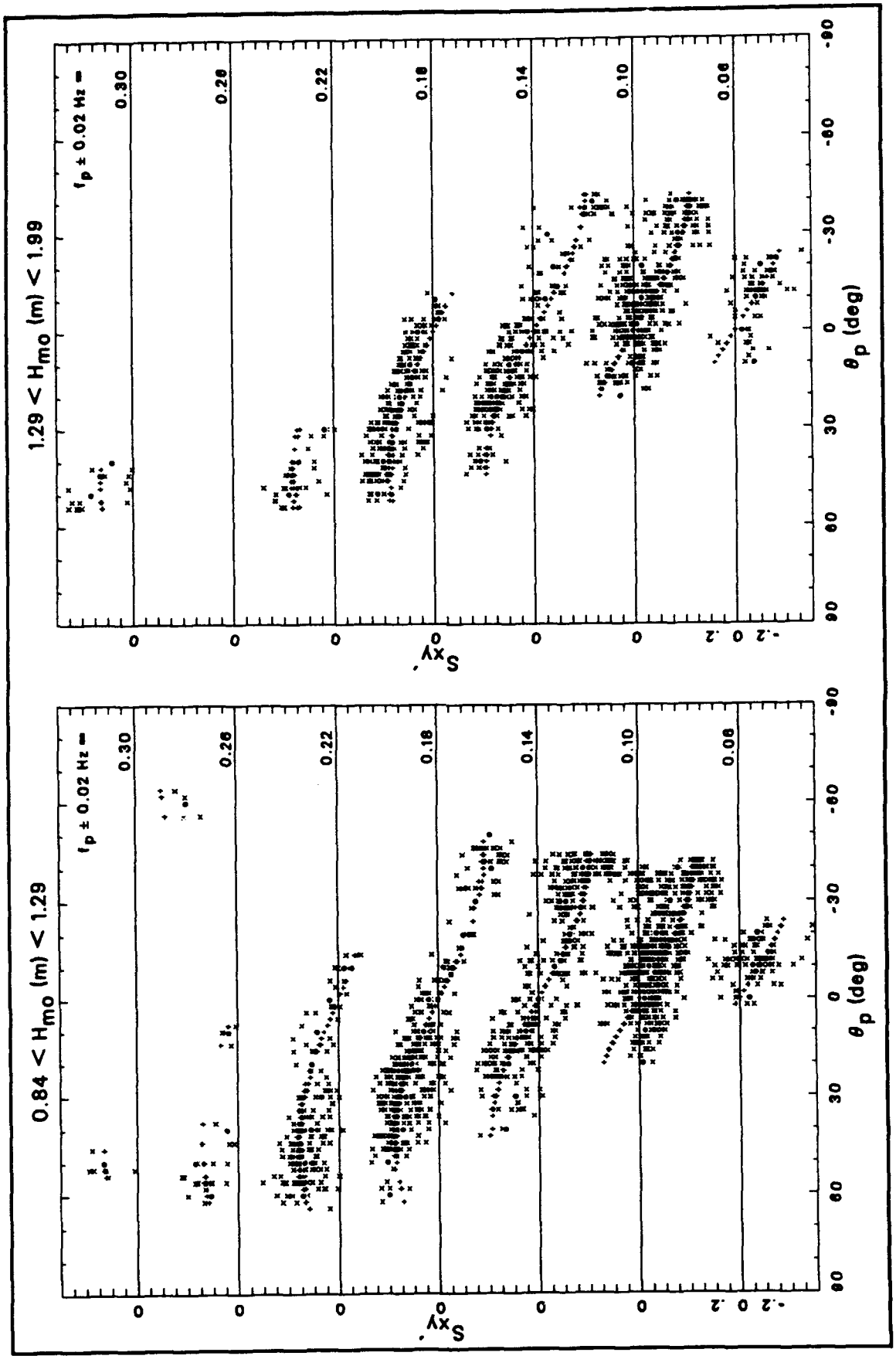

Figure 19. Estimates of S_{xy}' for wave heights between 0.84 and 1.99 m

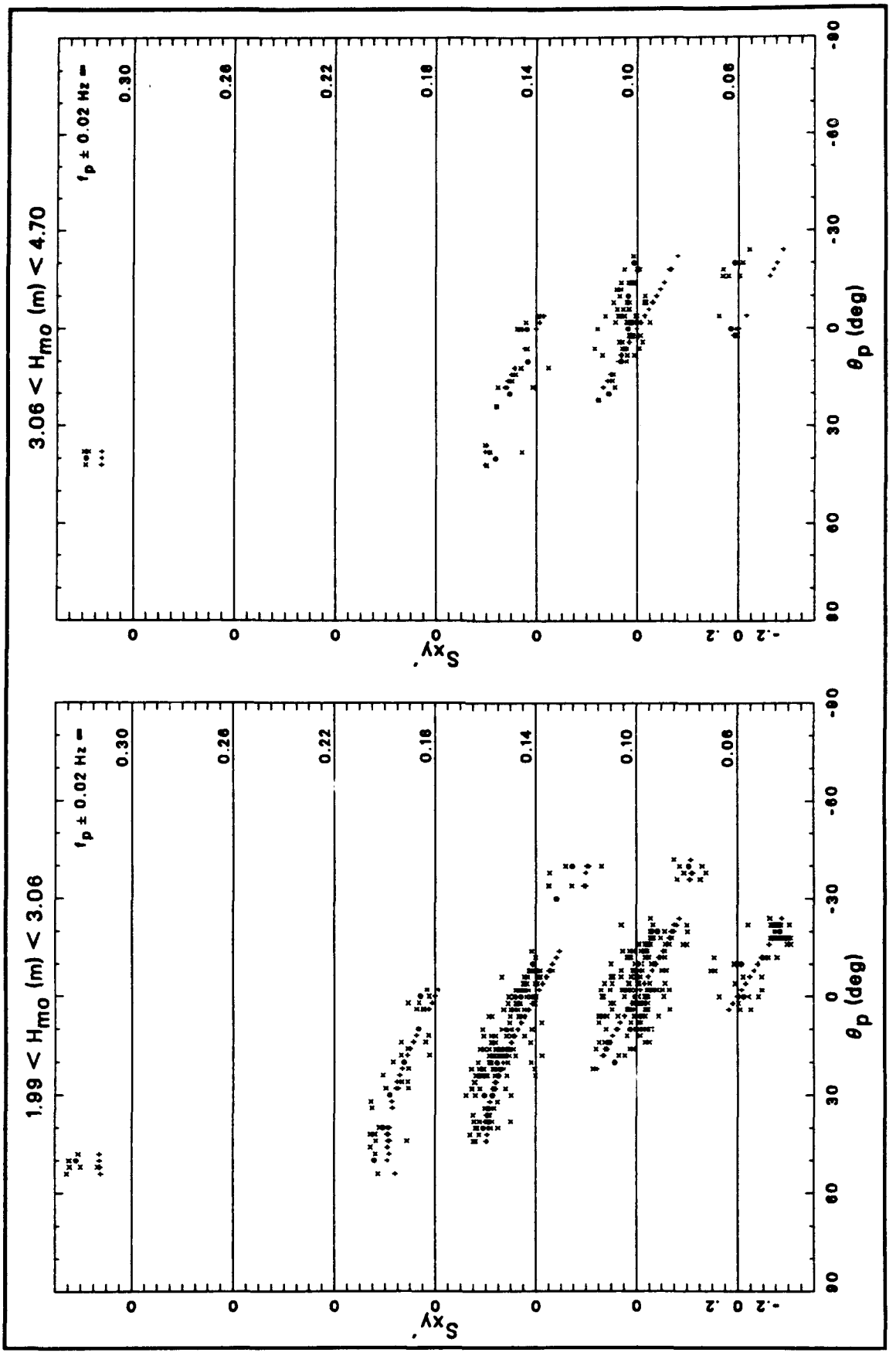

Figure 20. Estimates of S_{xy}' for wave heights between 1.99 and 4.70 m

As with the results for longshore energy flux, the groupings of + 's that represent unidirectional, monochromatic estimates follow simple sinusoidal patterns with rather small scatter. In terms of directional dependence, functional forms have maxima at 45 deg, minima at -45 deg, and zeros at 90, 0, and -90 deg. The amplitudes of the sinusoidal forms vary with frequency because of dependence on the ratio $C_g(f_p,d)/C(f_p,d)$. Some slight scatter in estimates is evident within (H_{mo},f_p,θ_p) classes, and is due to modest tidal variations in water depth.

In contrast with results for longshore energy flux, the curves for monochromatic, unidirectional estimates fall more nearly in the centers of clouds of x's that represent estimates from constituent frequency-direction spectra. This result indicates that there tends to be less bias in estimates based on monochromatic, unidirectional waves. On the other hand, the clouds of x's tend to scatter over broader ranges of S'_{xy}. This result indicates that estimates from individual frequency-direction spectra within a class are more sensitive to the specific nature of energy distributions within a spectrum than were corresponding estimates of longshore energy flux in Chapter 4.

Solid dots, which represent S'_{xy} estimates from characteristic spectra within a class, appear to correspond well with centers of the clouds of x's, suggesting that characteristic spectra can represent class averages of results from constituent spectra with reasonable verity. The solid dots are often, but not always, near the patterns of + 's of monochromatic, unidirectional estimates, again suggesting a reasonable correlation between these two measures of S'_{xy}.

Error analysis

To quantify the observations made in the last part of this chapter, correlations are computed for estimates from characteristic spectra with statistics from estimates of constituent spectra, and with class averages of unidirectional, monochromatic estimates. Also computed are biases in unidirectional, monochromatic estimates relative to characteristic spectra. These computations define a measure of the extent of errors incurred when using unidirectional, monochromatic estimates of S'_{xy}, and provide a means of making an optimum correction.

Figure 21 is a correlation of $S'_{xy,ll}$ (from Equation 31) with means and standard deviations of class groupings of constituent spectra in the form $\overline{S'_{xy,ll}} \pm S'_{xy,ll,\sigma}$ (from Equations 29 and 30, respectively). Symbols distinguish wave height classes, with high-energy (H_{mo} > 2 m) classes being shown as solid symbols. As anticipated, Figure 21 shows that $S'_{xy,ll}$ correlates very well with $\overline{S'_{xy,ll}}$, meaning that characteristic spectra can be used with considerable success to estimate the class average properties of the constituent spectra.

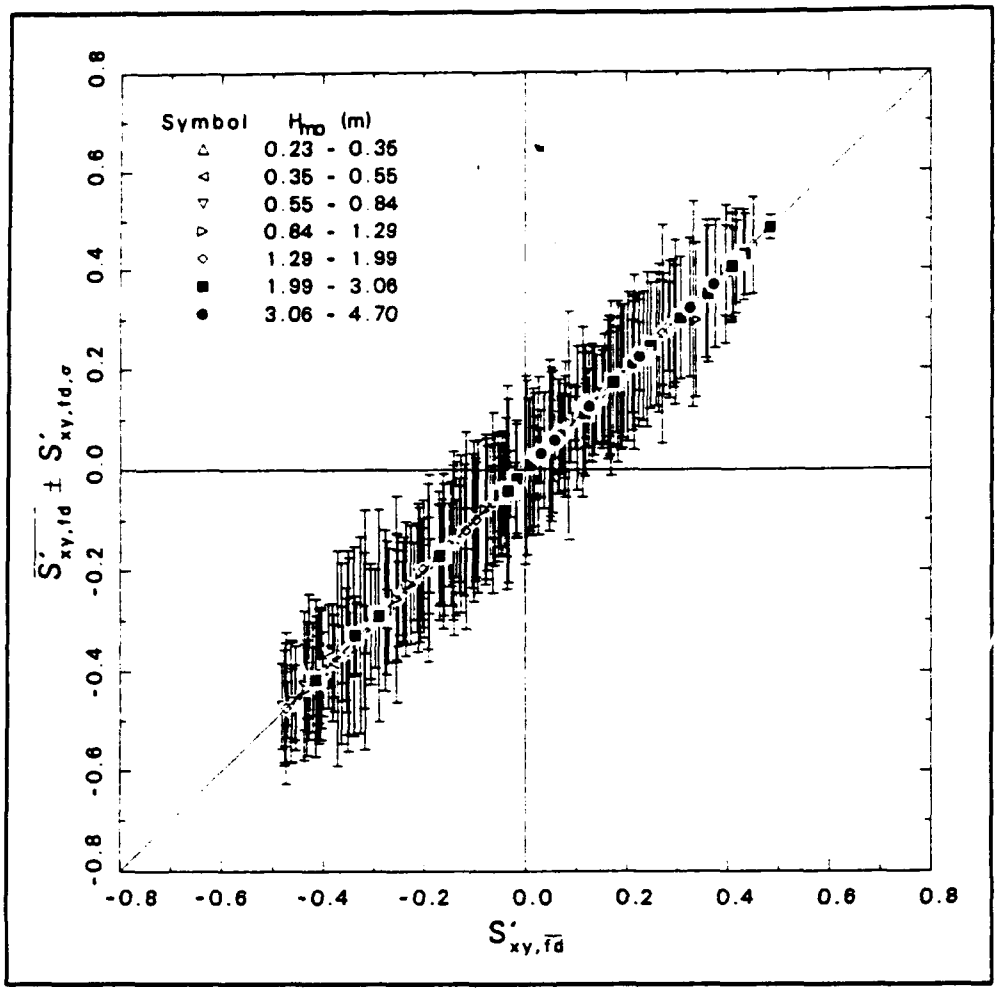

Figure 21. Correlation of S_{xy}' estimates from characteristic spectra with class statistics of constituent frequency-direction spectra

On the other hand, Figure 21 indicates that the variability of estimates within classes of constituent spectra is significant, as shown by the extent of the vertical lines representing $S'_{xy,fd,\sigma}$. There is no strong indication that the class standard deviations vary with the value of S'_{xy}, and Figure 21 indicates a nominal value of ± 0.15 as a representative standard deviation for the data set as a whole. This result shows the level of uncertainty in estimates where characteristic spectra are used. The uncertainty generally cannot be expressed as a percentage because S'_{xy} goes through zero. For estimates near zero, the level of uncertainty is of considerable importance because it can allow the sign of S'_{xy} to change in addition to very large percentage changes. A minimum percentage of uncertainty occurs at extreme values of S'_{xy}, and is about 30 percent for the data shown in Figure 21.

Figure 22 shows the correlation of S'_{xy} estimates from characteristic spectra ($S'_{xy,\overline{fd}}$, from Equation 31) with class-averaged unidirectional, monochromatic

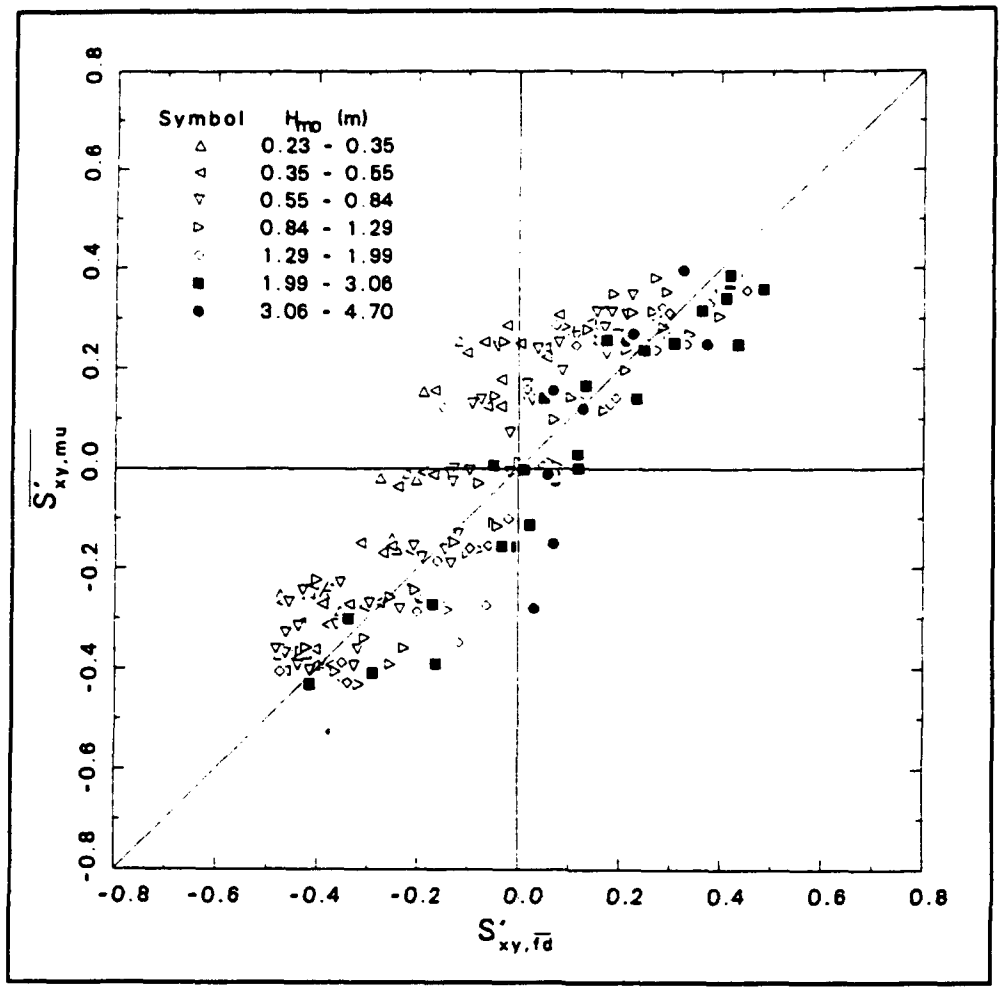

Figure 22. Correlation of S_{xy}' estimates from characteristic spectra with those of class averages of monochromatic, unidirectional spectra

estimates ($\overline{S'_{ij,mu}}$ from Equation 27). For the data set as a whole, the points scatter roughly evenly about the line of perfect correlation. Close examination of Figure 22 shows a tendency for monochromatic, unidirectional estimates to underestimate S'_{xy} relative to characteristic spectra at low characteristic wave heights, and, more important, to overestimate S'_{xy} for large wave heights. This property is not examined further here because the scatter of points is rather large for all wave heights, indicating that there is not a generally high correlation for the whole data set, and that methods of correction using the correlation in Figure 22 would have a large uncertainty.

A better approach to making corrections to monochromatic, unidirectional estimates is to compute and remove the biases so that the remaining uncertainty is only that associated with variability within classes. Figure 23 shows the computed biases, which are defined as $\overline{S'_{xy,mu}} - S'_{xy,\overline{fd}}$, as functions of direction-class center directions for all wave height and frequency classes. The bias patterns in Figure 23 are not quite as clearly defined as were the longshore

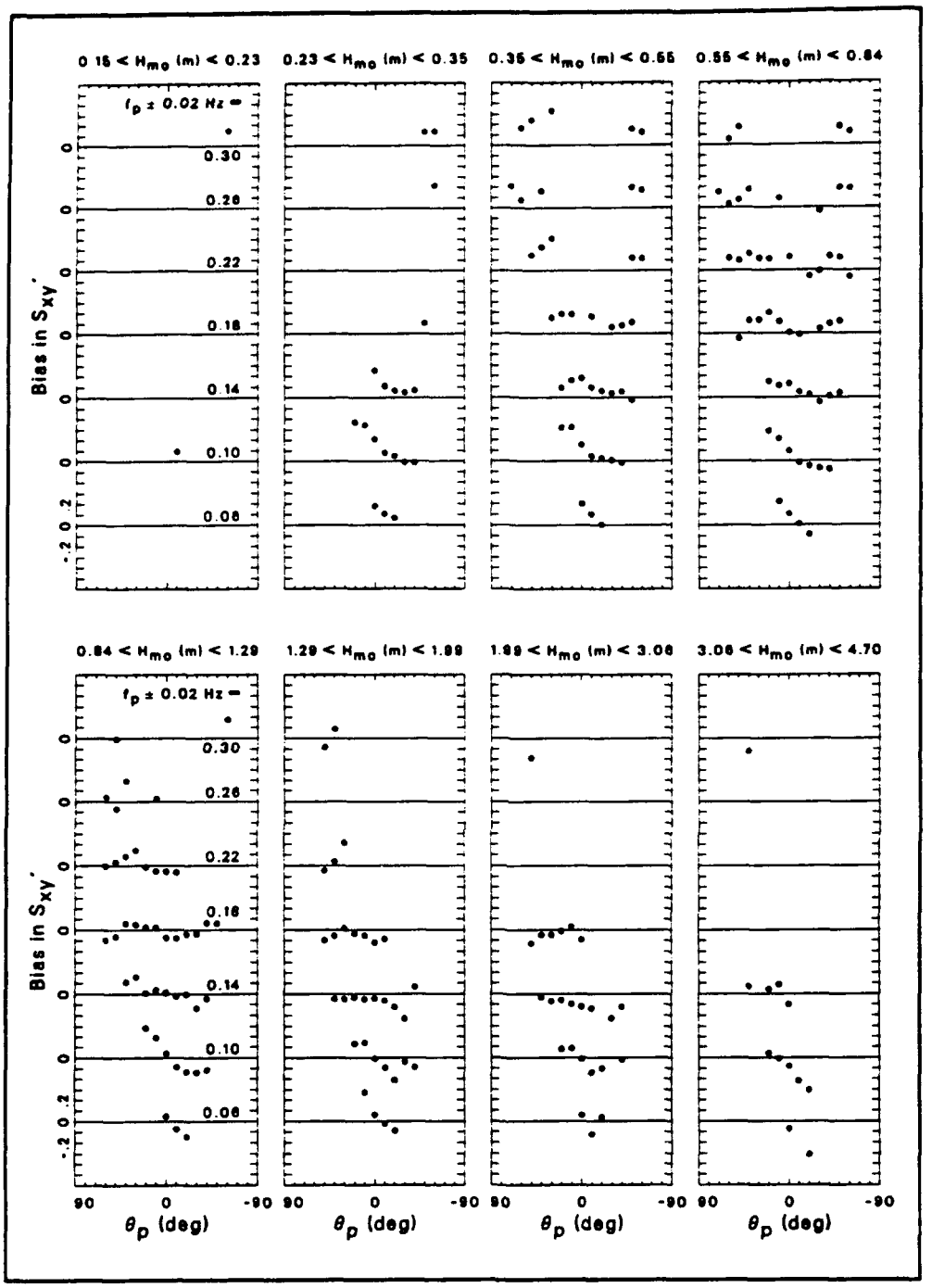

Figure 23. Bias in S_{xy}' estimates

energy flux biases of Figure 16, but there are some general tendencies. There is a tendency for the biases to be positive for low H_{mo}, negative for high H_{mo}, and often near zero for intermediate H_{mo}. At low f_p, there appears a tendency for a minimum bias at negative, intermediate θ_p, and a maximum bias at positive, intermediate θ_p. The pattern of points does not lend itself to ready, analytical description. However, Figure 23 can be used as graphical guidance for estimating bias.

S_{xy} predictor

To incorporate these results in an estimation scheme where all that is known is the characterizing parameter set (H_{mo}, f_p, θ_p), one would compute a monochromatic, unidirectional value, subtract the bias, and include a residual measure of uncertainty. Using $\hat{S}'_{xy}$ to represent such an estimate, the mathematical expression is

$$\hat{S}'_{xy} = \frac{C_g(f_p,d)}{C(f_p,d)} \cos\theta_p \sin\theta_p - bias(H_{mo},f_p,\theta_p) \pm 0.15 \qquad (33)$$

where $bias(H_{mo},f_p,\theta_p)$ is found from Figure 23, and the uncertainty is as evidenced in Figure 21. To create a dimensional estimate $\hat{S}_{xy}$, both sides of Equation 33 are multiplied by the normalizing factor $\rho g\sigma^2 = \rho g H_{mo}^2/16$, so that the result is in terms of the three characterizing parameters H_{mo}, f_p, and θ_p. The estimate takes the form

$$\hat{S}_{xy} = \rho g \frac{H_{mo}^2}{16} \left[\frac{C_g(f_p,d)}{C(f_p,d)} \cos\theta_p \sin\theta_p - bias(H_{mo},f_p,\theta_p) \pm 0.15 \right] \qquad (34)$$

where it is assumed that water density ρ and depth d are known.

Estimates of S_{xx} and S_{yy}

Patterns for the analyses of the other two radiation stress components are the same as for S'_{xy}. Results of these analyses are simply summarized here, and, to save space in the body of this report, supporting figures can be found in Appendix C. General mathematical forms for these two components are found by substituting the appropriate trigonometric functions and evaluating the delta functions in Equation 23. The form for S'_{xx} (or S'_{11}) becomes

$$S'_{xx} = \sum_{n=1}^{N} \sum_{m=1}^{M} \left[\left(\cos^2\theta_m + 1 \right) \frac{C_g(f_n,d)}{C(f_n,d)} - \frac{1}{2} \right] S'(f_n,\theta_m)\,\Delta\theta\,\Delta f \qquad (35)$$

and the form for S'_{yy} (or S'_{22}) becomes

$$S'_{yy} = \sum_{n=1}^{N} \sum_{m=1}^{M} \left[\left(\sin^2 \theta_m + 1 \right) \frac{C_g(f_n,d)}{C(f_n,d)} - \frac{1}{2} \right] S'(f_n,\theta_m) \, \Delta\theta \, \Delta f \quad (36)$$

Equations derived from Equations 25 to 31 for monochromatic, unidirectional estimates, constituent spectral estimates, characteristic spectral estimates, and their statistics also follow form when the appropriate trigonometric functions are substituted and delta functions evaluated. The reader can readily perform these operations, so the resulting equations are not listed here.

S_{xx} distributions

The onshore transport of onshore wave momentum represented by S'_{xx} tends always to be positive, with maxima near peak directions of 0 deg, and minima at extreme peak wave approach angles of 90 and -90 deg. This behavior is illustrated in Figures C1 to C4, which show the distributions of monochromatic, unidirectional estimates $S'_{xx,mu,i}$ (+'s), constituent spectral estimates $S'_{xx,fd,i}$ (x's), and characteristic spectral estimates $S'_{xx,\overline{fd}}$ (solid dots) for all cases in the database. These figures show a tendency for monochromatic, unidirectional estimates to be higher than the cloud of points representing spectral estimates near peak directions of 0 deg, and to be lower at high wave approach angles.

Figure C5 shows the correlation of characteristic spectral estimates $S'_{xx,\overline{fd}}$ with the class means and standard deviations of constituent spectral estimates in the form $\overline{S'_{xx,fd}} \pm S'_{xx,fd,\sigma}$, and indicates that class mean values are well-represented by those of characteristic spectra. Figure C5 also indicates a general uncertainty of estimates within a class of about ± 0.1, which can be expressed as a percentage error ranging from about 20 percent for small S'_{xx} to about 9 percent for large S'_{xx}. Figure C6 shows the correlation of characteristic spectral estimates with class means of monochromatic, unidirectional estimates, and emphasizes the tendency for monochromatic, unidirectional estimates to be high for large S'_{xx} and low for small S'_{xx}. This tendency is quantified class by class in Figure C7, which shows the empirical bias function of monochromatic, unidirectional class averages relative to characteristic spectra, defined as $\overline{S'_{xx,mu}} - S'_{xx,\overline{fd}}$.

S_{xx} predictor

These results lead to a method of estimation of S'_{xx} when all that is known is the characteristic parameter set (H_{mo},f_p,θ_p). Designated $\hat{S}'_{xx}$, this estimate is

$$S'_{xx} = \left(\cos^2 \theta_p + 1 \right) \frac{C_g(f_p,d)}{C(f_p,d)} - \frac{1}{2} - bias(H_{mo},f_p,\theta_p) \pm 0.1 \qquad (37)$$

and the dimensional form S_{xx} is

$$S_{xx} = \rho g \frac{H_{mo}^2}{16} \left[\left(\cos^2 \theta_p + 1 \right) \frac{C_g(f_p,d)}{C(f_p,d)} - \frac{1}{2} - bias(H_{mo},f_p,\theta_p) \pm 0.1 \right] \qquad (38)$$

when both sides of Equation 37 are multiplied by the normalization factor $\rho g \sigma^2 = \rho g H_{mo}^2/16$.

S_{yy} distributions

The behavior of S'_{yy}, the alongshore transport of longshore momentum, is somewhat like the behavior of S'_{xx}, the exception being that the trigonometric functional form is $\sin^2 \theta$ for S'_{yy} instead of $\cos^2 \theta$. This difference causes S'_{yy} to have minima near peak wave approach angles of 0 deg, and maxima at approach angles of 90 and -90 deg. This behavior is shown in Figures C8 to C11, which show monochromatic, unidirectional estimates $S'_{yy,mu,i}$ (+'s), constituent spectral estimates $S'_{yy,fd,i}$ (x's), and characteristic spectral estimates $S'_{yy,JB}$ (solid dots) for all cases. For this component of radiation stress, monochromatic, unidirectional estimates tend to underestimate spectral estimates for small peak wave approach angles, and to overestimate spectral estimates at large approach angles.

Figure C12 shows the correlation of characteristic spectral estimates $S'_{yy,JB}$ with the constituent spectral class means and standard deviations in the form $\overline{S'_{yy,fd}} \pm S'_{yy,fd,\sigma}$. As for the other radiation stress components, this figure shows that $\overline{S'_{yy,fd}}$ is very well represented by $S'_{yy,JB}$, and that the class uncertainty is reasonably uniform for the full range of S'_{yy}, but the level of uncertainty is smaller than for S'_{xx}, being about ± 0.05. Figure C13 shows the correlation of $S'_{yy,JB}$ with $\overline{S'_{yy,mu}}$, and indicates the tendency for monochromatic, unidirectional estimates to be high for large S'_{yy}, and low for small S'_{yy}, much like the behavior for S'_{xx} in Figure C6. Figure C14 quantifies the bias $\overline{S'_{yy,mu}} - S'_{yy,JB}$ as computed for all data classes, and shows the bias to be rather well-behaved.

S_{yy} predictor

A predictor $\hat{S}'_{yy}$ for dimensionless longshore transport of longshore wave momentum evolves from these results in the form

$$\hat{S}'_{yy} = \left(\sin^2 \theta_p + 1 \right) \frac{C_g(f_p,d)}{C(f_p,d)} - \frac{1}{2} - bias(H_{mo},f_p,\theta_p) \pm 0.05 \qquad (39)$$

The dimensional form $\hat{S}_{yy}$ becomes

$$\hat{S}_{yy} = \rho g \frac{H_{mo}^2}{16} \left[\left(\sin^2 \theta_p + 1 \right) \frac{C_g(f_p,d)}{C(f_p,d)} - \frac{1}{2} - bias(H_{mo},f_p,\theta_p) \pm 0.05 \right] \qquad (40)$$

when both sides of Equation 39 are multiplied by the normalization factor $\rho g \sigma^2 = \rho g H_{mo}^2/16$.

Discussion

Equations 34, 38, and 40 are the optimum estimates of S_{xy}, S_{xx}, and S_{yy}, respectively, in terms of the analysis approach used here. Bias removal converts the estimates to class averages of constituent frequency-direction spectra, or, very nearly equivalently, estimates from class characteristic spectra. The remaining uncertainties are not reducible if only three characterizing parameters are used to describe the wave field. It is likely that confidence intervals can be reduced if more parameters are employed to describe the constituent spectra. This last statement is an iteration of the comment made in Chapter 4, and means that an incomplete description of the wave field must necessarily result in considerable uncertainty in the estimation of wave field properties.

Also iterated here is the point that these results are specific to the FRF and, possibly, similar sites. A similar site would be characterized by adjacency to a broad, shallow continental shelf with the ocean subject to wind forcing by frontal systems oriented along a diagonal to the shoreline. While these results are not intended for general engineering use, they do emphasize the broad truth that rather significant errors can occur when dynamically important properties are estimated from poorly characterized wave fields.

An advantage of the present results is that a quantifiable estimate of error can be assigned to radiation stress estimates in instances where these results might apply. If these results are used in a project of broader scope, one can examine the consequences of estimation uncertainty on the project as a whole,

and, perhaps, employ a compensating safety factor. Because these results show the uncertainties to be frequently rather large, it is very clear that improved estimation of radiation stress components is possible only with more knowledge of the wave field than the three-parameter set (H_{m_0}, f_p, θ_p) that is commonly used. Measures of such things as directional spread and multiple modes would greatly enhance the spectral classification scheme, and the result would be rather smaller error bars on estimates of radiation stresses.

6 Conclusion

The intent of this report has been to examine a 5-year, 6,759-case database of high-resolution frequency-direction spectra for three interrelated properties, all based on classification of the spectra by three parameters: characteristic wave height, spectral peak frequency, and spectral peak direction. The first property is the general distribution of the observed spectra in wave height-frequency-direction space. Second is the definition of characteristic spectra to represent the various classes of height, frequency, and direction. Third is an examination of estimation methods for and variability of some direction-sensitive wave properties to determine the consequences of using monochromatic, unidirectional waves or characteristic spectra in lieu of observed spectra in the estimates.

The spectra are classified as being in one of eight geometrically spaced wave height groups, one of seven regularly spaced frequency bands, and one of nineteen regularly spaced direction bins. Counting the number of spectra in each class showed that low-energy wave fields with high peak frequencies tend to arrive from high approach angles relative to shore-normal. Those with intermediate peak frequencies have approach angles closer to shore-normal. Low-energy wave fields with low peak frequencies tend to arrive primarily from slightly south of shore-normal, the direction of nearest approach of the continental shelf break. High-energy spectra tend to have low peak frequencies and had peak directions centered more nearly around shore-normal, as is expected due to the process of refraction.

None of these results are surprising, though the percentage of occurrence estimates may help in climatological studies of wave field behavior. For example, the high percentage of low-energy southerly swell, which is often associated with nearshore sediment accretion, might be related to the low percentage of high-energy spectra that are usually credited with beach erosion. Quantitative models of subtle, direction-dependent behavior in the dynamic erosion-accretion balance might be developed when these results are used in conjunction with bathymetric survey data.

Computing averages of constituent spectra within classes has provided representative or characteristic spectra for each class. Directional energy distributions of these characteristic spectra reveal the frequent occurrence of skewed or multimodal shapes. Such shapes can have a strong effect on nearshore processes driven by these waves, and suggest that simple models of

continental shelf wave generation and transformation may be inadequate to account for these observations.

The characteristic spectra found in this study are expected to be of considerable use to modelers of nearshore processes, wave generation, and wave transformation. For example, in all of the high-energy spectral classes, the characteristic spectra show distinctive features that not only persist through individual storms, but also appear in the same form from storm to storm. These spectra have directionally broad low-frequency energy peaks and well-defined, directionally bimodal high frequency spectral tails. This characteristic shape is different from what is expected of a nearshore spectrum, which is usually narrow-banded in direction due to refractive processes. Because these spectra occur at high energy, seeking physical explanations for them is an important topic for future research, as are the consequences for nearshore processes being driven by waves having this unique spectral signature.

Along with averages of constituent spectra, standard deviations of constituent spectra are also discussed. Standard deviation spectra are found to be of comparable size and shape to their corresponding mean spectra. Part of the variation is due to the rather broad frequency bands and direction bins used to define spectral classes. This situation allows constituent spectra of several peak frequencies or peak directions to exist in the same class, and can cause significant variability as measured by the standard deviation spectra.

The remainder of the variation is due to subtleties in spectral shape not distinguished in a simple, three-parameter classification. Directional side lobes and relatively low-level secondary energy modes exist in some spectra, but not in others. Though secondary relative to spectral peak parameters, these features can have significant effects on direction-sensitive, integral properties of the spectra, such as longshore energy fluxes and radiation stresses. More refined spectral classification can reduce the variability due to these features by using additional characterizing parameters to account for such things as directional spread and secondary modal structure. Though beyond the scope of the present study, such an effort is highly recommended for future work.

The final part of this study is a rather laborious, but quite insightful examination of the consequences of using both monochromatic, unidirectional waves and characteristic spectra to estimate longshore energy flux and radiation stress tensor components in light of distributions of estimates from constituent spectra. It is found that, without correction, monochromatic, unidirectional waves typically produce estimates with large errors, and, in the cases of longshore energy flux and onshore transport of longshore momentum, can even result in estimates with the wrong sign. These are serious errors, and would invalidate models of sediment transport and nearshore currents that commonly rely on these properties.

An optimum correction is found for monochromatic, unidirectional estimates of longshore energy flux and radiation stresses. The correction consists of adjusting the estimate for the empirically derived bias of the monochromat-

ic, unidirectional estimate relative to either the mean of the constituent spectral estimates within a class or, nearly equivalently, the estimate from the class characteristic spectrum. The correction is optimum because it adjusts the estimate to the most probable value for the class, and cannot be refined further because all three dimensions of the analysis space (wave height, period, and direction) are required to define the bias.

Considerable uncertainty remains in the corrected estimates, however, because some direction-sensitive details of the constituent spectra cannot be discerned in a three-parameter spectral characterization. The magnitude of the remaining uncertainty is very important because it still allows estimates of longshore energy flux and onshore transport of longshore momentum to be of opposite sign from the true values. This property of the results reemphasizes the need for characterizations of a wave field that are more refined than the commonly used three parameters. If wave conditions are to be defined with a limited set of parameters, the set must include enough information to distinguish such things as directionally broad from narrow spectra, multiple modes, and significant directional side lobes of energy.

Perhaps the most important result of this study is the general conclusion that characterizing wave conditions at the FRF with only three parameters is unduly restrictive. If accurate modeling and engineering computations are to be performed, the absolute maximum amount of available directional information must be employed; commonly computed, direction-dependent wave properties are just too sensitive to directional energy definition to rely on low-resolution wave field characterization. This conclusion implies that where a directional wave gauge is deployed, low-resolution analysis is likely to result in a poorly described wave field, and the problems found in this study will not be solved. Hence, it is recommended that high-resolution analysis techniques be used with directional wave gauges of any style in order to minimize uncertainties in direction-sensitive wave processes.

Finally, it is re-emphasized that the specific directional nature of nearshore waves discussed in this report is true only at the FRF site where measurements were made. Some of the properties described in this report may apply at sites having forcing and boundary conditions similar to those at the FRF, but are not likely to be generally applicable. However, the broader indications of this study are more universal: a three-parameter characterization of wave energy spectra is likely to be unduly restrictive, with direction-sensitive wave properties suffering from egregiously large error bars. Considerable mitigation of this problem is possible either with added parametric descriptions of wave spectra or the direct use of highly resolved spectra.

References

Birkemeier, W. A., Miller, H. C., Wilhelm, S. D., DeWall, A. E., and Gorbics, C. S. (1985). "A user's guide to the Coastal Engineering Research Center's (CERC's) Field Research Facility," Technical Report CERC-85-1, U.S. Army Engineer Waterways Experiment Station, Vicksburg, MS.

Corson, W. D., Resio, D. T., and Vincent, C. L. (1980). "Wave information study of U. S. coastlines; Surface pressure field reconstruction for wave hindcasting purposes," Technical Report HL-80-11, U.S. Army Engineer Waterways Experiment Station, Vicksburg, MS.

Crowson, R. A., Birkemeier, W. A., Klein, H. M., and Miller, H. C. (1988). "SUPERDUCK nearshore processes experiment: Summary of studies, CERC Field Research Facility," Technical Report CERC-88-12, U.S. Army Engineer Waterways Experiment Station, Vicksburg, MS.

Davis, R. E., and Regier, L. A. (1977). "Methods for estimating directional wave spectra from multi-element arrays," *Journal of Marine Research* 35, 453-477.

Horikawa, K., ed. (1988). *Nearshore dynamics and coastal processes*. University of Tokyo Press.

Howell, G. L. (1992). "A new nearshore directional wave gage," *Proceedings of the 23rd International Conference on Coastal Engineering*, American Society of Civil Engineers, October, 1992, Venice, Italy, 1-13.

Long, C. E., and Oltman-Shay, J. M. (1991). "Directional characteristics of waves in shallow water," Technical Report CERC-91-1, U.S. Army Engineer Waterways Experiment Station, Vicksburg, MS.

Long, C. E. (in preparation). "Storm evolution of directional seas in shallow water," U.S. Army Engineer Waterways Experiment Station, Vicksburg, MS.

Longuet-Higgins, M. S., and Stewart, R. W. (1964). "Radiation stress in water waves, a physical discussion with application," *Deep Sea Research*, 11, 529.

Oppenheim, A. V., and Schafer, R. W. (1975). *Digital signal processing*. Prentice-Hall, Englewood Cliffs, NJ.

Pawka, S. S. (1982). "Wave directional characteristics on a partially sheltered coast," Ph.D. dissertation, Scripps Institution of Oceanography, University of California, San Diego, CA.

_____. (1983). "Island shadows in wave directional spectra," *Journal of Geophysical Research* 88, 2579-2591.

Thornton, E. B., and Guza, R. T. (1989). "Nearshore circulation." *Nearshore sediment transport*. R. J. Seymour, ed., Plenum, New York.

Shore Protection Manual. (1984). 4th Edition, 2 Vols, U.S. Army Engineer Waterways Experiment Station, Coastal Engineering Research Center, U.S. Government Printing Office, Washington, DC.

Appendix A
Plots of Characteristic Spectra

This appendix contains illustrations of mean or characteristic normalized spectra $\overline{S}'(f_n,\theta_m)$ defined by Equation 7 in Chapter 3 for all (H_{mo},f_p,θ_p) parametric classes for which data are available. Plots are grouped such that two or more consecutive pages represent a single wave height class. Each page contains four direction classes within its wave height class, and all frequency classes corresponding to the height and direction classes. Spaces for classes with too few cases to average are included to preserve the matrix form of this display. To save space, plot axes are not labelled. However, all spectra are plotted to the same scale, and axis scales are as shown in Figure A1, which can be used as a template for axis notation.

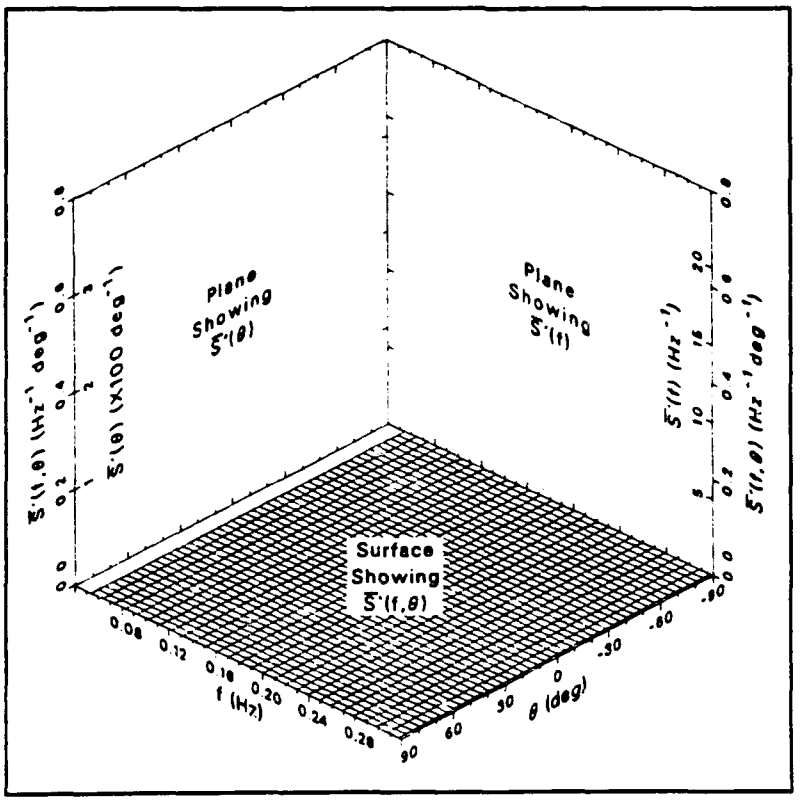

Figure A1. Axis label template

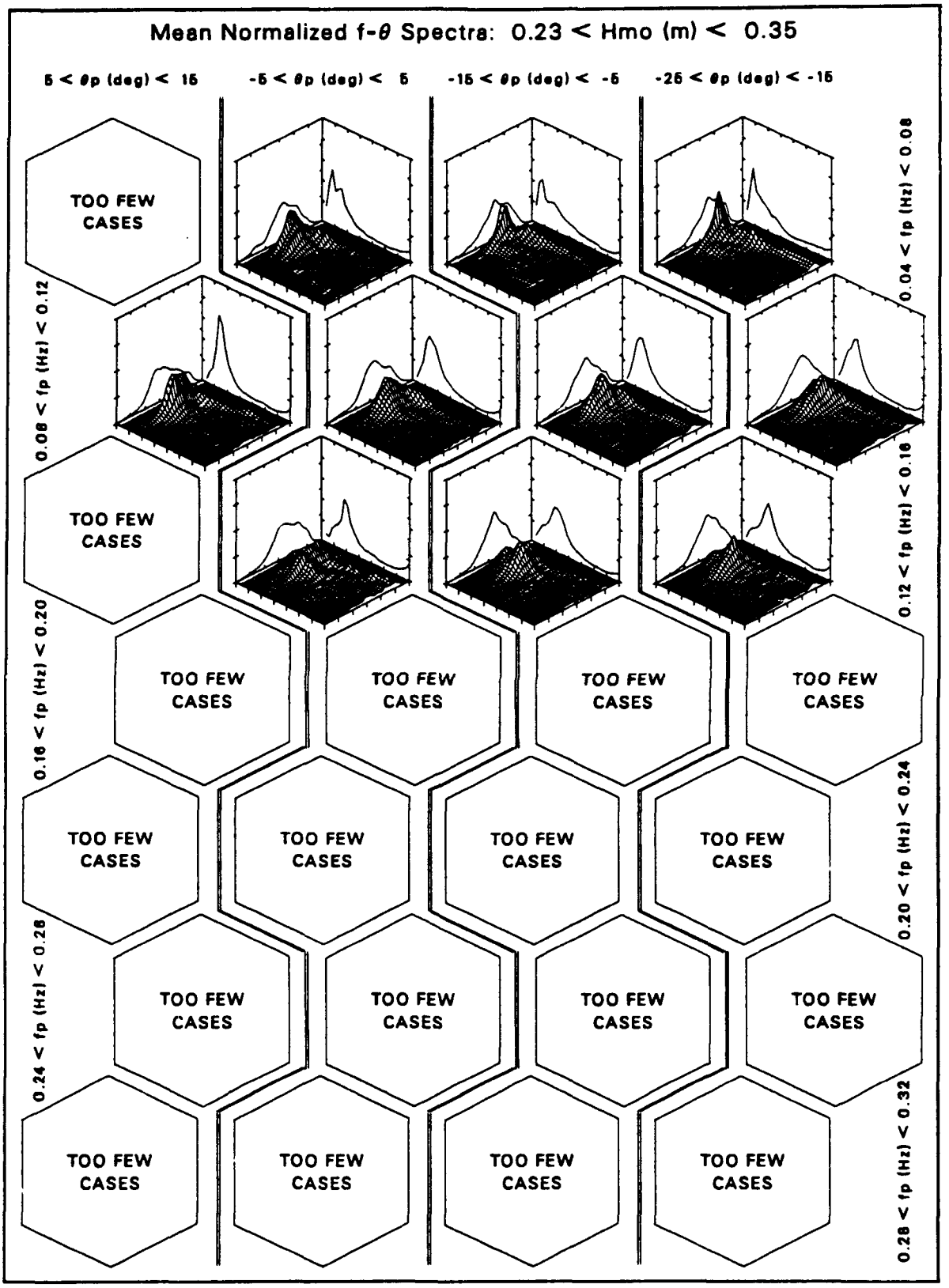
Mean Normalized f-θ Spectra: 0.23 < Hmo (m) < 0.35
5 < θp (deg) < 15
-5 < θp (deg) < 5
-15 < θp (deg) < -5
-25 < θp (deg) < -15
0.04 < fp (Hz) < 0.08
0.08 < fp (Hz) < 0.12
0.12 < fp (Hz) < 0.16
0.16 < fp (Hz) < 0.20
0.20 < fp (Hz) < 0.24
0.24 < fp (Hz) < 0.28
0.28 < fp (Hz) < 0.32
TOO FEW CASES

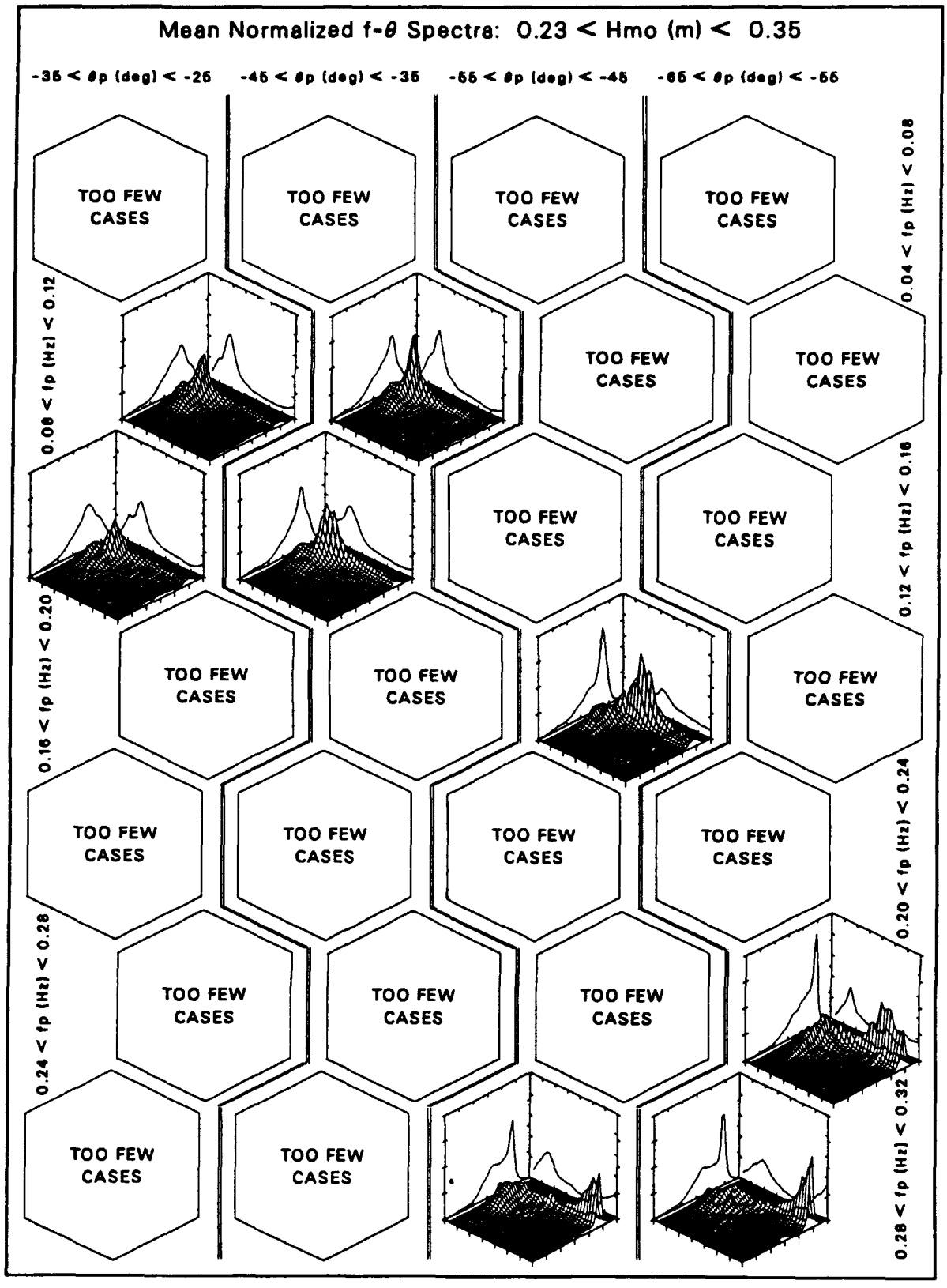
Mean Normalized f-θ Spectra: 0.23 < Hmo (m) < 0.35
-35 < θp (deg) < -25
-45 < θp (deg) < -35
-55 < θp (deg) < -45
-65 < θp (deg) < -55
0.04 < fp (Hz) < 0.08
0.08 < fp (Hz) < 0.12
0.12 < fp (Hz) < 0.16
0.16 < fp (Hz) < 0.20
0.20 < fp (Hz) < 0.24
0.24 < fp (Hz) < 0.28
0.28 < fp (Hz) < 0.32
TOO FEW CASES

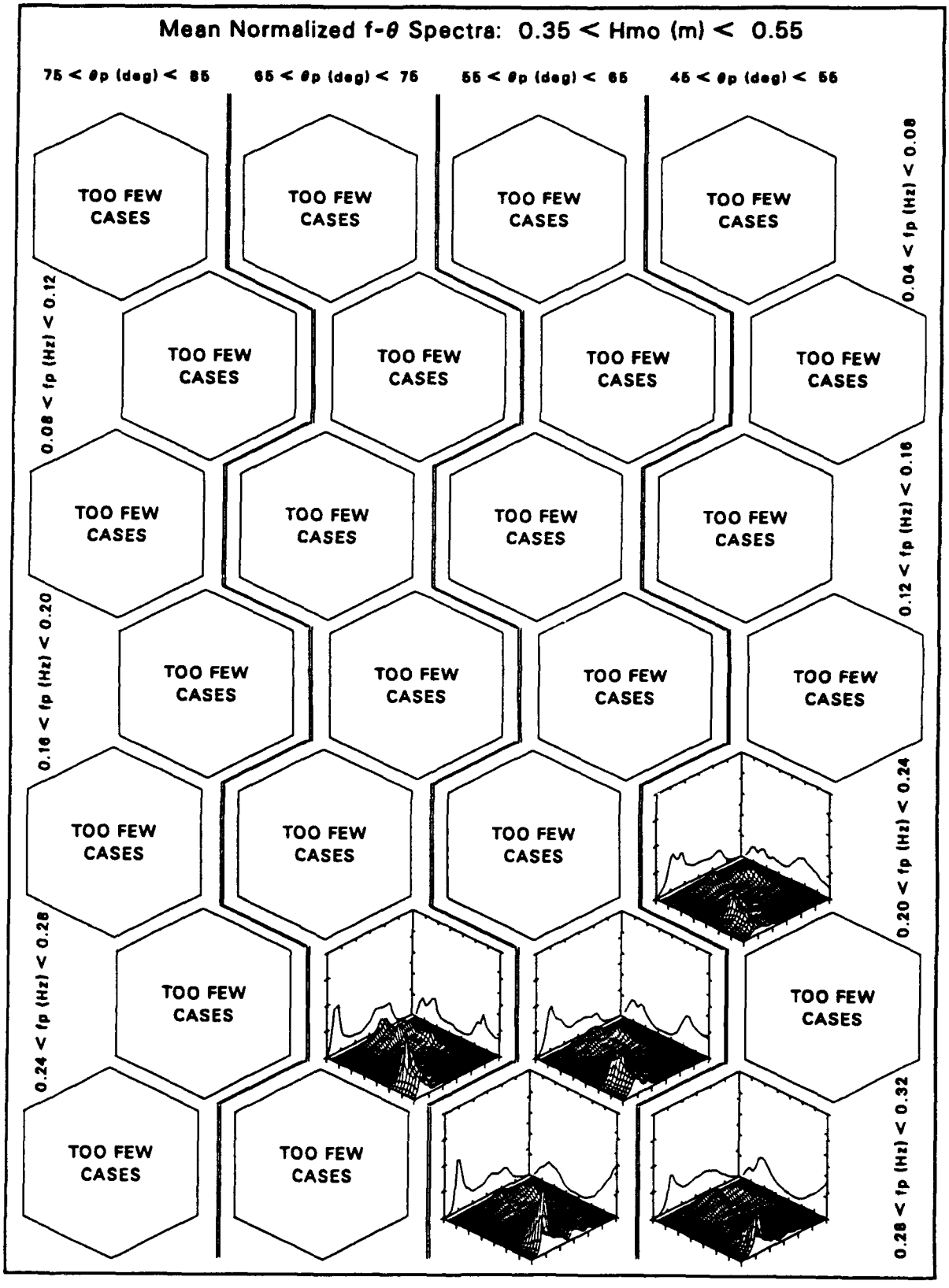
Mean Normalized f-θ Spectra: 0.35 < Hmo (m) < 0.55
75 < θp (deg) < 85
65 < θp (deg) < 75
55 < θp (deg) < 65
45 < θp (deg) < 55
0.04 < fp (Hz) < 0.08
0.08 < fp (Hz) < 0.12
0.12 < fp (Hz) < 0.16
0.16 < fp (Hz) < 0.20
0.20 < fp (Hz) < 0.24
0.24 < fp (Hz) < 0.28
0.28 < fp (Hz) < 0.32
TOO FEW CASES

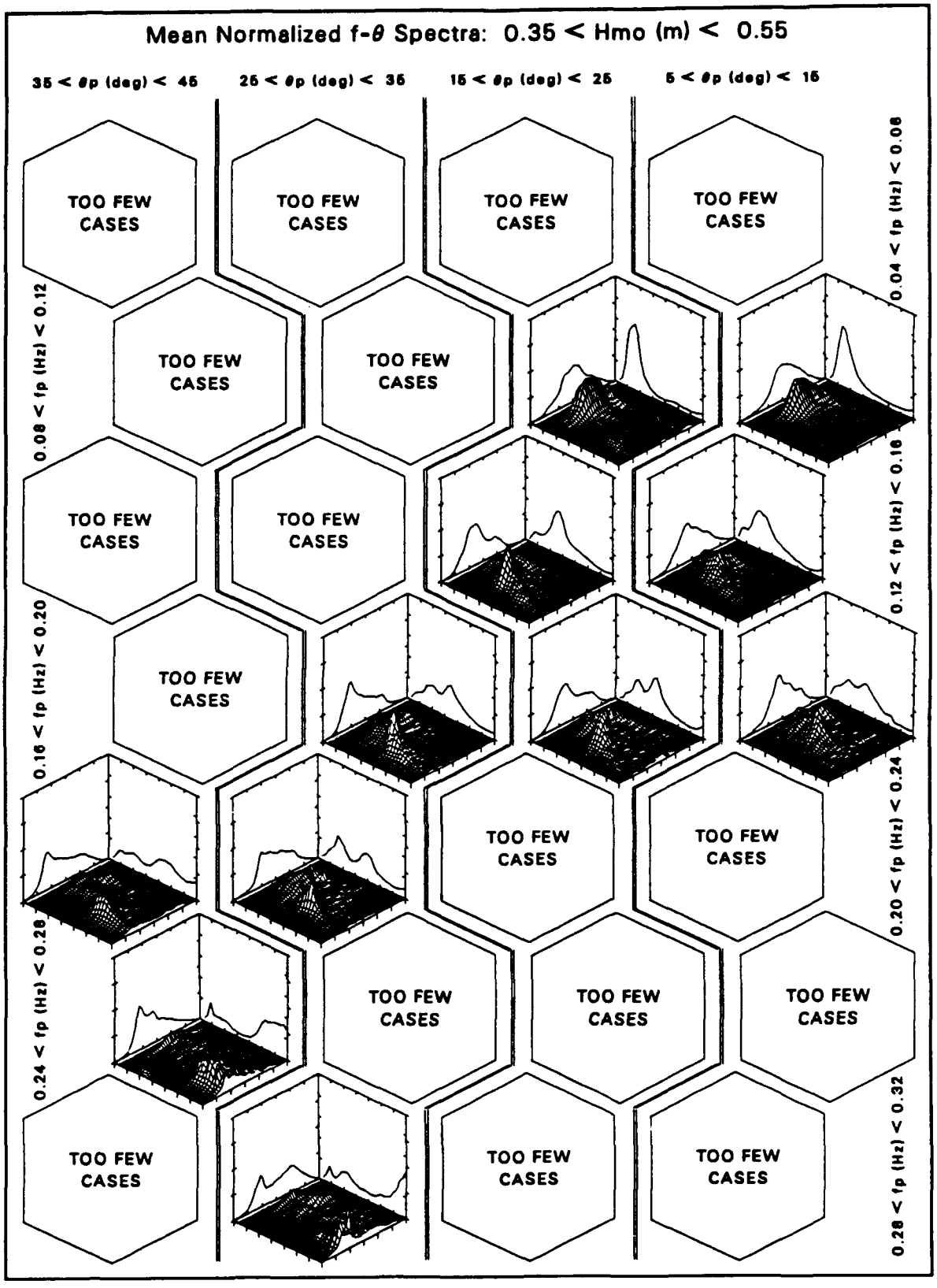
Mean Normalized f-θ Spectra: 0.35 < Hmo (m) < 0.55
35 < θp (deg) < 45
25 < θp (deg) < 35
15 < θp (deg) < 25
5 < θp (deg) < 15
0.04 < fp (Hz) < 0.08
0.08 < fp (Hz) < 0.12
0.12 < fp (Hz) < 0.16
0.16 < fp (Hz) < 0.20
0.20 < fp (Hz) < 0.24
0.24 < fp (Hz) < 0.28
0.28 < fp (Hz) < 0.32
TOO FEW CASES

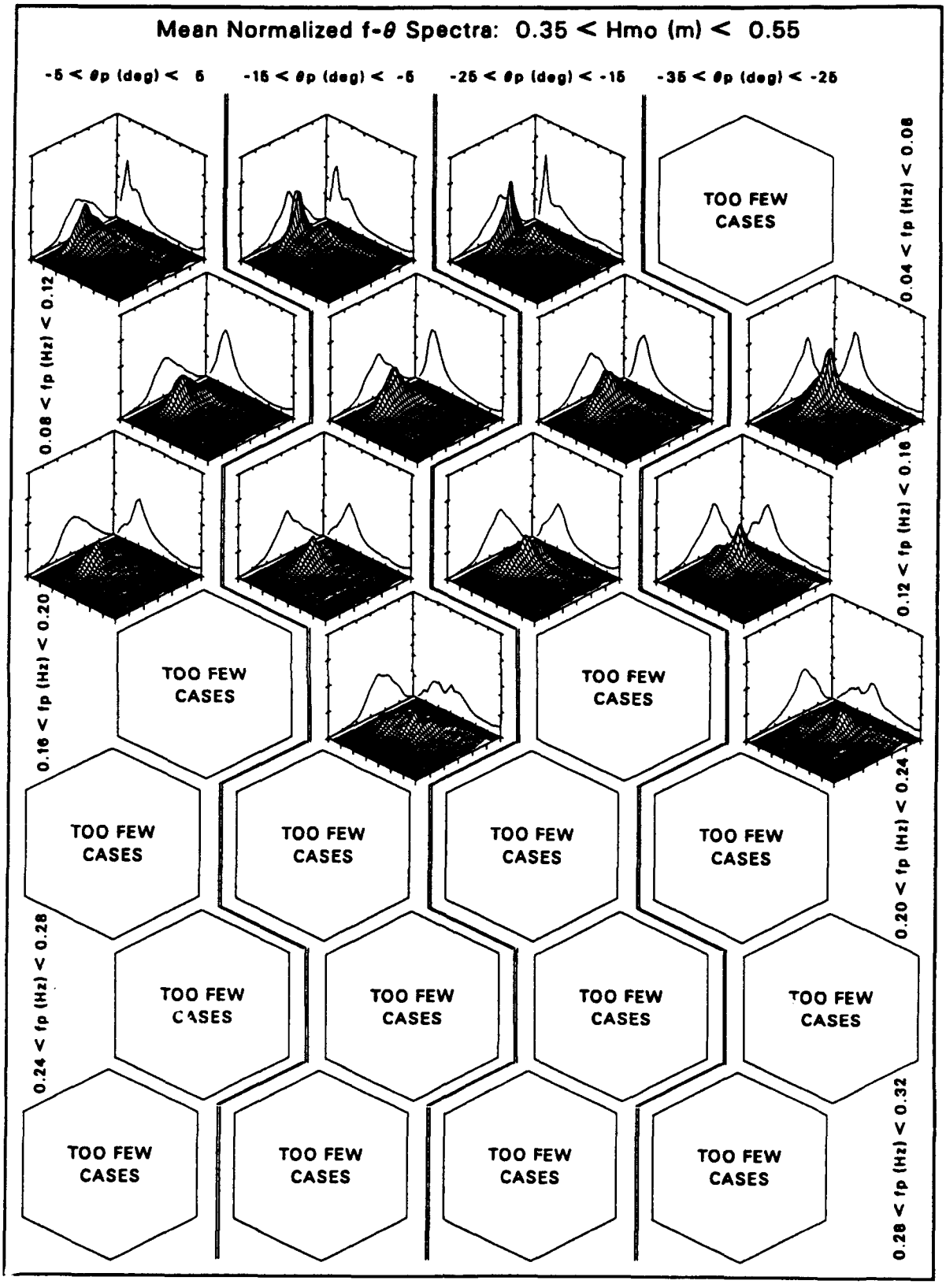
Mean Normalized f-θ Spectra: 0.35 < Hmo (m) < 0.55
-5 < θp (deg) < 5
-15 < θp (deg) < -5
-25 < θp (deg) < -15
-35 < θp (deg) < -25
0.04 < fp (Hz) < 0.08
0.08 < fp (Hz) < 0.12
0.12 < fp (Hz) < 0.16
0.16 < fp (Hz) < 0.20
0.20 < fp (Hz) < 0.24
0.24 < fp (Hz) < 0.28
0.28 < fp (Hz) < 0.32
TOO FEW CASES

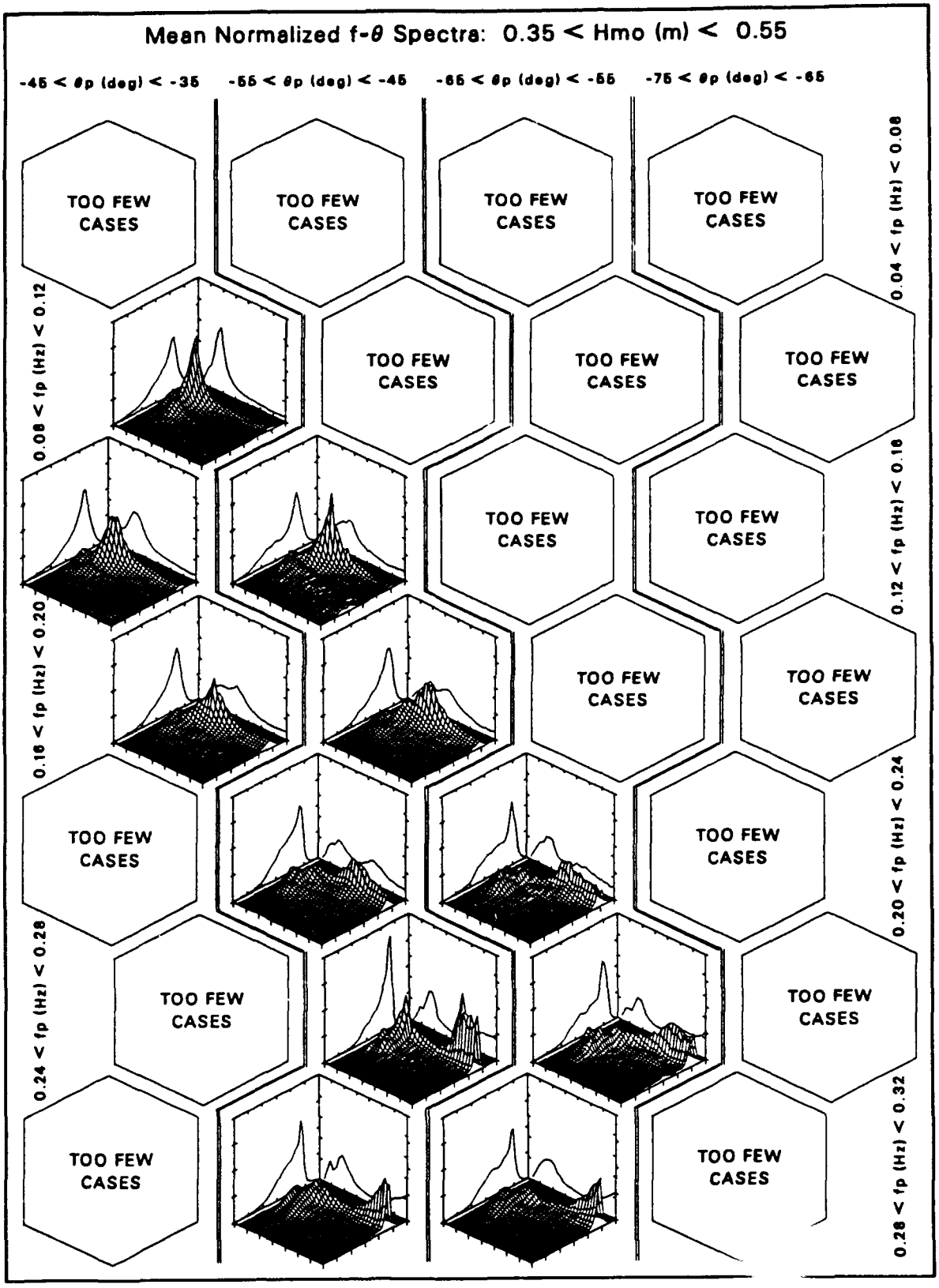
Mean Normalized f-θ Spectra: 0.35 < Hmo (m) < 0.55
-45 < θp (deg) < -35
-55 < θp (deg) < -45
-65 < θp (deg) < -55
-75 < θp (deg) < -65
0.04 < fp (Hz) < 0.08
0.08 < fp (Hz) < 0.12
0.12 < fp (Hz) < 0.16
0.16 < fp (Hz) < 0.20
0.20 < fp (Hz) < 0.24
0.24 < fp (Hz) < 0.28
0.28 < fp (Hz) < 0.32
TOO FEW CASES

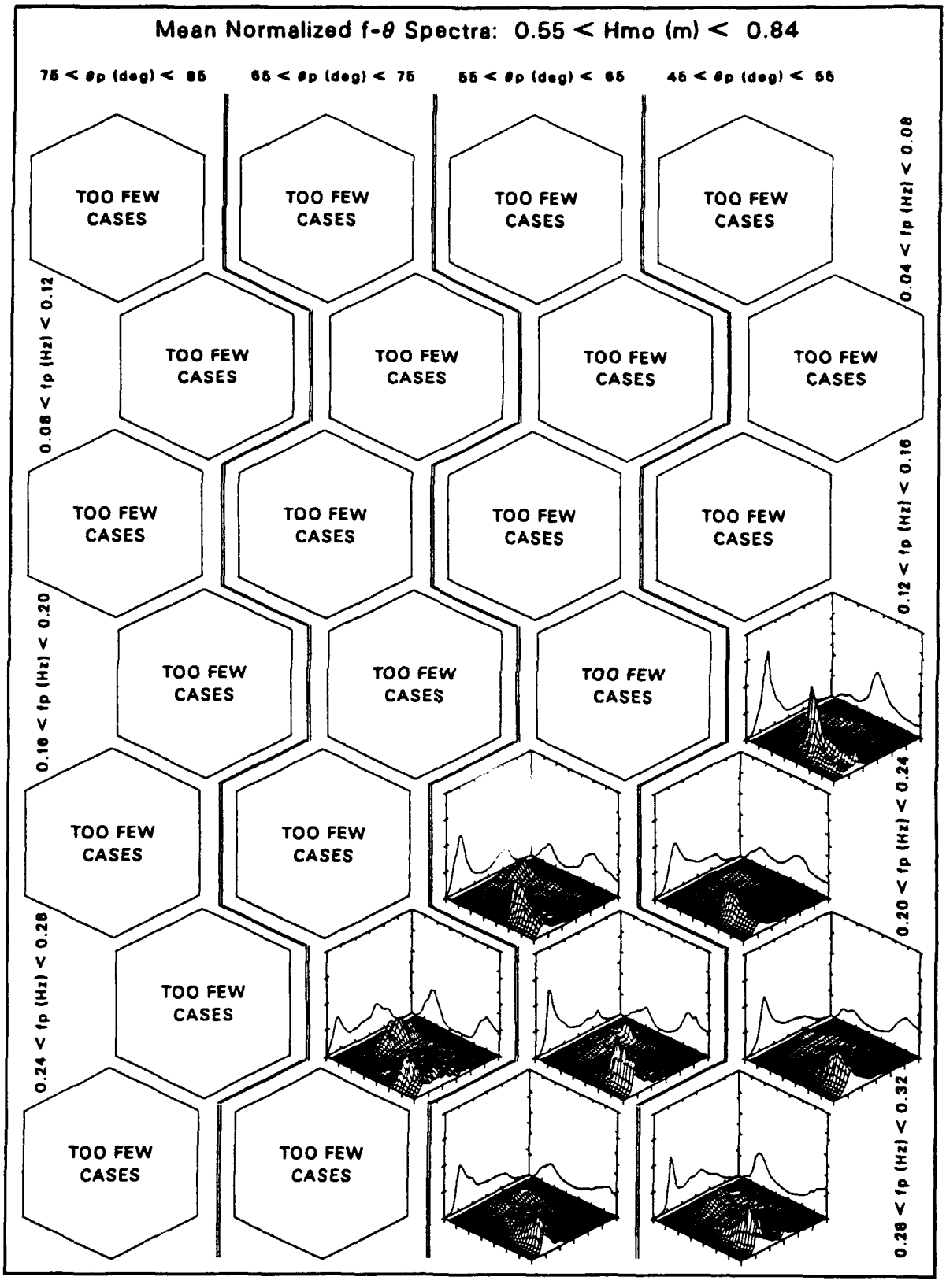
Mean Normalized f-θ Spectra: 0.55 < Hmo (m) < 0.84
75 < θp (deg) < 85
65 < θp (deg) < 75
55 < θp (deg) < 65
45 < θp (deg) < 55
0.04 < fp (Hz) < 0.08
0.08 < fp (Hz) < 0.12
0.12 < fp (Hz) < 0.16
0.16 < fp (Hz) < 0.20
0.20 < fp (Hz) < 0.24
0.24 < fp (Hz) < 0.28
0.28 < fp (Hz) < 0.32
TOO FEW CASES

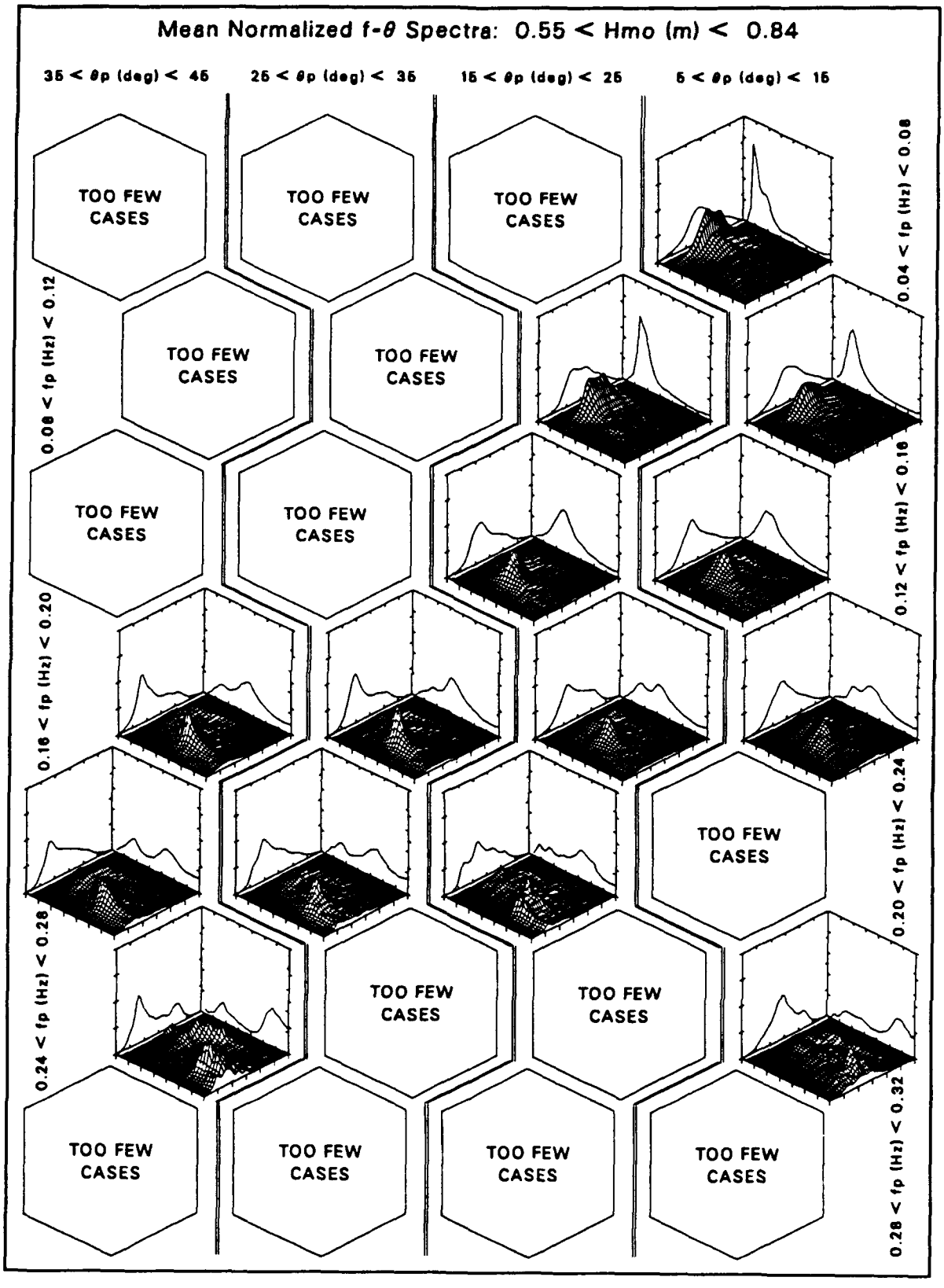
Mean Normalized f-θ Spectra: 0.55 < Hmo (m) < 0.84
35 < θp (deg) < 45
25 < θp (deg) < 35
15 < θp (deg) < 25
5 < θp (deg) < 15
0.04 < fp (Hz) < 0.08
0.08 < fp (Hz) < 0.12
0.12 < fp (Hz) < 0.16
0.16 < fp (Hz) < 0.20
0.20 < fp (Hz) < 0.24
0.24 < fp (Hz) < 0.28
0.28 < fp (Hz) < 0.32
TOO FEW CASES

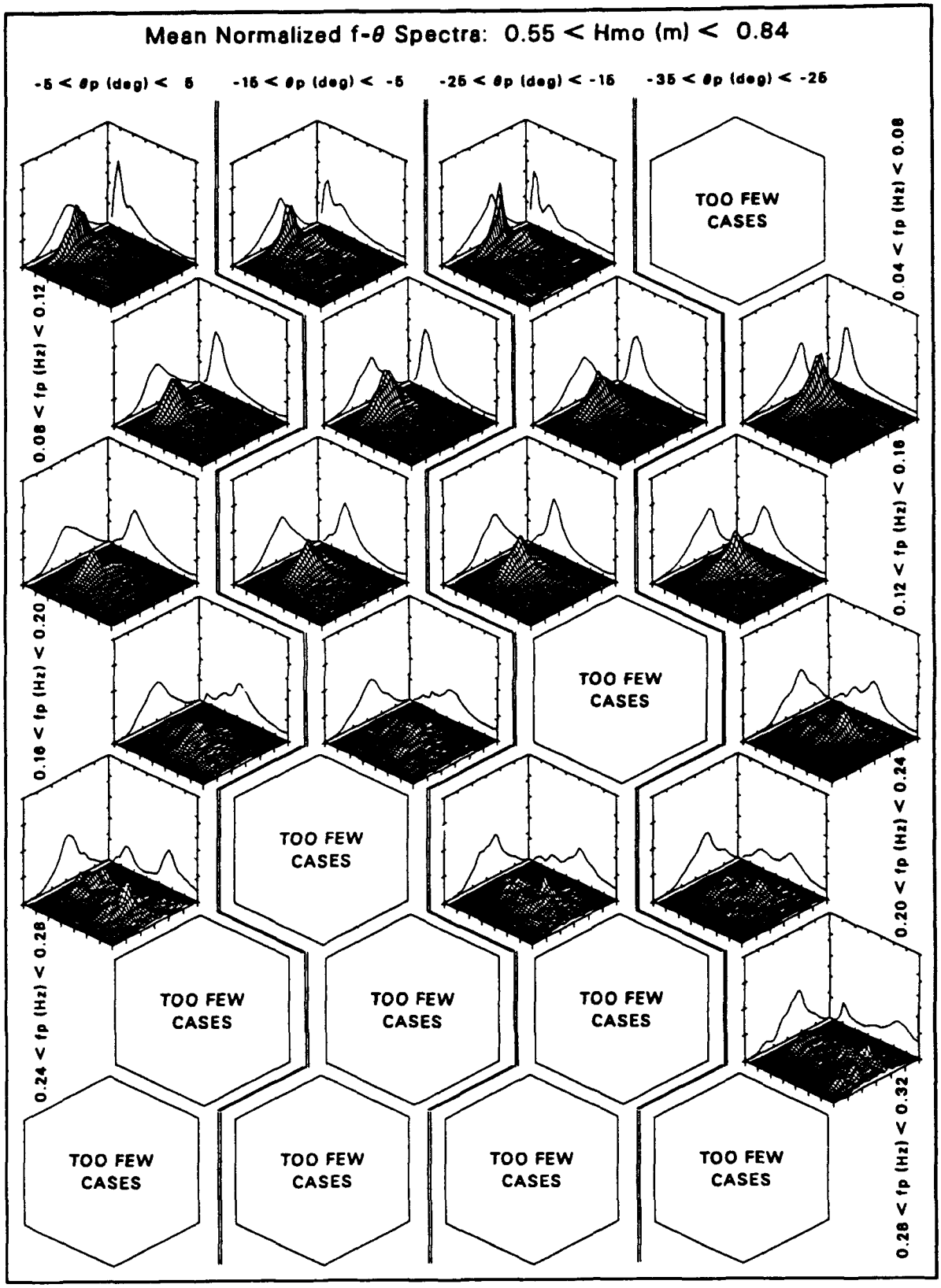
Mean Normalized f-θ Spectra: 0.55 < Hmo (m) < 0.84
-5 < θp (deg) < 5
-15 < θp (deg) < -5
-25 < θp (deg) < -15
-35 < θp (deg) < -25
0.04 < fp (Hz) < 0.08
0.08 < fp (Hz) < 0.12
0.12 < fp (Hz) < 0.16
0.16 < fp (Hz) < 0.20
0.20 < fp (Hz) < 0.24
0.24 < fp (Hz) < 0.28
0.28 < fp (Hz) < 0.32
TOO FEW CASES

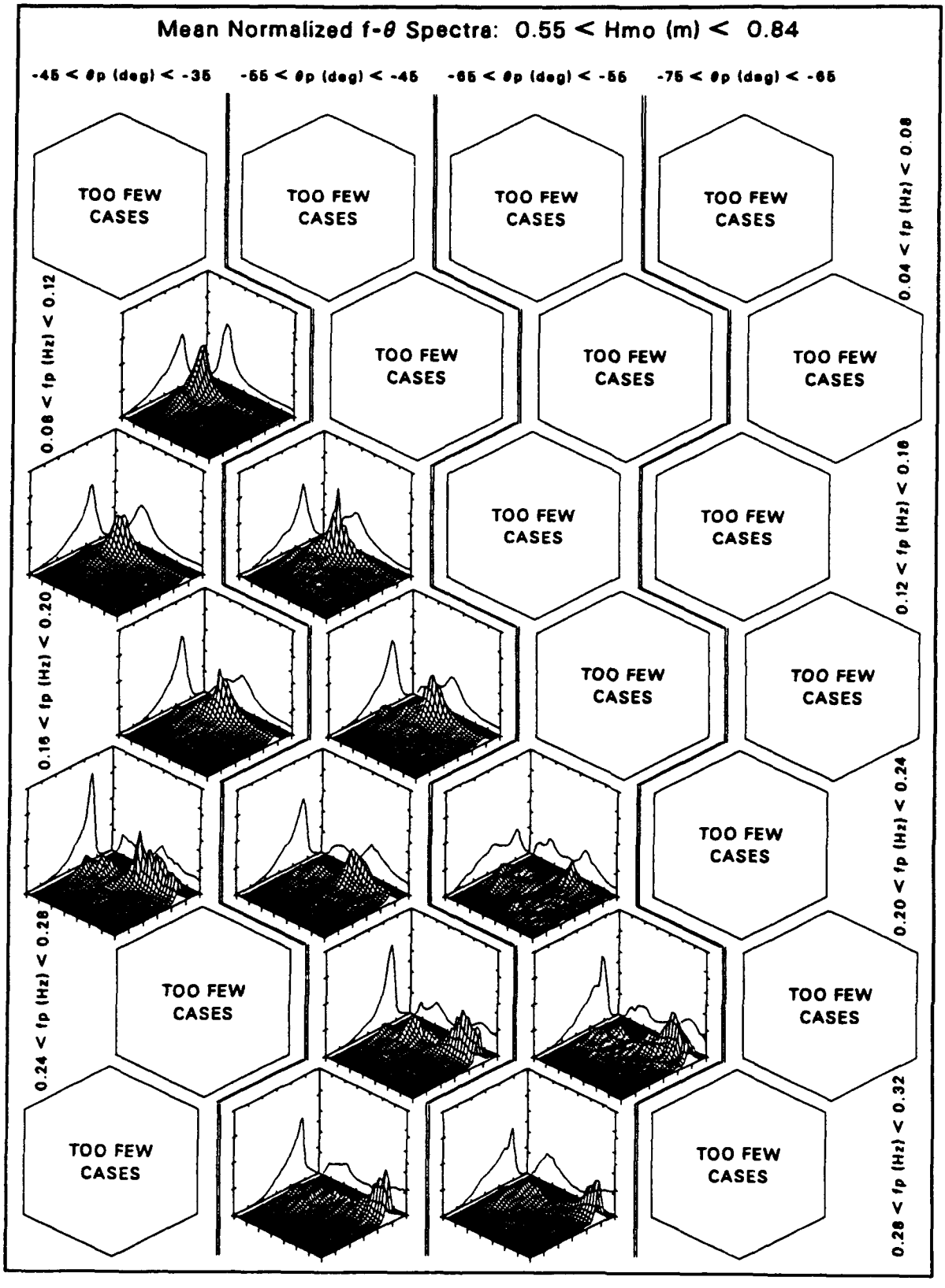
Mean Normalized f-θ Spectra: 0.55 < Hmo (m) < 0.84
-45 < θp (deg) < -35
-55 < θp (deg) < -45
-65 < θp (deg) < -55
-75 < θp (deg) < -65
0.04 < fp (Hz) < 0.08
0.08 < fp (Hz) < 0.12
0.12 < fp (Hz) < 0.16
0.16 < fp (Hz) < 0.20
0.20 < fp (Hz) < 0.24
0.24 < fp (Hz) < 0.28
0.28 < fp (Hz) < 0.32
TOO FEW CASES

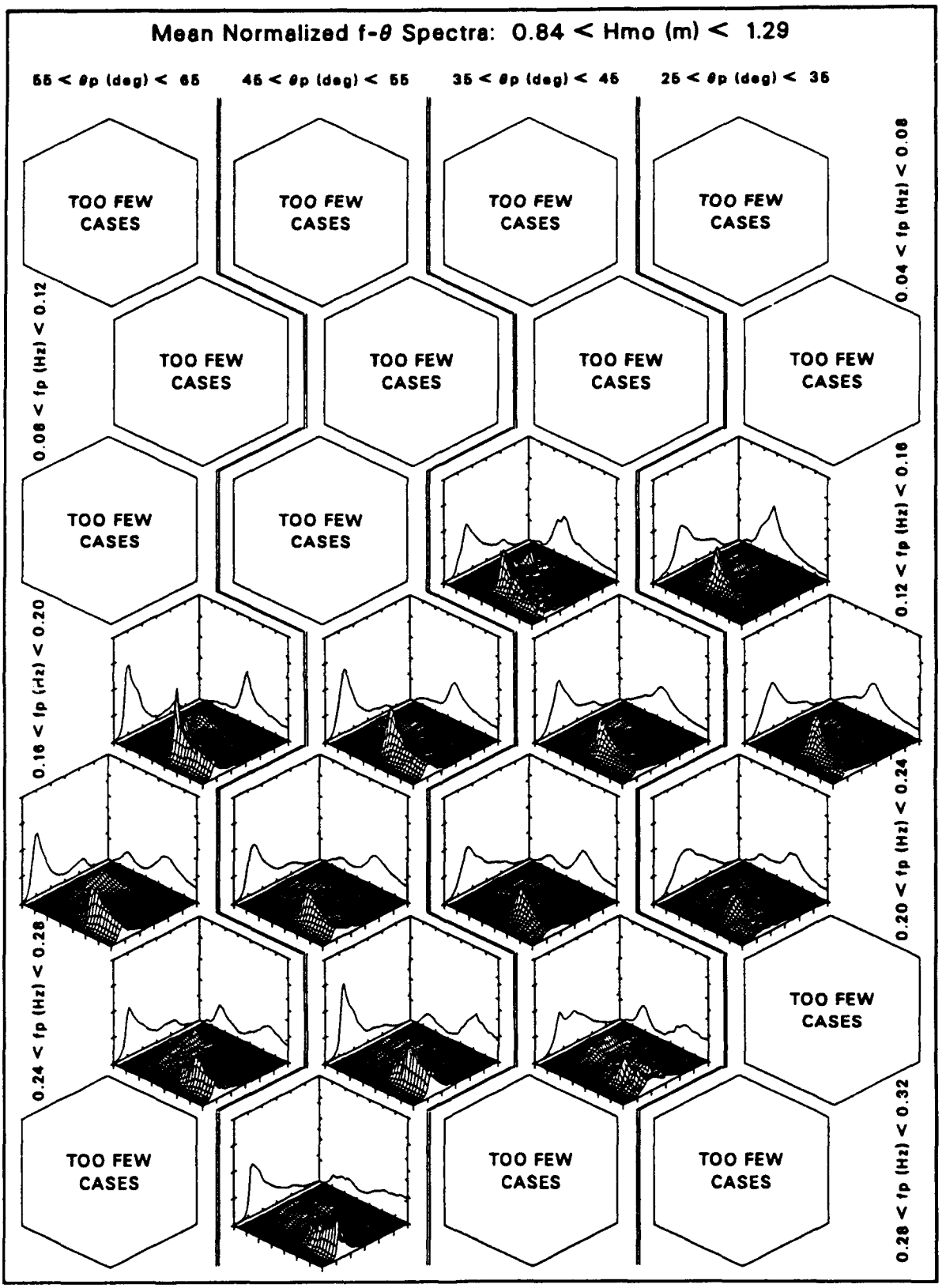
Mean Normalized f-θ Spectra: 0.84 < Hmo (m) < 1.29
55 < θp (deg) < 65
45 < θp (deg) < 55
35 < θp (deg) < 45
25 < θp (deg) < 35
0.04 < fp (Hz) < 0.08
0.08 < fp (Hz) < 0.12
0.12 < fp (Hz) < 0.16
0.16 < fp (Hz) < 0.20
0.20 < fp (Hz) < 0.24
0.24 < fp (Hz) < 0.28
0.28 < fp (Hz) < 0.32
TOO FEW CASES

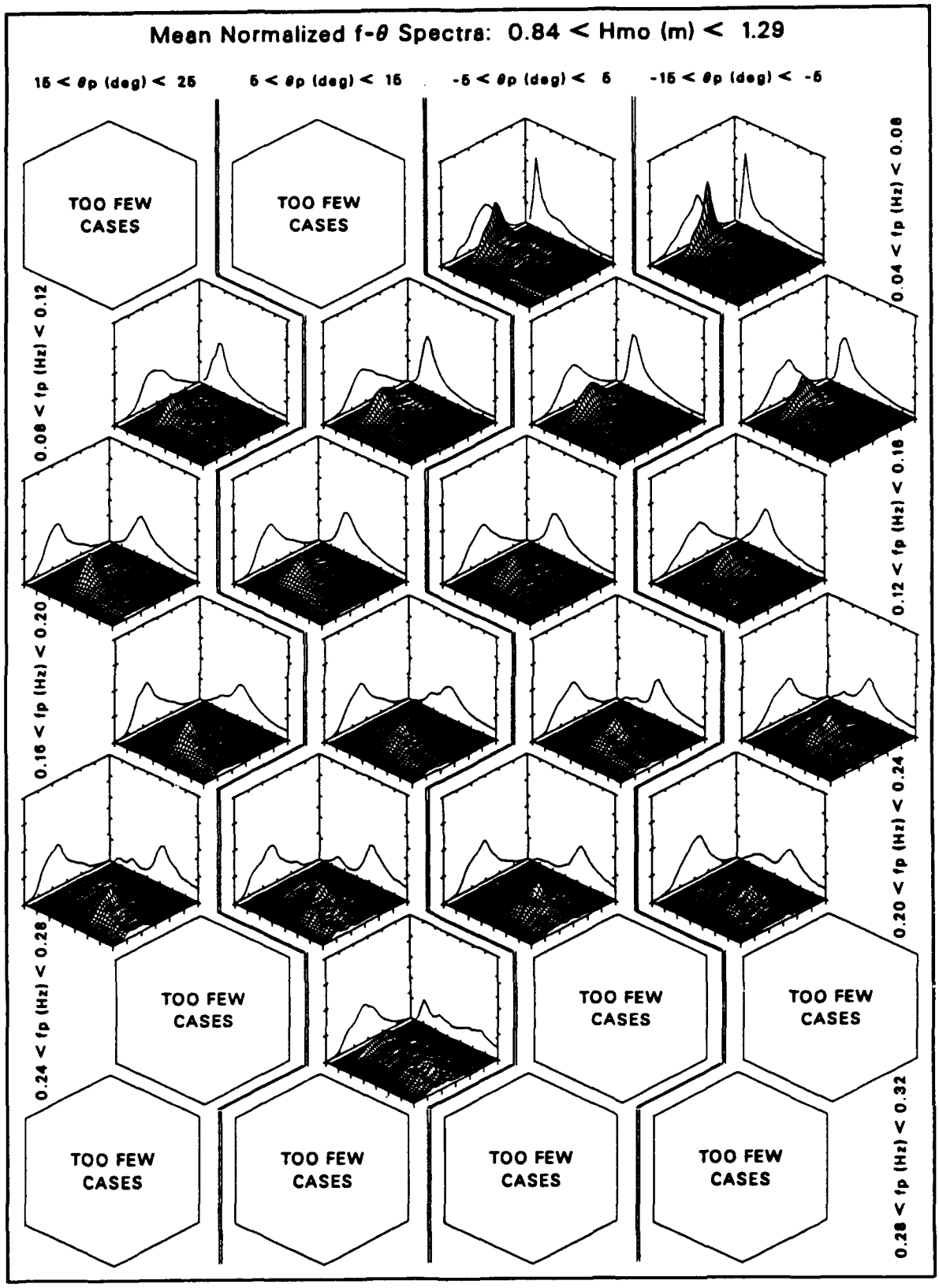
Mean Normalized f-θ Spectra: 0.84 < Hmo (m) < 1.29
15 < θp (deg) < 25
5 < θp (deg) < 15
-5 < θp (deg) < 5
-15 < θp (deg) < -5
0.04 < fp (Hz) < 0.08
0.08 < fp (Hz) < 0.12
0.12 < fp (Hz) < 0.16
0.16 < fp (Hz) < 0.20
0.20 < fp (Hz) < 0.24
0.24 < fp (Hz) < 0.28
0.28 < fp (Hz) < 0.32
TOO FEW CASES

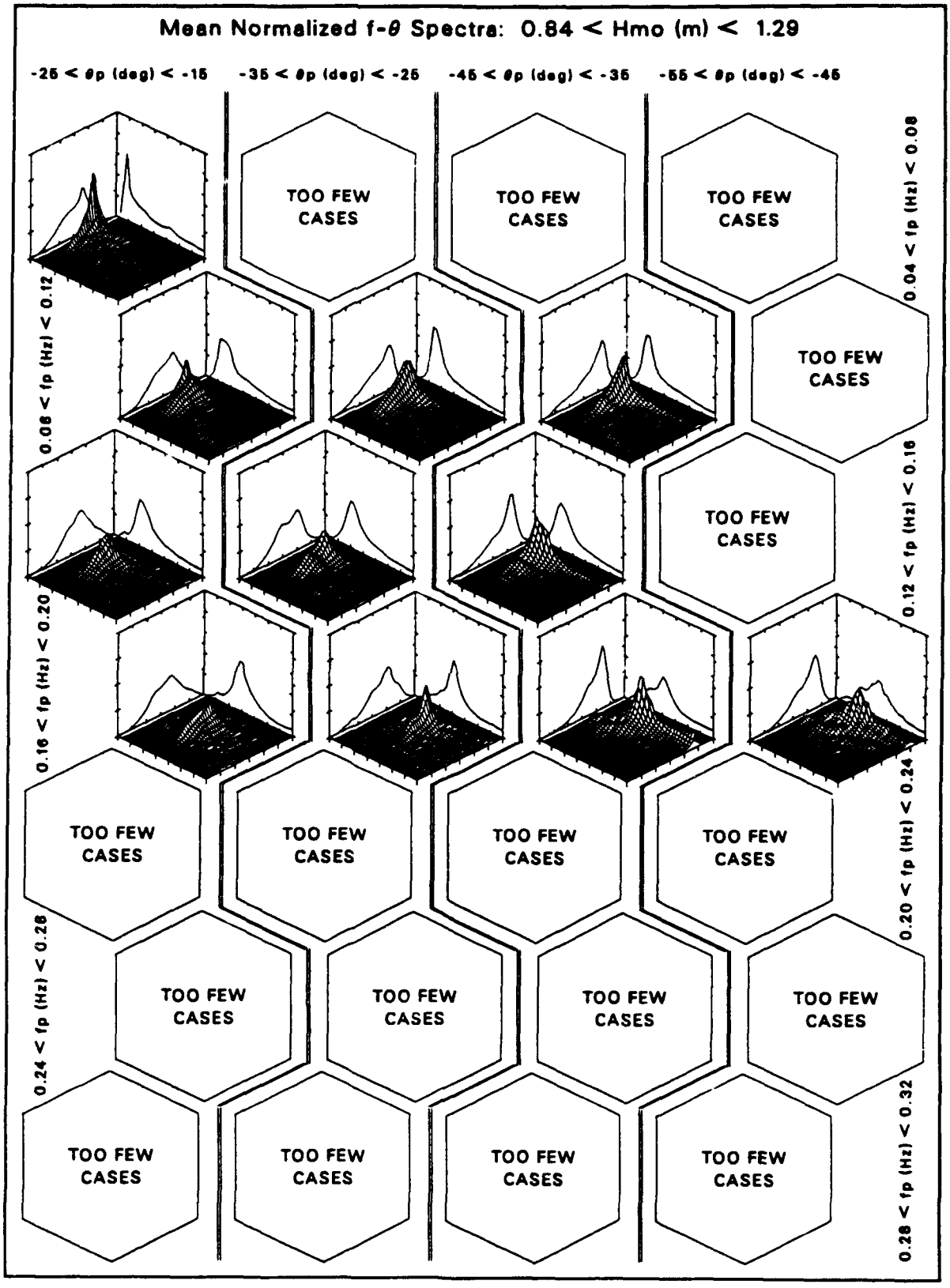
Mean Normalized f-θ Spectra: 0.84 < Hmo (m) < 1.29
-25 < θp (deg) < -15
-35 < θp (deg) < -25
-45 < θp (deg) < -35
-55 < θp (deg) < -45
0.04 < fp (Hz) < 0.08
0.08 < fp (Hz) < 0.12
0.12 < fp (Hz) < 0.16
0.16 < fp (Hz) < 0.20
0.20 < fp (Hz) < 0.24
0.24 < fp (Hz) < 0.28
0.28 < fp (Hz) < 0.32
TOO FEW CASES

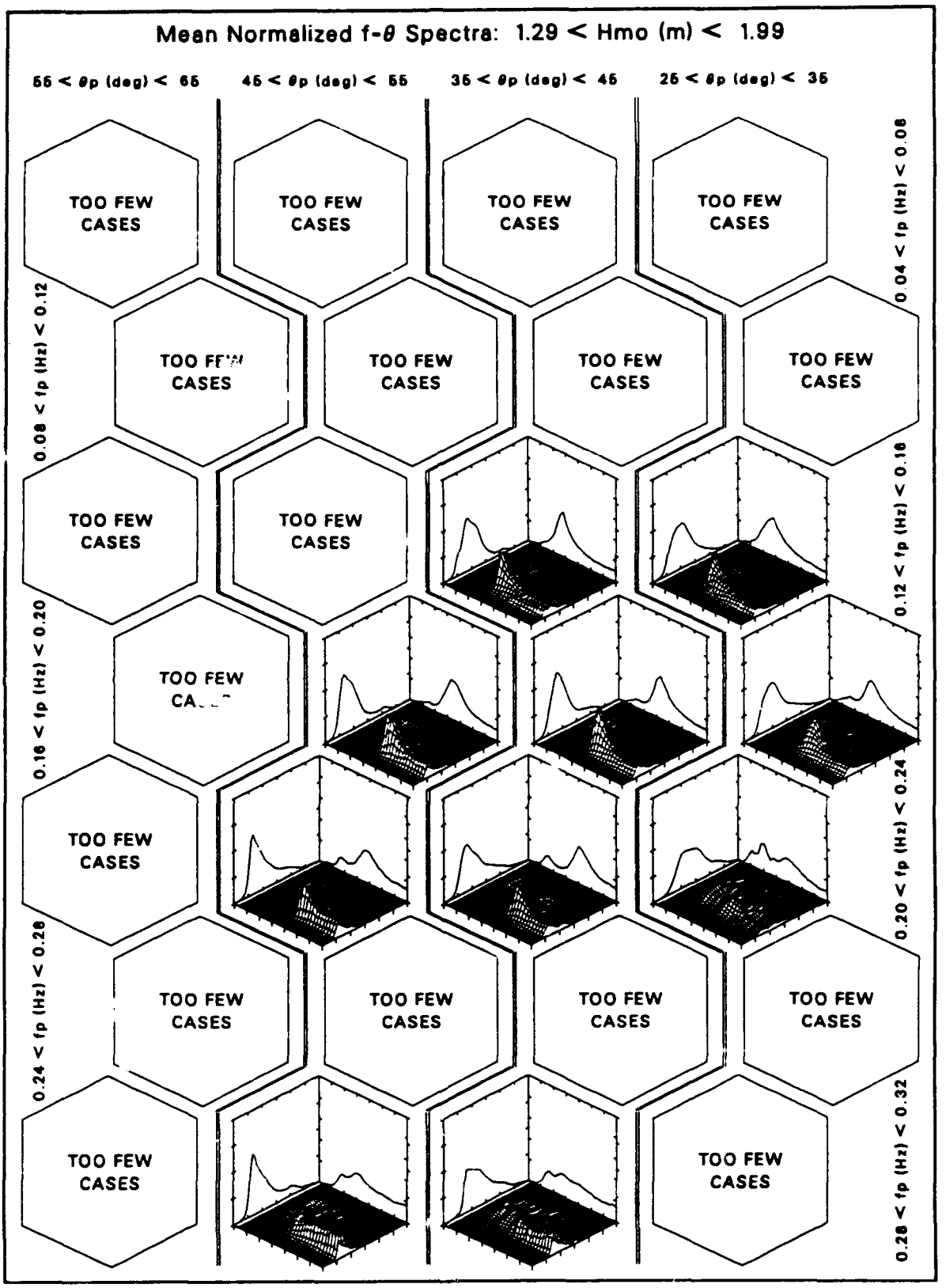
Mean Normalized f-θ Spectra: 1.29 < Hmo (m) < 1.99
55 < θp (deg) < 65
45 < θp (deg) < 55
35 < θp (deg) < 45
25 < θp (deg) < 35
0.04 < fp (Hz) < 0.08
0.08 < fp (Hz) < 0.12
0.12 < fp (Hz) < 0.16
0.16 < fp (Hz) < 0.20
0.20 < fp (Hz) < 0.24
0.24 < fp (Hz) < 0.28
0.28 < fp (Hz) < 0.32
TOO FEW CASES

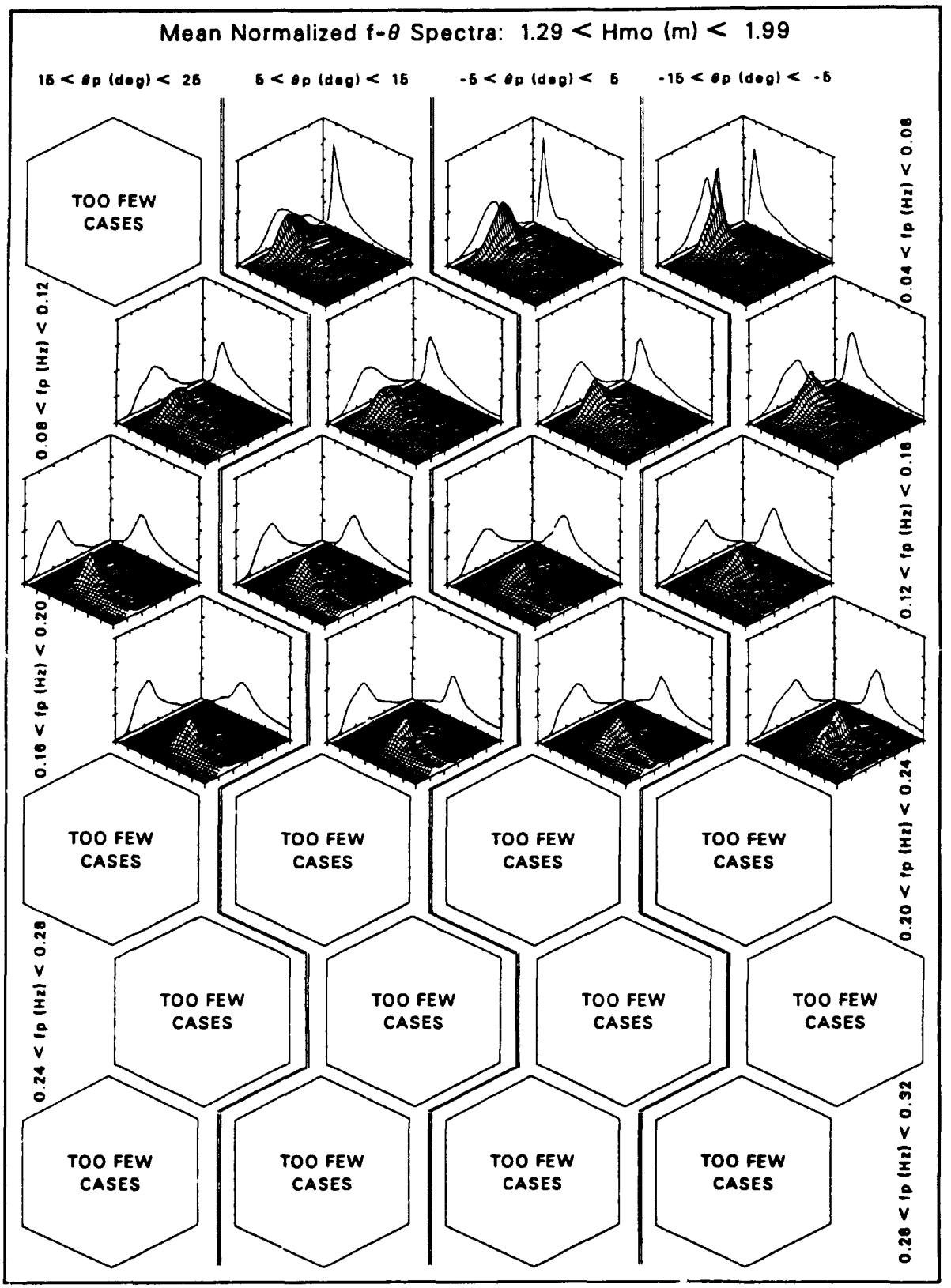
Mean Normalized f-θ Spectra: 1.29 < Hmo (m) < 1.99
15 < θp (deg) < 25
5 < θp (deg) < 15
-5 < θp (deg) < 5
-15 < θp (deg) < -5
0.04 < fp (Hz) < 0.08
0.08 < fp (Hz) < 0.12
0.12 < fp (Hz) < 0.16
0.16 < fp (Hz) < 0.20
0.20 < fp (Hz) < 0.24
0.24 < fp (Hz) < 0.28
0.28 < fp (Hz) < 0.32
TOO FEW CASES

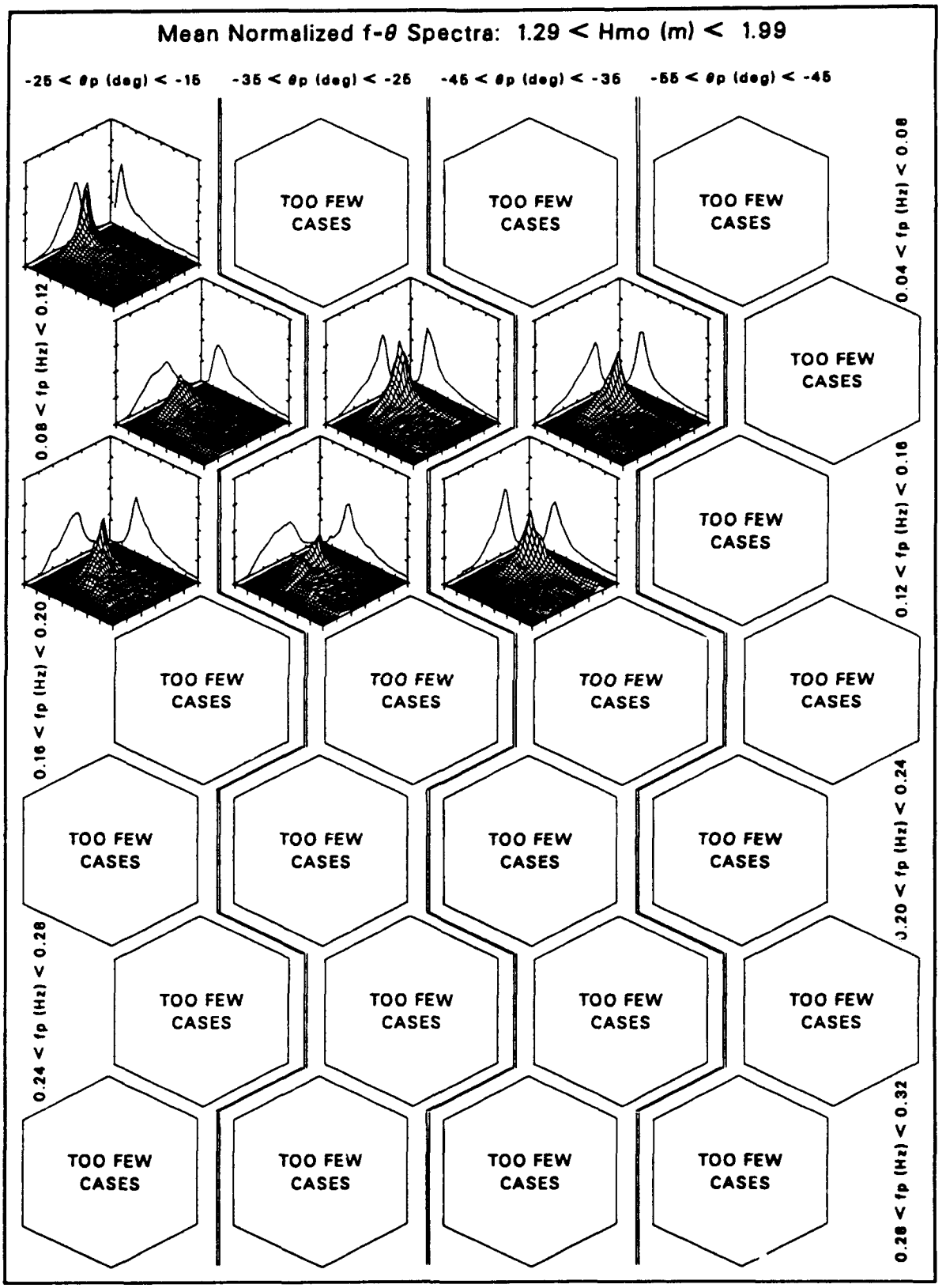
Mean Normalized f-θ Spectra: 1.29 < Hmo (m) < 1.99
-25 < θp (deg) < -15
-35 < θp (deg) < -25
-45 < θp (deg) < -35
-55 < θp (deg) < -45
0.08 < fp (Hz) < 0.12
0.04 < fp (Hz) < 0.08
0.12 < fp (Hz) < 0.16
0.16 < fp (Hz) < 0.20
0.20 < fp (Hz) < 0.24
0.24 < fp (Hz) < 0.28
0.28 < fp (Hz) < 0.32
TOO FEW CASES

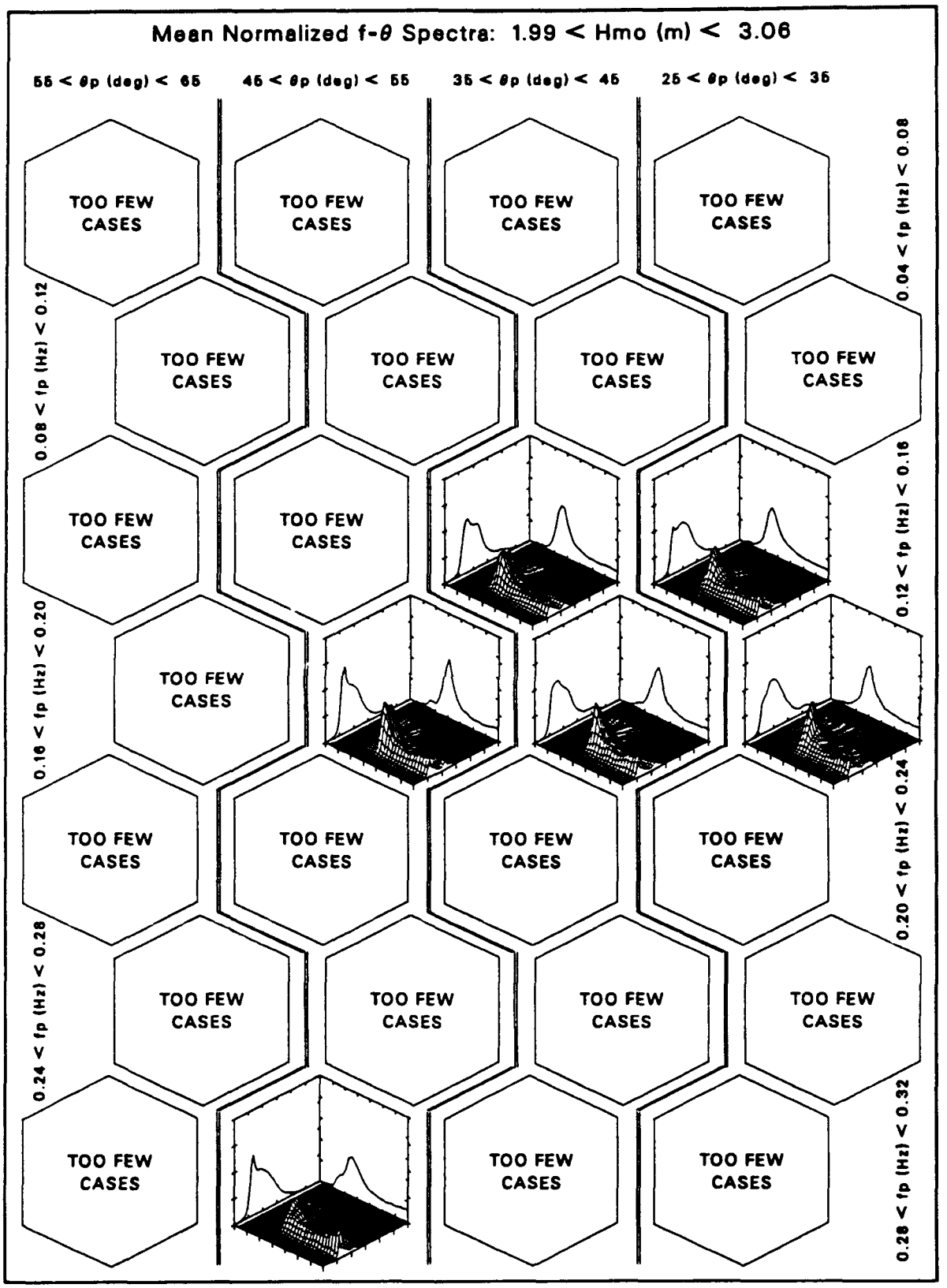
Mean Normalized f-θ Spectra: 1.99 < Hmo (m) < 3.06
55 < θp (deg) < 65
45 < θp (deg) < 55
35 < θp (deg) < 45
25 < θp (deg) < 35
0.04 < fp (Hz) < 0.08
0.08 < fp (Hz) < 0.12
0.12 < fp (Hz) < 0.16
0.16 < fp (Hz) < 0.20
0.20 < fp (Hz) < 0.24
0.24 < fp (Hz) < 0.28
0.28 < fp (Hz) < 0.32
TOO FEW CASES

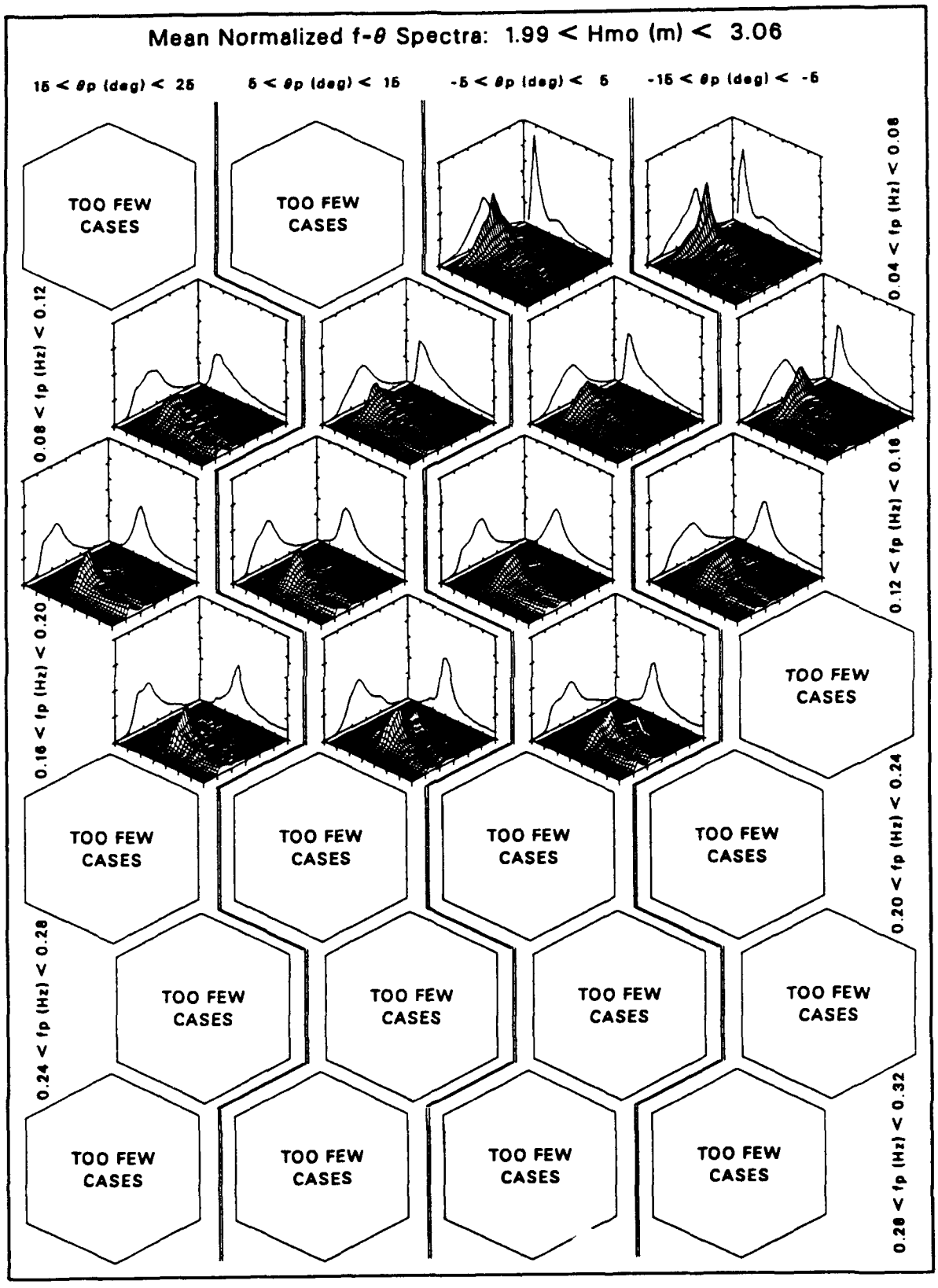
Mean Normalized f-θ Spectra: 1.99 < Hmo (m) < 3.06
15 < θp (deg) < 25
5 < θp (deg) < 15
-5 < θp (deg) < 5
-15 < θp (deg) < -5
0.04 < fp (Hz) < 0.08
0.08 < fp (Hz) < 0.12
0.12 < fp (Hz) < 0.16
0.16 < fp (Hz) < 0.20
0.20 < fp (Hz) < 0.24
0.24 < fp (Hz) < 0.28
0.28 < fp (Hz) < 0.32
TOO FEW CASES

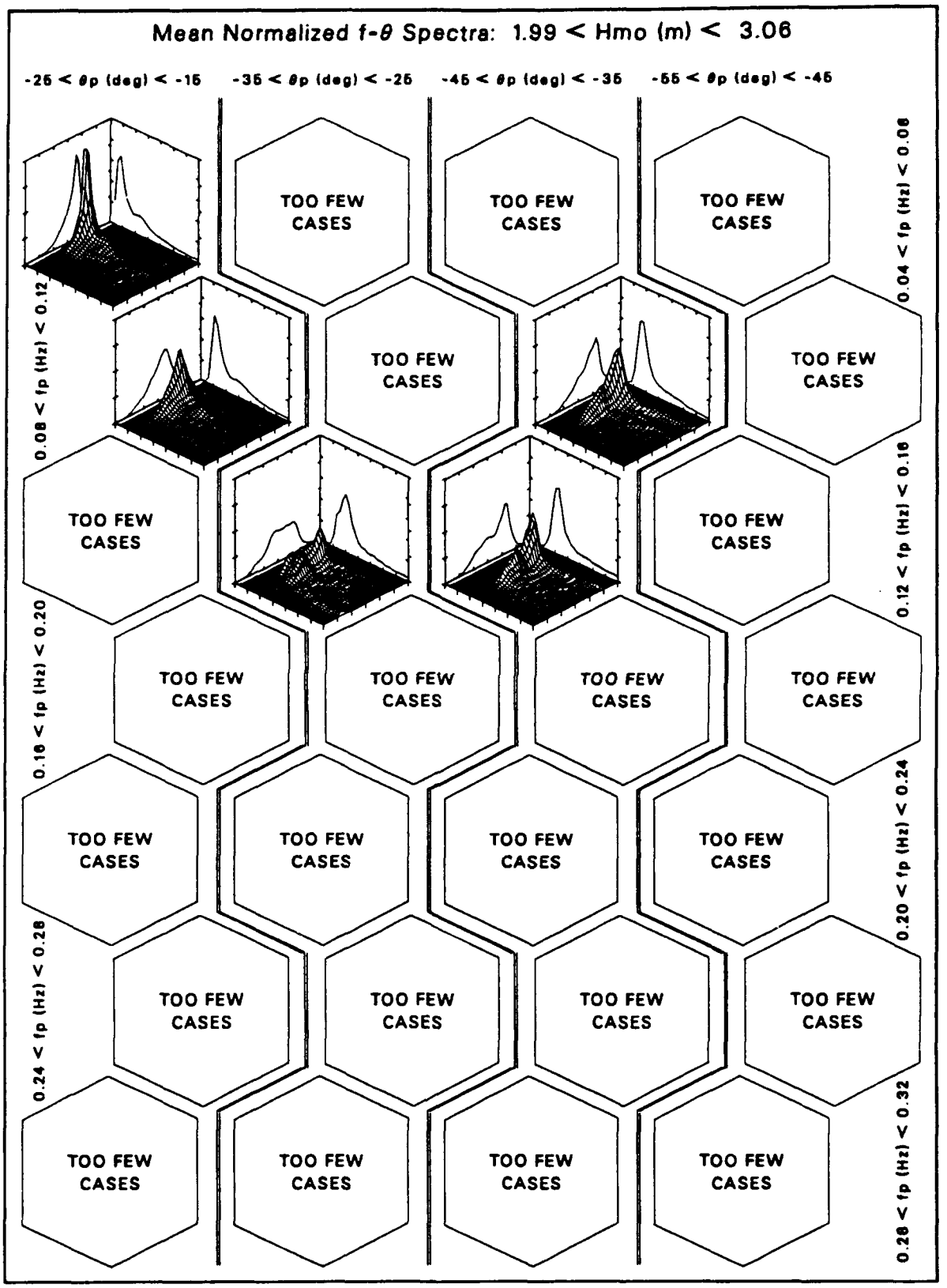
Mean Normalized f-θ Spectra: 1.99 < Hmo (m) < 3.06
-25 < θp (deg) < -15
-35 < θp (deg) < -25
-45 < θp (deg) < -35
-55 < θp (deg) < -45
0.04 < fp (Hz) < 0.08
0.08 < fp (Hz) < 0.12
0.12 < fp (Hz) < 0.16
0.16 < fp (Hz) < 0.20
0.20 < fp (Hz) < 0.24
0.24 < fp (Hz) < 0.28
0.28 < fp (Hz) < 0.32
TOO FEW CASES

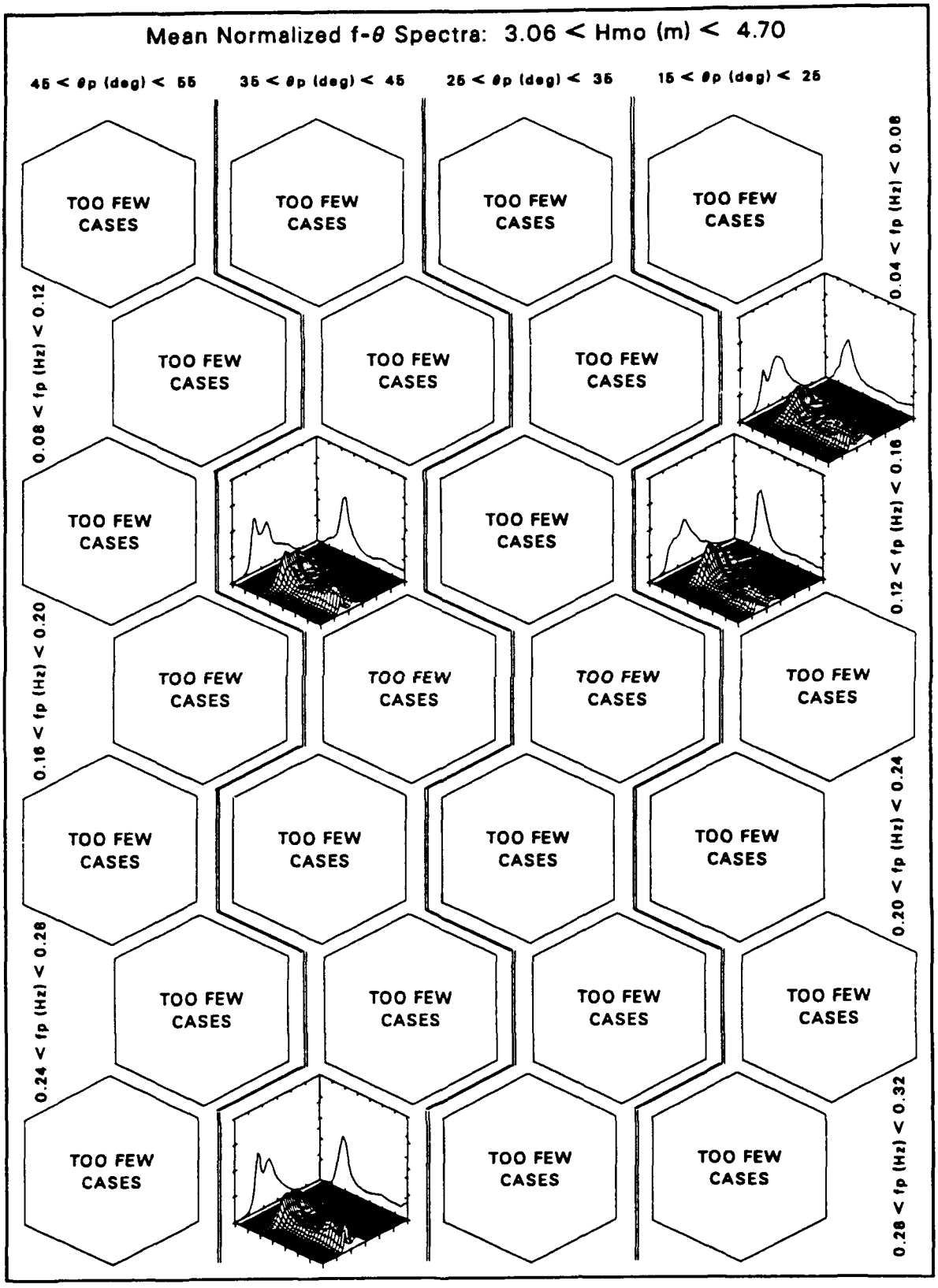
Mean Normalized f-θ Spectra: 3.06 < Hmo (m) < 4.70
45 < θp (deg) < 55
35 < θp (deg) < 45
25 < θp (deg) < 35
15 < θp (deg) < 25
0.04 < fp (Hz) < 0.08
0.08 < fp (Hz) < 0.12
0.12 < fp (Hz) < 0.16
0.16 < fp (Hz) < 0.20
0.20 < fp (Hz) < 0.24
0.24 < fp (Hz) < 0.28
0.28 < fp (Hz) < 0.32
TOO FEW CASES

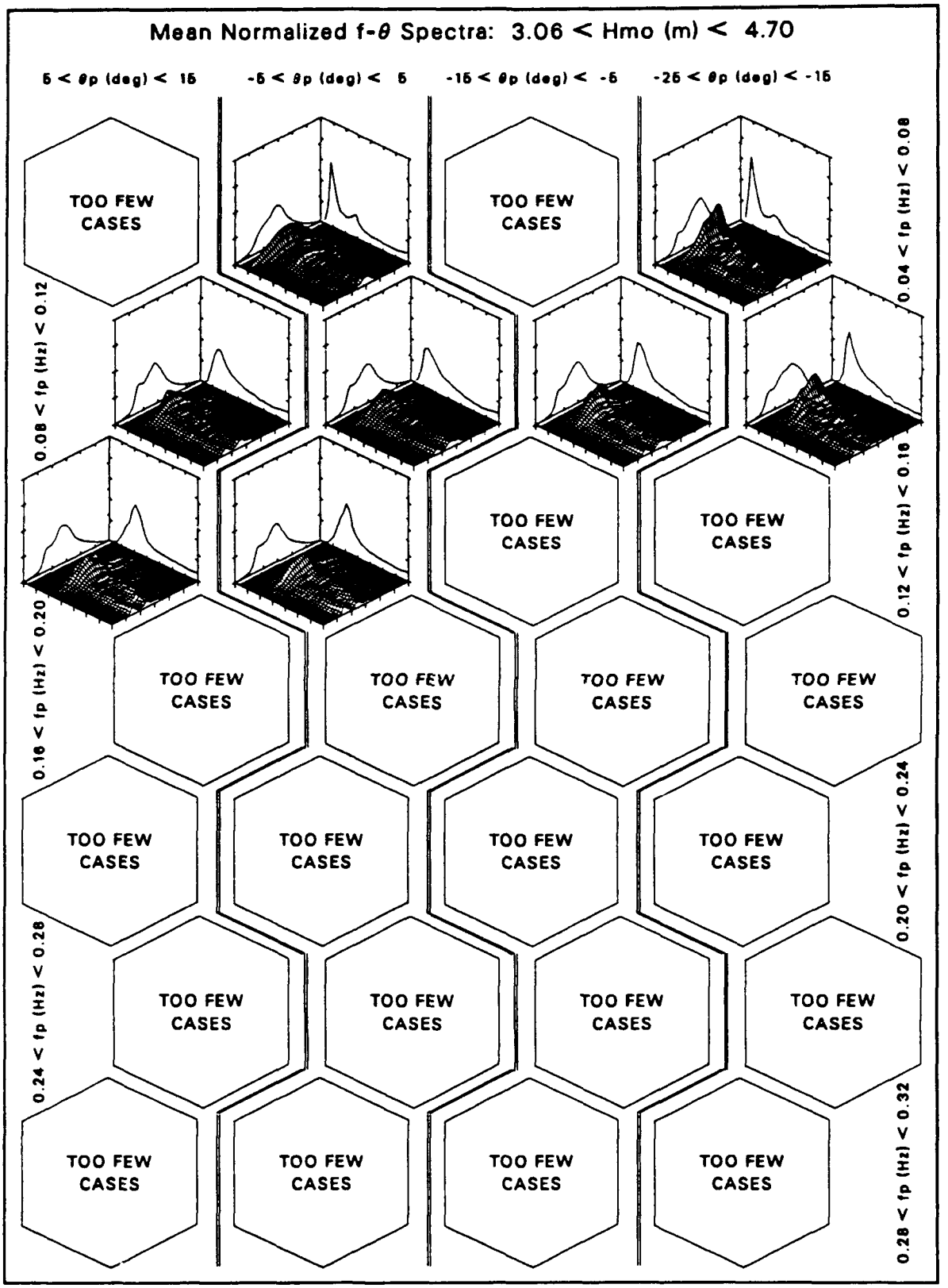
Mean Normalized f-θ Spectra: 3.06 < Hmo (m) < 4.70
5 < θp (deg) < 15
-5 < θp (deg) < 5
-15 < θp (deg) < -5
-25 < θp (deg) < -15
0.04 < fp (Hz) < 0.08
0.08 < fp (Hz) < 0.12
0.12 < fp (Hz) < 0.16
0.16 < fp (Hz) < 0.20
0.20 < fp (Hz) < 0.24
0.24 < fp (Hz) < 0.28
0.28 < fp (Hz) < 0.32
TOO FEW CASES

Appendix B
Plots of Deviation Spectra

This appendix contains illustrations of normalized standard deviation spectra $S'_{\sigma}(f_n,\theta_m)$ defined by Equation 8 in Chapter 3 for all (H_{mo},f_p,θ_p) parametric classes for which data are available. Plots are grouped such that two or more consecutive pages represent a single wave height class. Each page contains four direction classes within its wave height class, and all frequency classes corresponding to the height and direction classes. Spaces for classes with too few cases to average are included to preserve the matrix form of this display. To save space, plot axes are not labelled. However, all spectra are plotted to the same scale, and axis scales are as shown in Figure B1, which can be used as a template for axis notation.

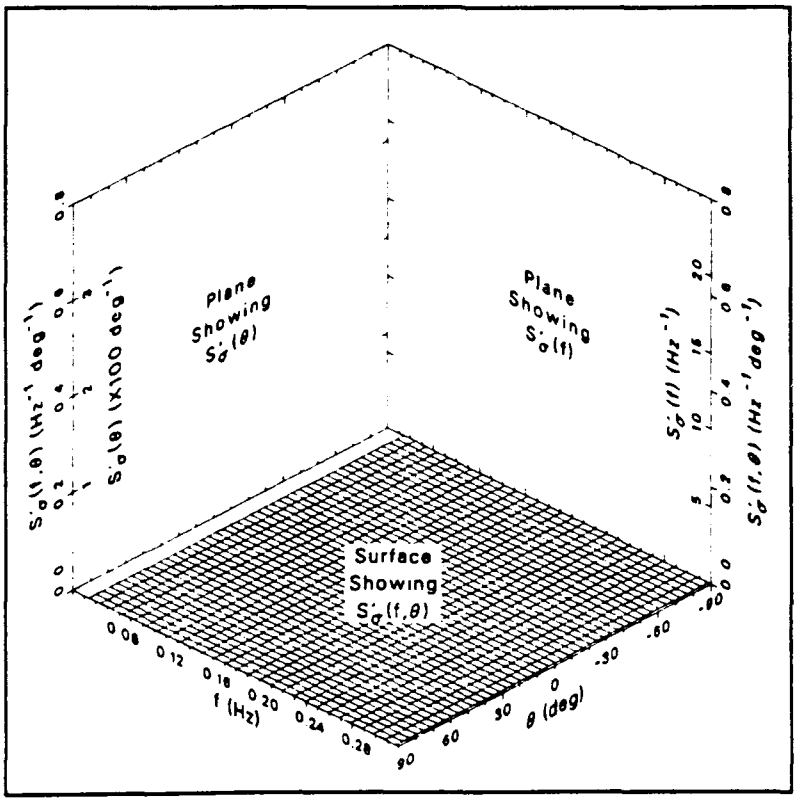

Figure B1. Axis label template

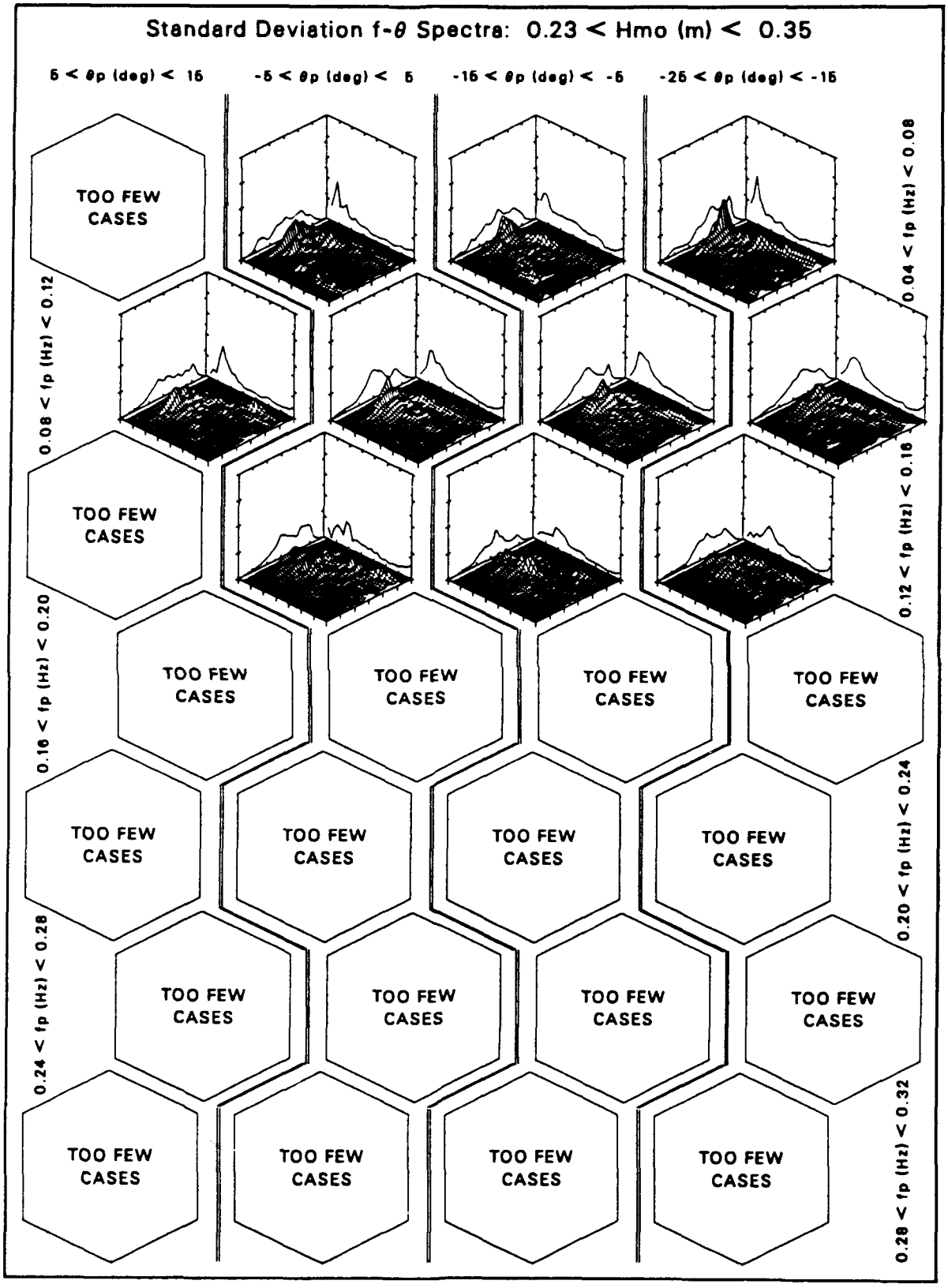
Standard Deviation f-θ Spectra: 0.23 < Hmo (m) < 0.35
5 < θp (deg) < 15
-5 < θp (deg) < 5
-15 < θp (deg) < -5
-25 < θp (deg) < -15
0.04 < fp (Hz) < 0.08
0.08 < fp (Hz) < 0.12
0.12 < fp (Hz) < 0.16
0.16 < fp (Hz) < 0.20
0.20 < fp (Hz) < 0.24
0.24 < fp (Hz) < 0.28
0.28 < fp (Hz) < 0.32
TOO FEW CASES

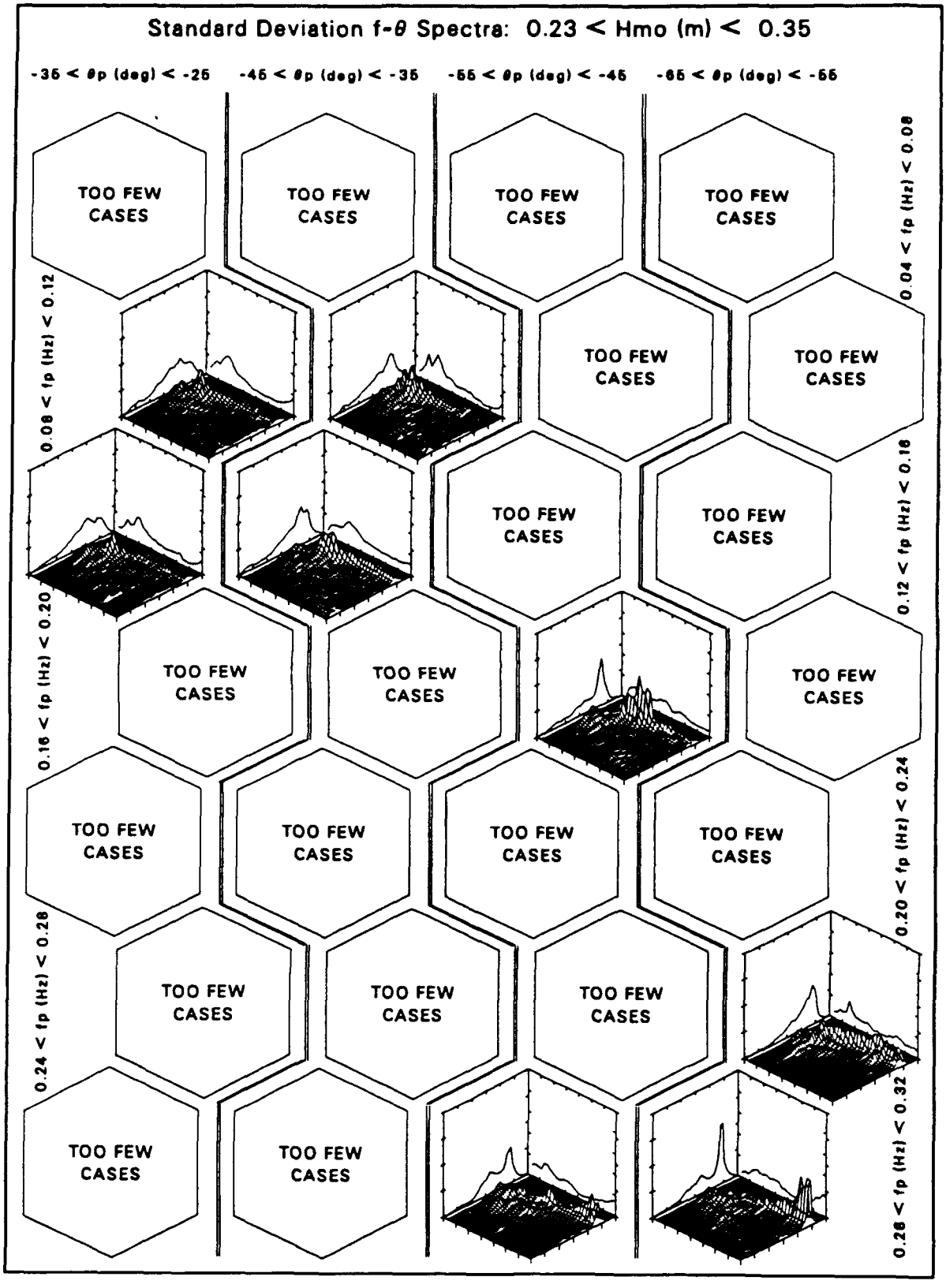
Standard Deviation f-θ Spectra: 0.23 < Hmo (m) < 0.35
-35 < θp (deg) < -25
-45 < θp (deg) < -35
-55 < θp (deg) < -45
-65 < θp (deg) < -55
0.04 < fp (Hz) < 0.08
0.08 < fp (Hz) < 0.12
0.12 < fp (Hz) < 0.16
0.16 < fp (Hz) < 0.20
0.20 < fp (Hz) < 0.24
0.24 < fp (Hz) < 0.28
0.28 < fp (Hz) < 0.32
TOO FEW CASES

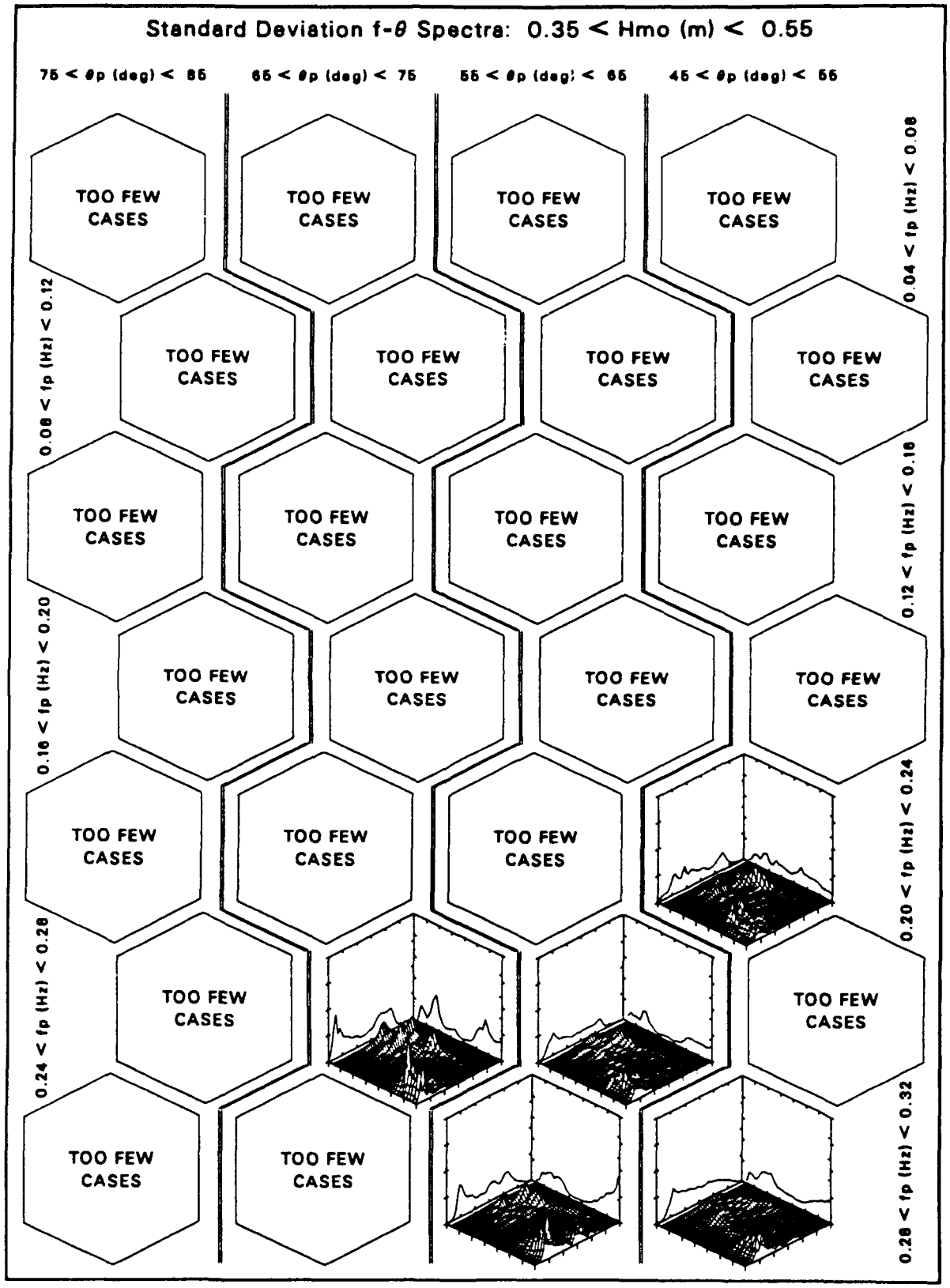
Standard Deviation f-θ Spectra: 0.35 < Hmo (m) < 0.55
75 < θp (deg) < 85
65 < θp (deg) < 75
55 < θp (deg) < 65
45 < θp (deg) < 55
0.04 < fp (Hz) < 0.08
0.08 < fp (Hz) < 0.12
0.12 < fp (Hz) < 0.16
0.16 < fp (Hz) < 0.20
0.20 < fp (Hz) < 0.24
0.24 < fp (Hz) < 0.28
0.28 < fp (Hz) < 0.32
TOO FEW CASES

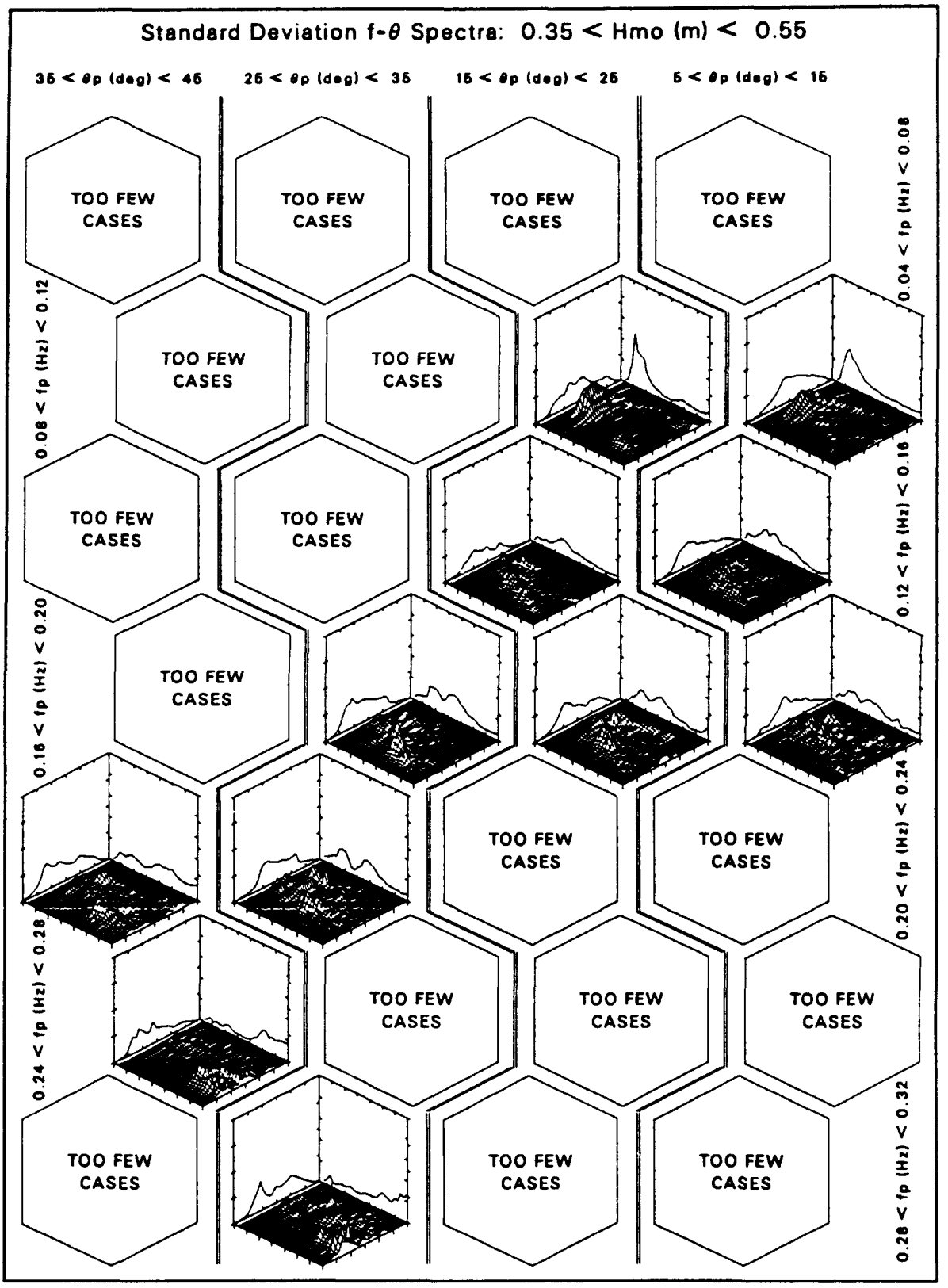
Standard Deviation f-θ Spectra: 0.35 < Hmo (m) < 0.55
35 < θp (deg) < 45
25 < θp (deg) < 35
15 < θp (deg) < 25
5 < θp (deg) < 15
0.04 < fp (Hz) < 0.08
0.08 < fp (Hz) < 0.12
0.12 < fp (Hz) < 0.16
0.16 < fp (Hz) < 0.20
0.20 < fp (Hz) < 0.24
0.24 < fp (Hz) < 0.28
0.28 < fp (Hz) < 0.32
TOO FEW CASES

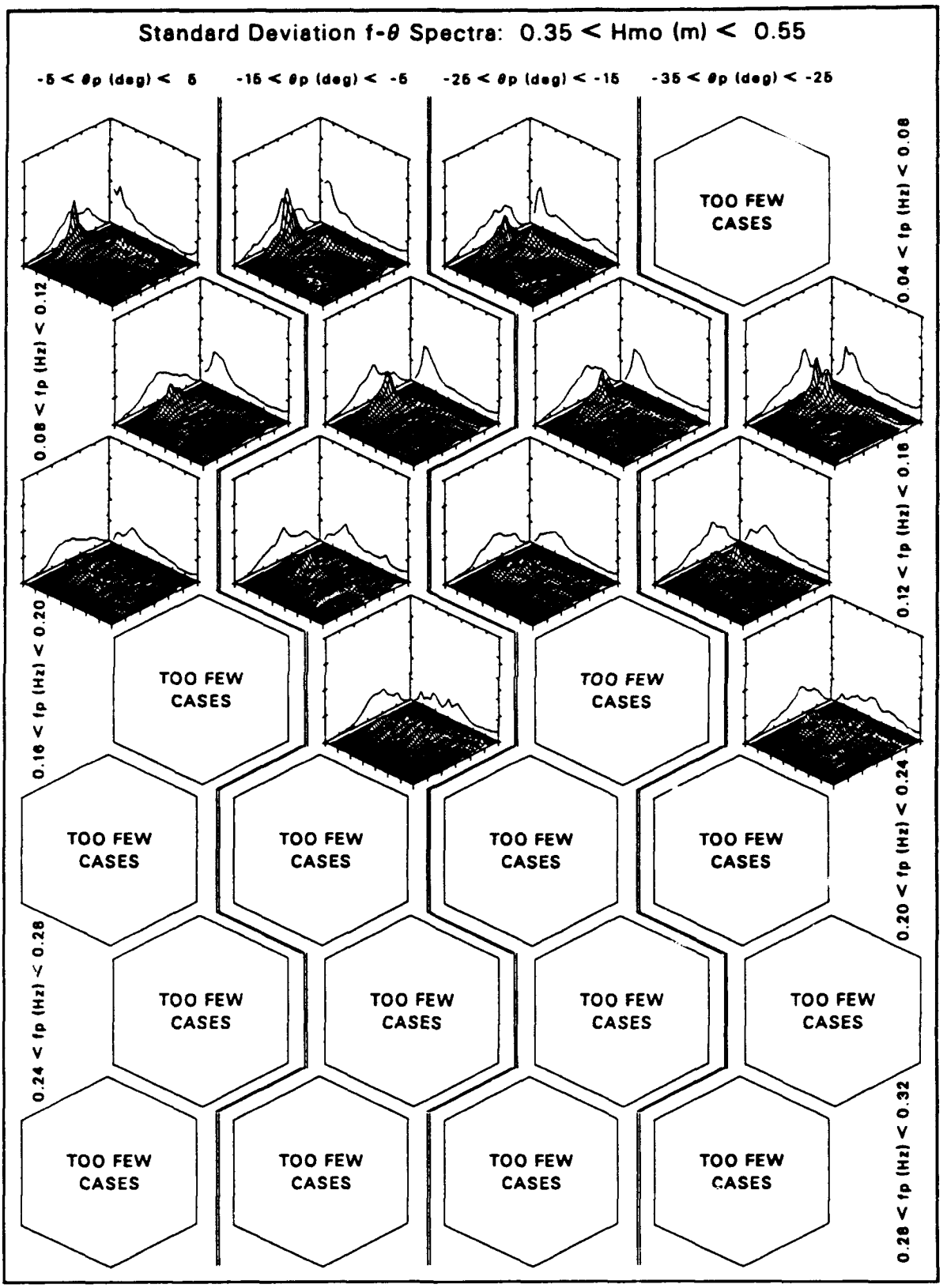
Standard Deviation f-θ Spectra: 0.35 < Hmo (m) < 0.55
-5 < θp (deg) < 5
-15 < θp (deg) < -5
-25 < θp (deg) < -15
-35 < θp (deg) < -25
0.04 < fp (Hz) < 0.08
0.08 < fp (Hz) < 0.12
0.12 < fp (Hz) < 0.16
0.16 < fp (Hz) < 0.20
0.20 < fp (Hz) < 0.24
0.24 < fp (Hz) < 0.28
0.28 < fp (Hz) < 0.32
TOO FEW CASES

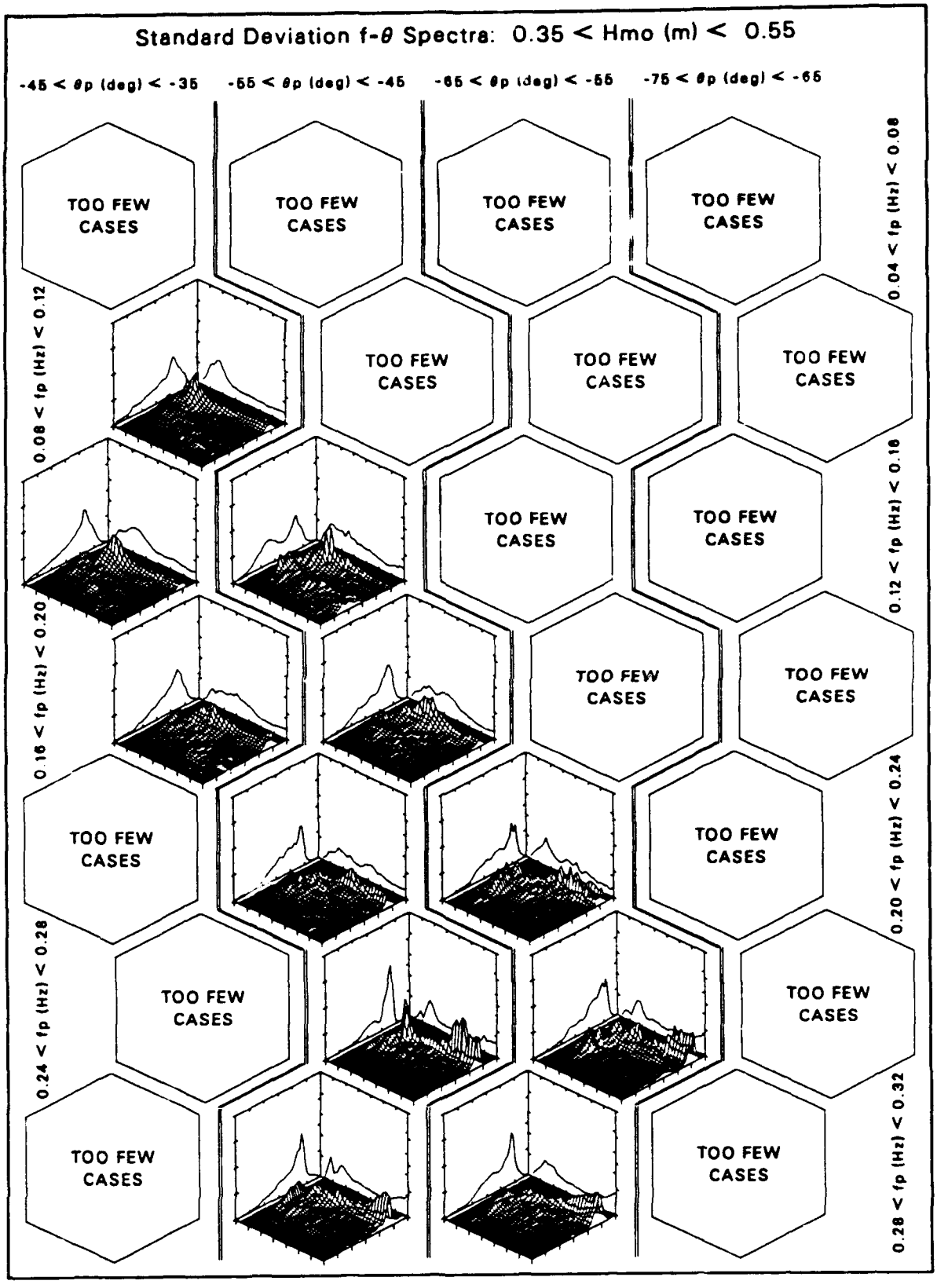
Standard Deviation f-θ Spectra: 0.35 < Hmo (m) < 0.55
-45 < θp (deg) < -35
-55 < θp (deg) < -45
-65 < θp (deg) < -55
-75 < θp (deg) < -65
0.04 < fp (Hz) < 0.08
0.08 < fp (Hz) < 0.12
0.12 < fp (Hz) < 0.16
0.16 < fp (Hz) < 0.20
0.20 < fp (Hz) < 0.24
0.24 < fp (Hz) < 0.28
0.28 < fp (Hz) < 0.32
TOO FEW CASES

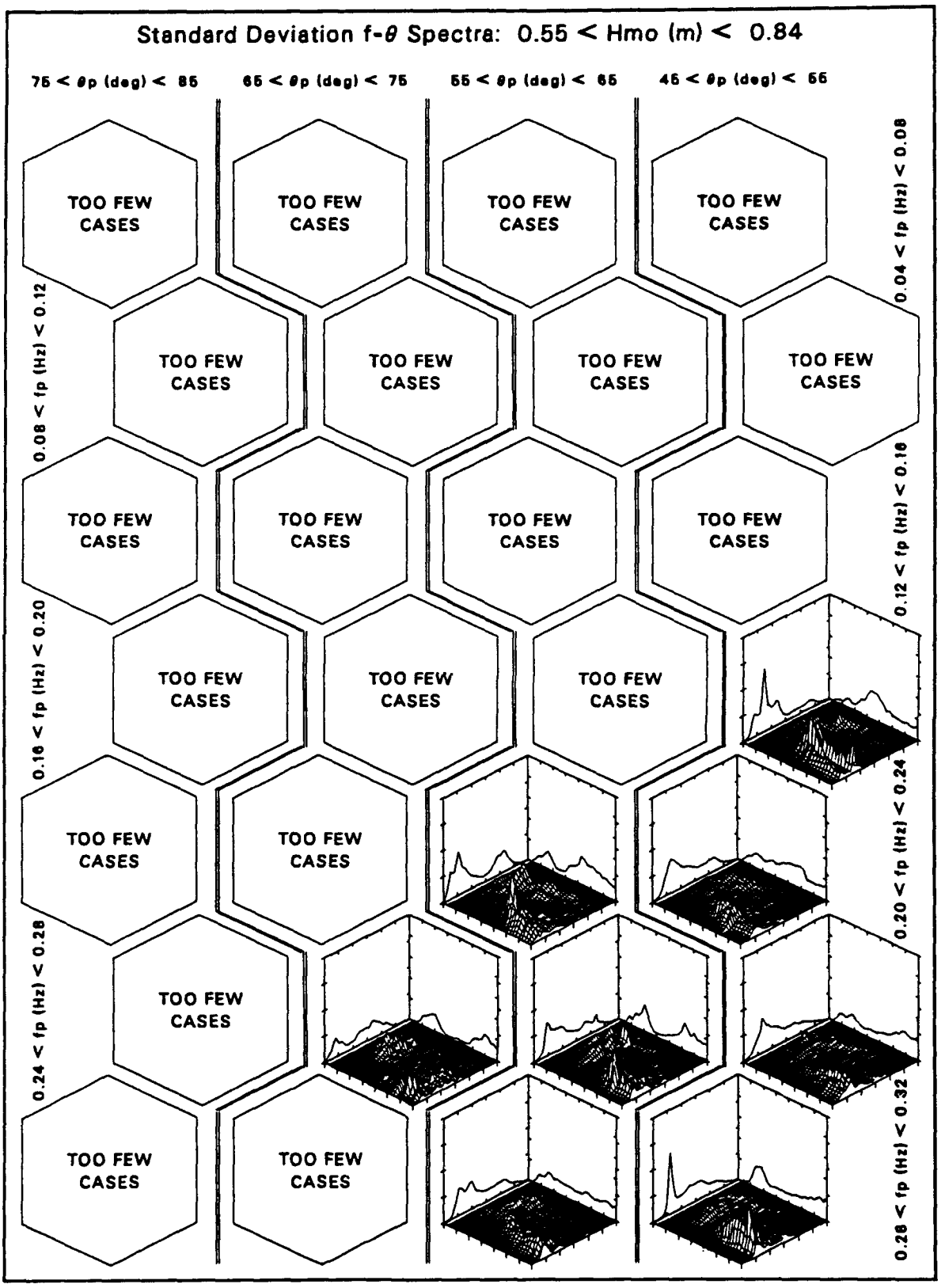
Standard Deviation f-θ Spectra: 0.55 < Hmo (m) < 0.84
75 < θp (deg) < 85
65 < θp (deg) < 75
55 < θp (deg) < 65
45 < θp (deg) < 55
0.04 < fp (Hz) < 0.08
0.08 < fp (Hz) < 0.12
0.12 < fp (Hz) < 0.16
0.16 < fp (Hz) < 0.20
0.20 < fp (Hz) < 0.24
0.24 < fp (Hz) < 0.28
0.28 < fp (Hz) < 0.32
TOO FEW CASES

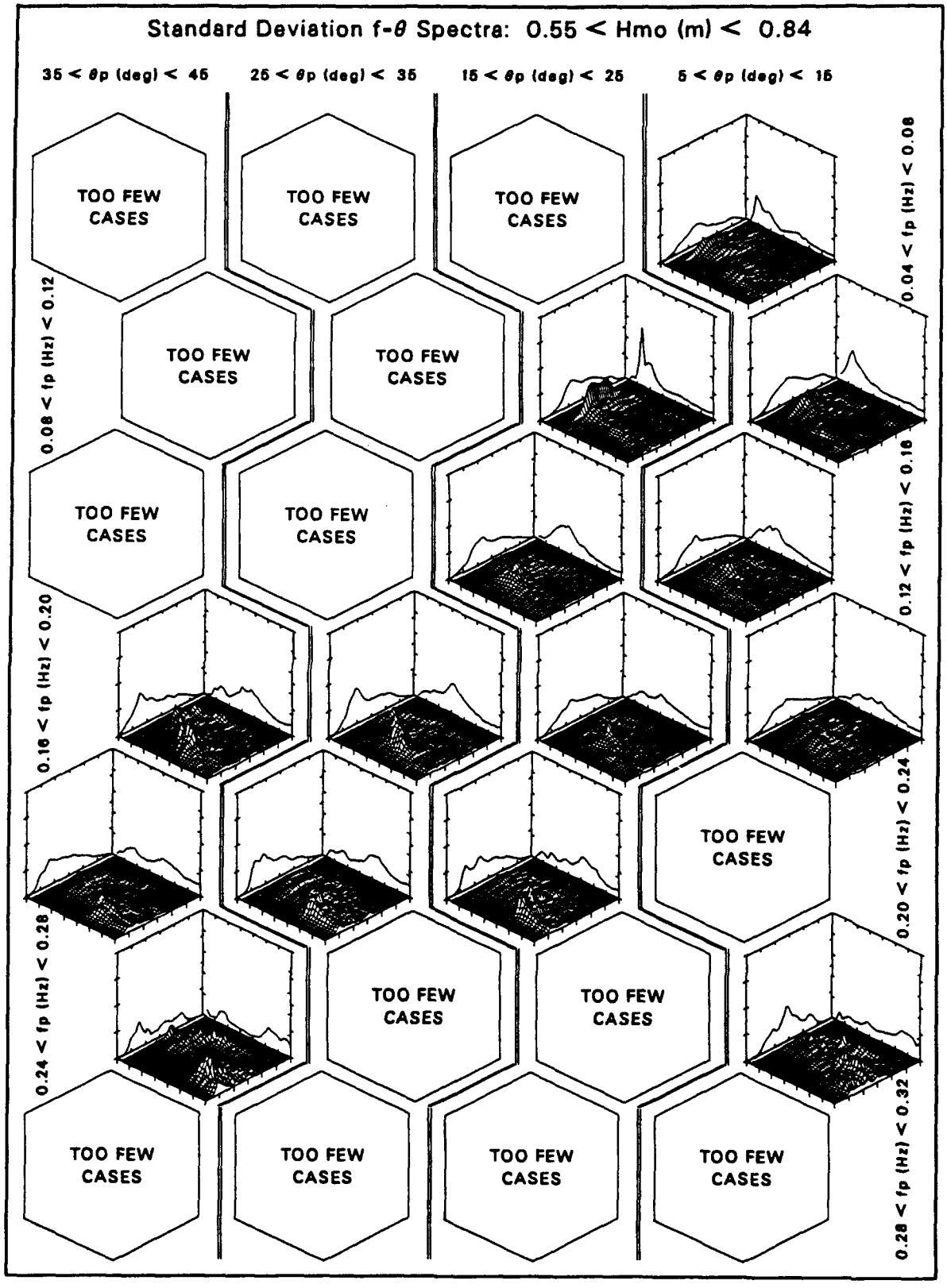
Standard Deviation f-θ Spectra: 0.55 < Hmo (m) < 0.84
35 < θp (deg) < 45
25 < θp (deg) < 35
15 < θp (deg) < 25
5 < θp (deg) < 15
0.04 < fp (Hz) < 0.08
0.08 < fp (Hz) < 0.12
0.12 < fp (Hz) < 0.16
0.16 < fp (Hz) < 0.20
0.20 < fp (Hz) < 0.24
0.24 < fp (Hz) < 0.28
0.28 < fp (Hz) < 0.32
TOO FEW CASES

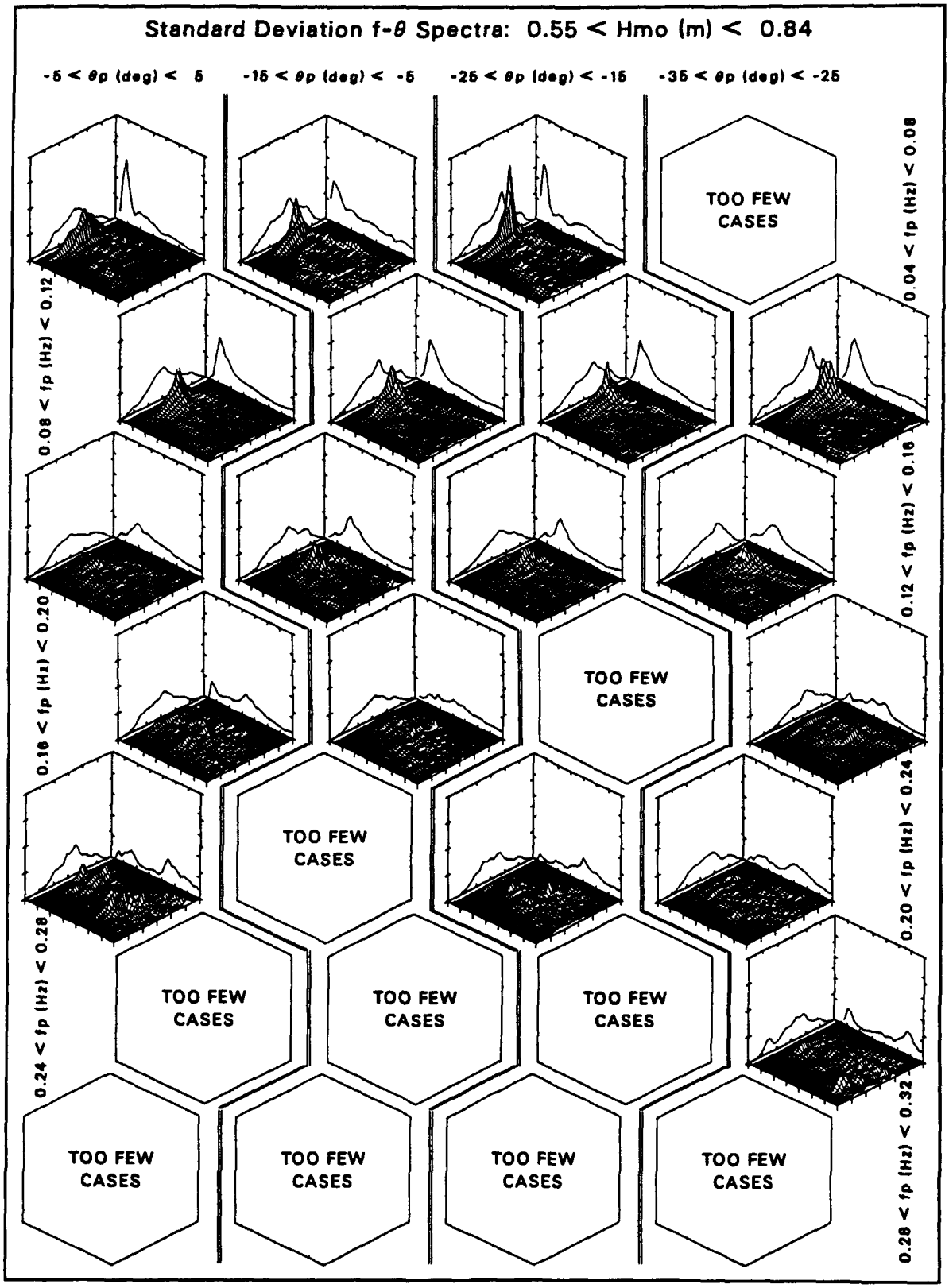
Standard Deviation f-θ Spectra: 0.55 < Hmo (m) < 0.84
-5 < θp (deg) < 5
-15 < θp (deg) < -5
-25 < θp (deg) < -15
-35 < θp (deg) < -25
0.04 < fp (Hz) < 0.08
0.08 < fp (Hz) < 0.12
0.12 < fp (Hz) < 0.16
0.16 < fp (Hz) < 0.20
0.20 < fp (Hz) < 0.24
0.24 < fp (Hz) < 0.28
0.28 < fp (Hz) < 0.32
TOO FEW CASES

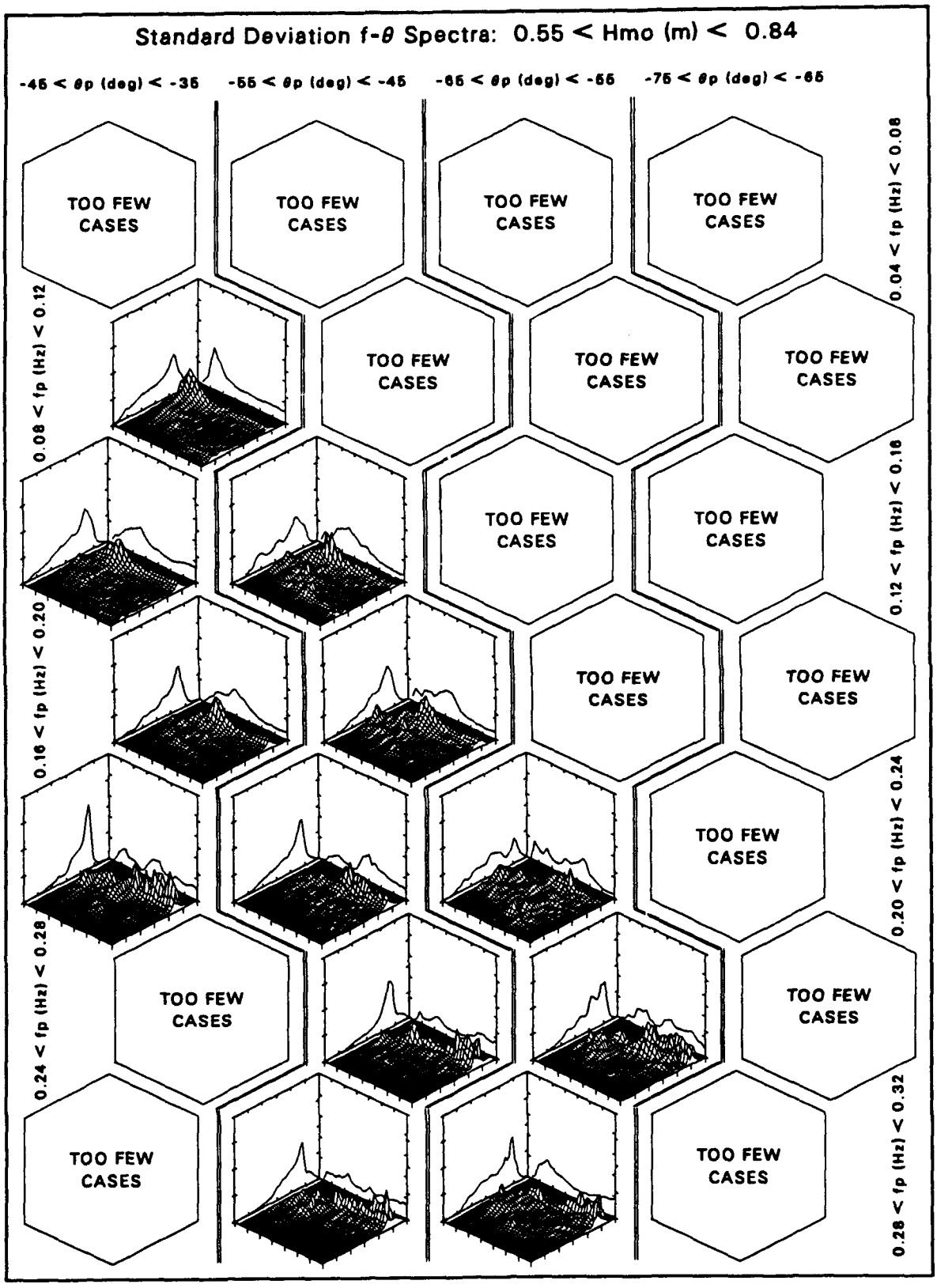
Standard Deviation f-θ Spectra: 0.55 < Hmo (m) < 0.84
-45 < θp (deg) < -35
-55 < θp (deg) < -45
-65 < θp (deg) < -55
-75 < θp (deg) < -65
0.04 < fp (Hz) < 0.08
0.08 < fp (Hz) < 0.12
0.12 < fp (Hz) < 0.16
0.16 < fp (Hz) < 0.20
0.20 < fp (Hz) < 0.24
0.24 < fp (Hz) < 0.28
0.28 < fp (Hz) < 0.32
TOO FEW CASES

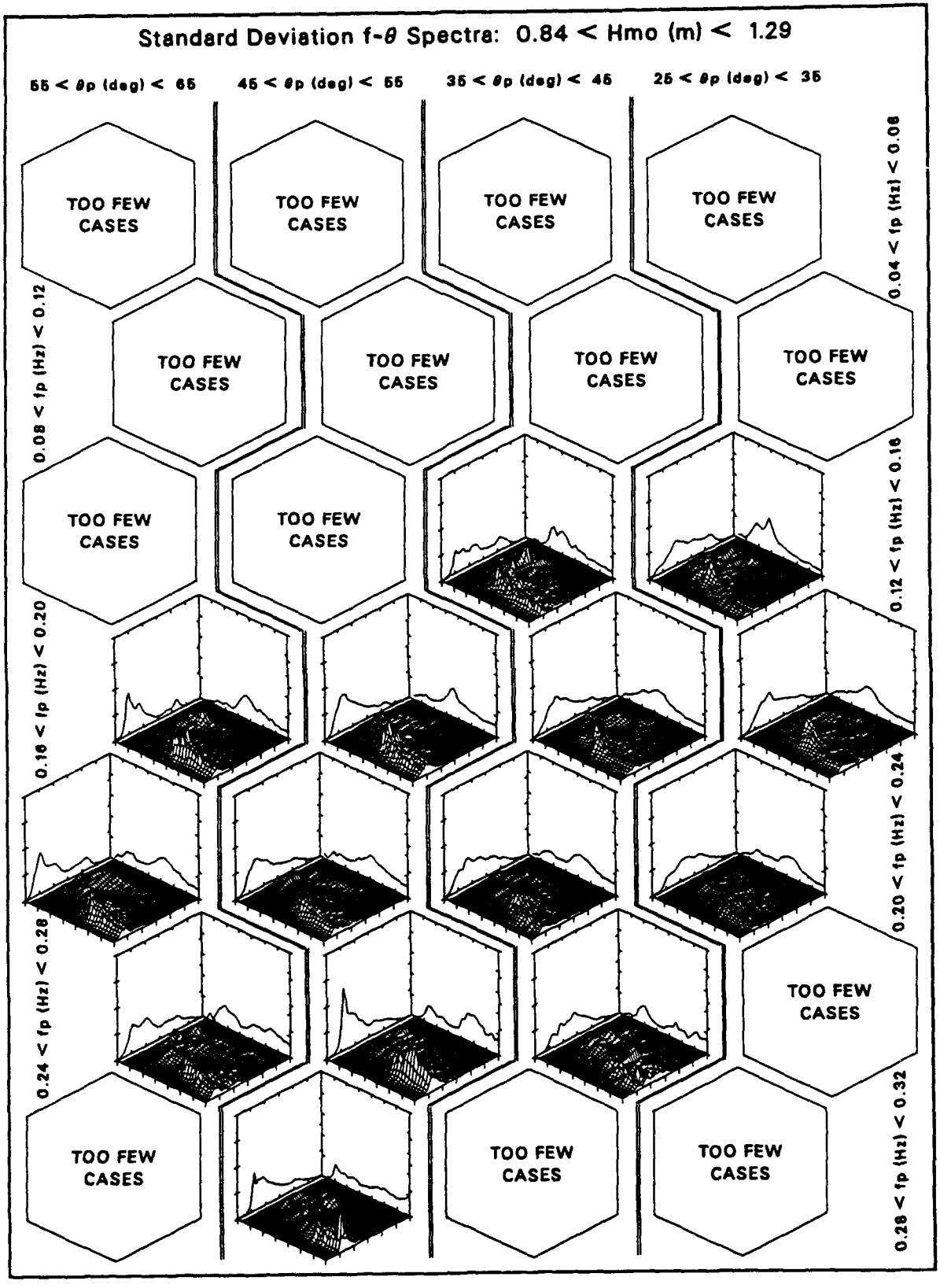
Standard Deviation f-θ Spectra: 0.84 < Hmo (m) < 1.29
55 < θp (deg) < 65
45 < θp (deg) < 55
35 < θp (deg) < 45
25 < θp (deg) < 35
0.04 < fp (Hz) < 0.08
0.08 < fp (Hz) < 0.12
0.12 < fp (Hz) < 0.16
0.16 < fp (Hz) < 0.20
0.20 < fp (Hz) < 0.24
0.24 < fp (Hz) < 0.28
0.28 < fp (Hz) < 0.32
TOO FEW CASES

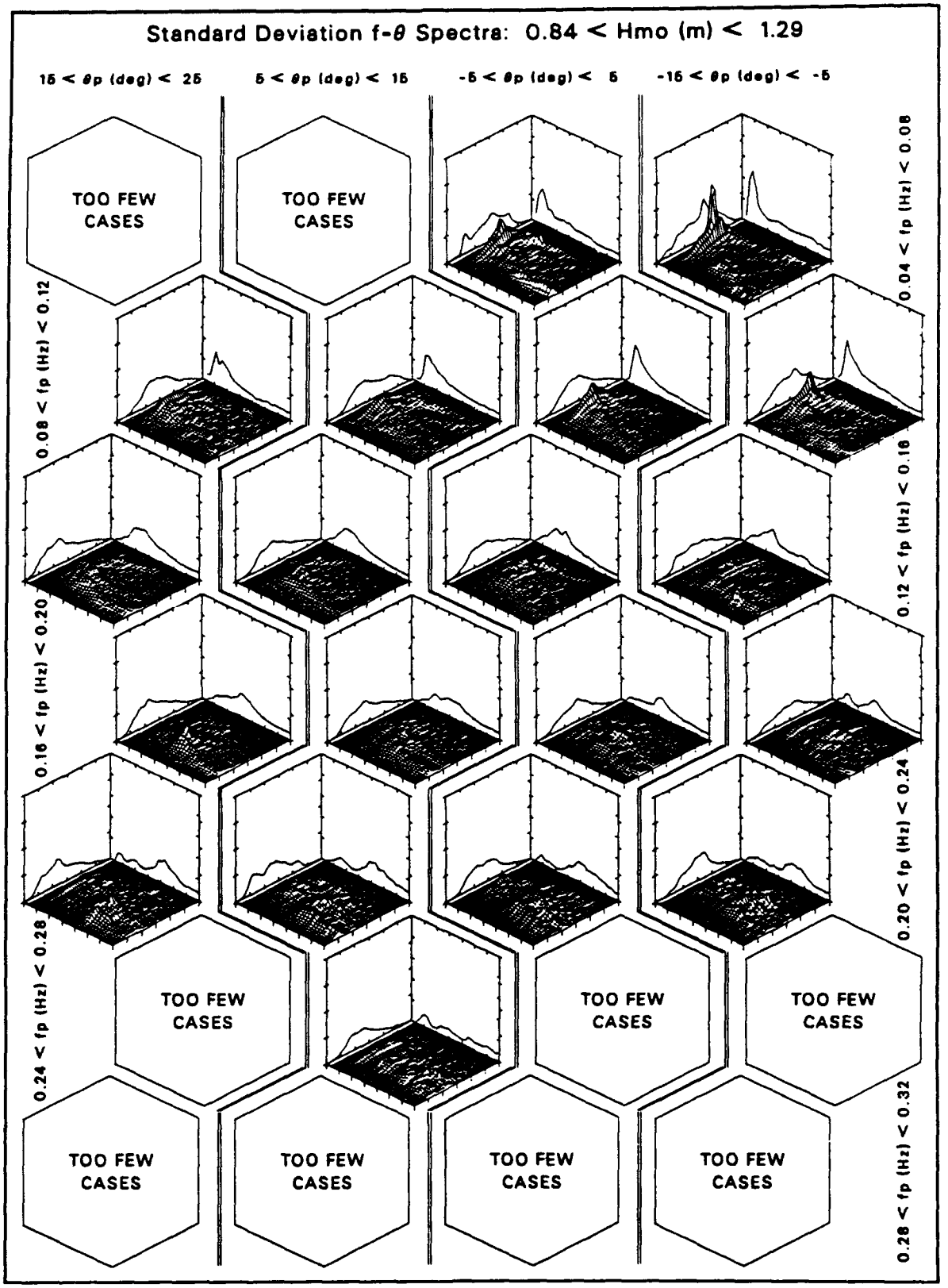
Standard Deviation f-θ Spectra: 0.84 < Hmo (m) < 1.29
15 < θp (deg) < 25
5 < θp (deg) < 15
-5 < θp (deg) < 5
-15 < θp (deg) < -5
0.04 < fp (Hz) < 0.08
0.08 < fp (Hz) < 0.12
0.12 < fp (Hz) < 0.16
0.16 < fp (Hz) < 0.20
0.20 < fp (Hz) < 0.24
0.24 < fp (Hz) < 0.28
0.28 < fp (Hz) < 0.32
TOO FEW CASES

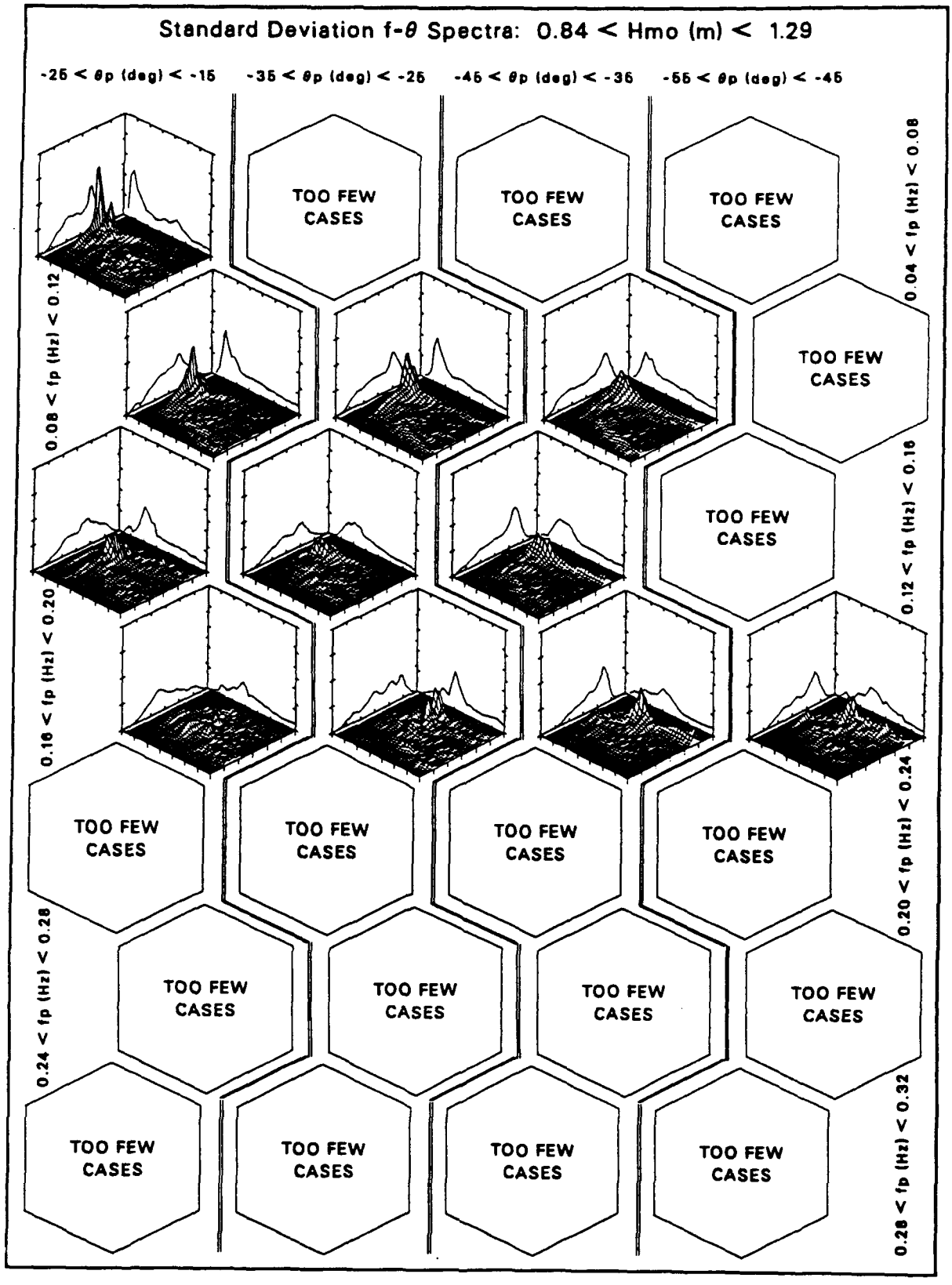
Standard Deviation f-θ Spectra: 0.84 < Hmo (m) < 1.29
-25 < θp (deg) < -15
-35 < θp (deg) < -25
-45 < θp (deg) < -35
-55 < θp (deg) < -45
0.04 < fp (Hz) < 0.08
0.08 < fp (Hz) < 0.12
0.12 < fp (Hz) < 0.16
0.16 < fp (Hz) < 0.20
0.20 < fp (Hz) < 0.24
0.24 < fp (Hz) < 0.28
0.28 < fp (Hz) < 0.32
TOO FEW CASES

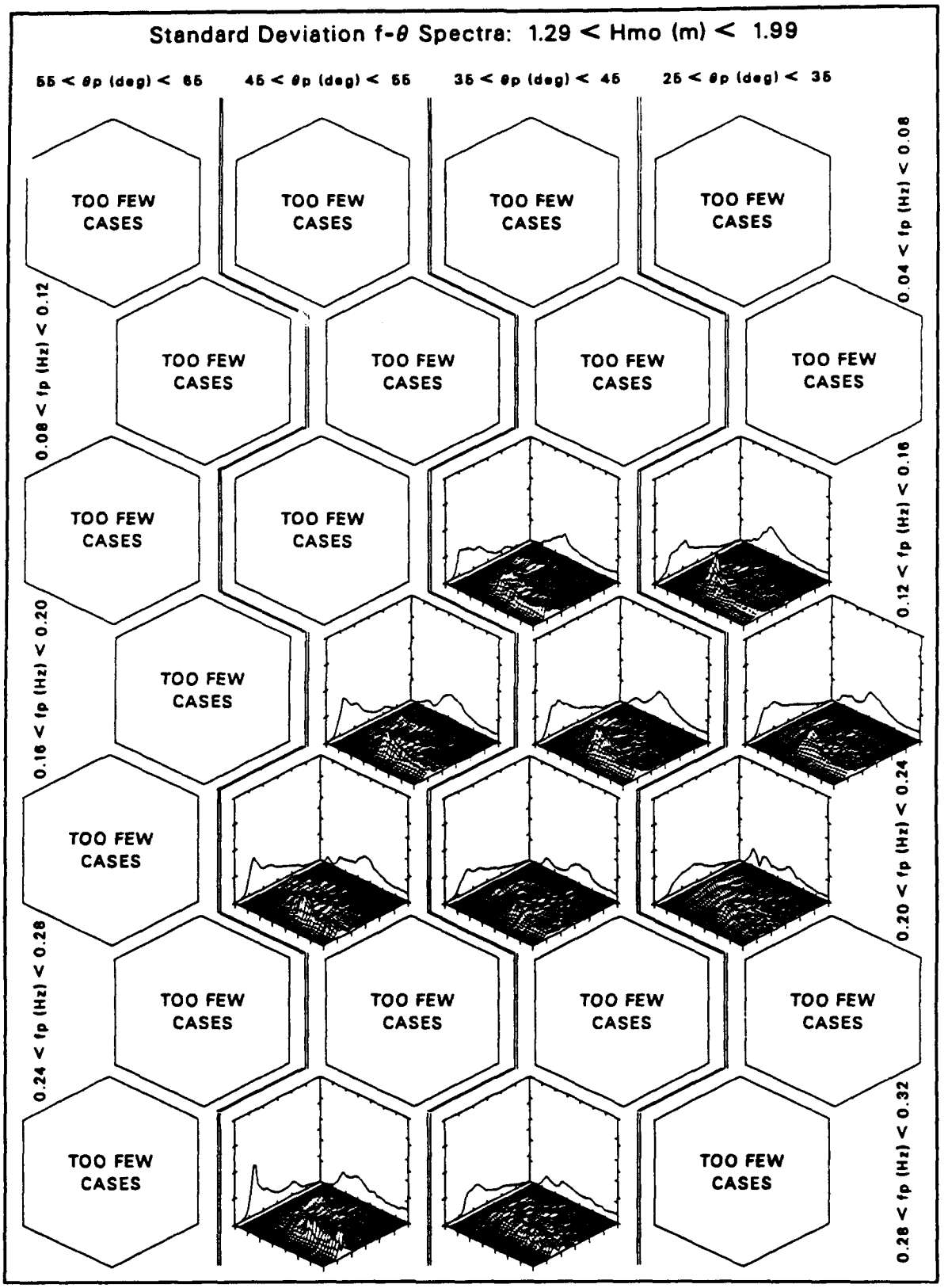
Standard Deviation f-θ Spectra: 1.29 < Hmo (m) < 1.99
55 < θp (deg) < 65
45 < θp (deg) < 55
35 < θp (deg) < 45
25 < θp (deg) < 35
0.04 < fp (Hz) < 0.08
0.08 < fp (Hz) < 0.12
0.12 < fp (Hz) < 0.16
0.16 < fp (Hz) < 0.20
0.20 < fp (Hz) < 0.24
0.24 < fp (Hz) < 0.28
0.28 < fp (Hz) < 0.32
TOO FEW CASES

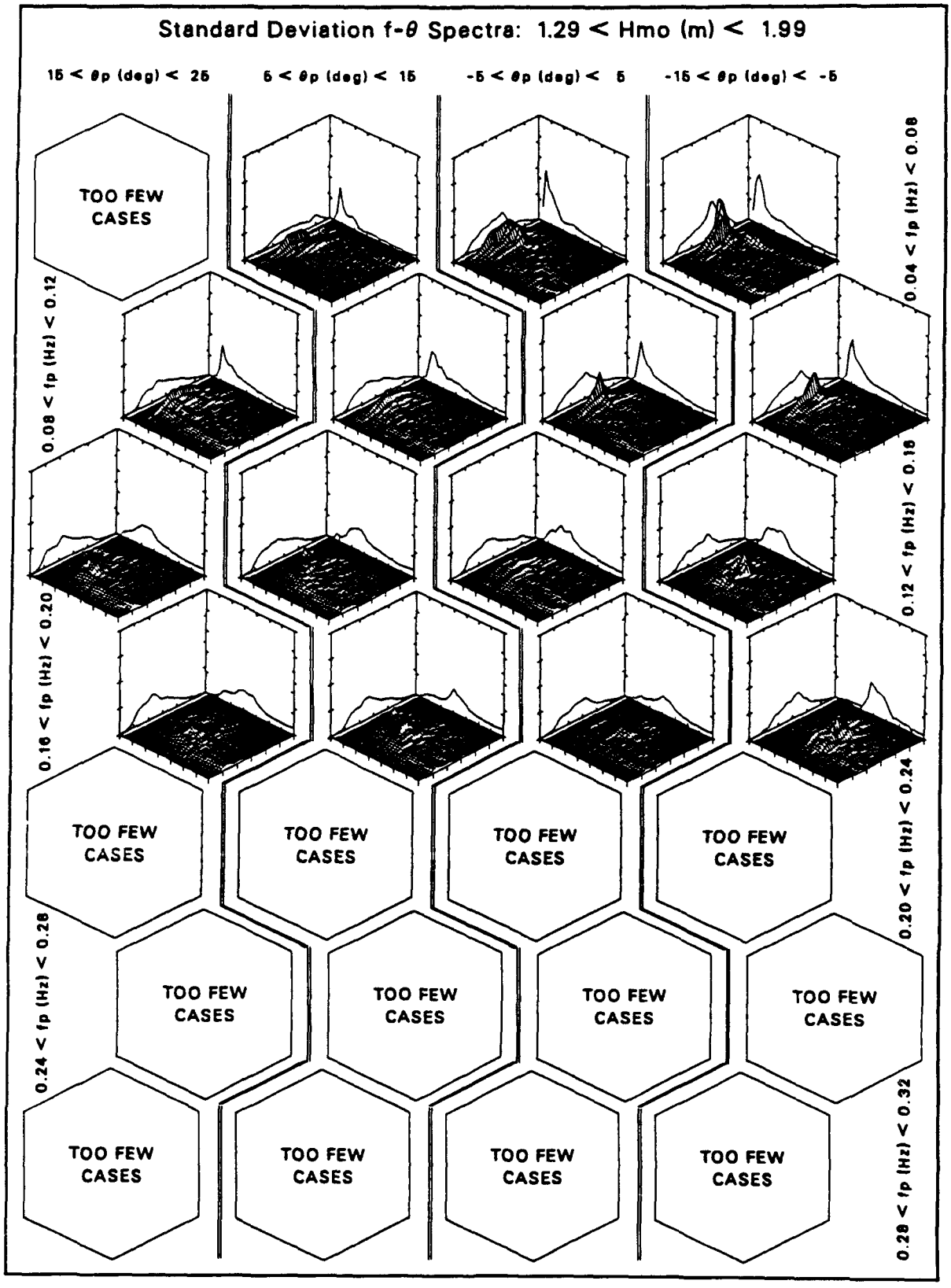
Standard Deviation f-θ Spectra: 1.29 < Hmo (m) < 1.99
15 < θp (deg) < 25
5 < θp (deg) < 15
-5 < θp (deg) < 5
-15 < θp (deg) < -5
0.04 < fp (Hz) < 0.08
0.08 < fp (Hz) < 0.12
0.12 < fp (Hz) < 0.16
0.16 < fp (Hz) < 0.20
0.20 < fp (Hz) < 0.24
0.24 < fp (Hz) < 0.28
0.28 < fp (Hz) < 0.32
TOO FEW CASES

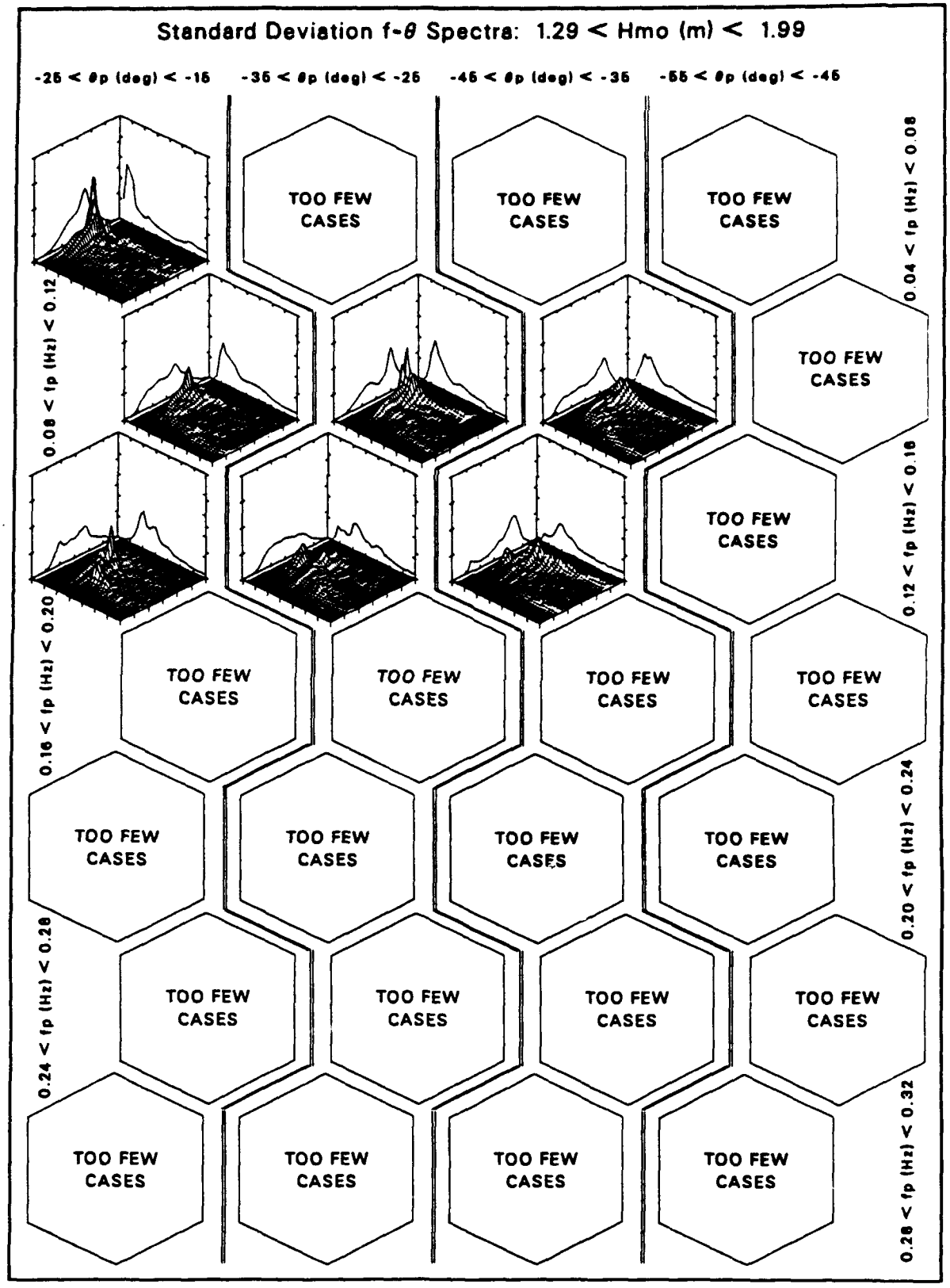
Standard Deviation f-θ Spectra: 1.29 < Hmo (m) < 1.99
-25 < θp (deg) < -15
-35 < θp (deg) < -25
-45 < θp (deg) < -35
-55 < θp (deg) < -45
0.04 < fp (Hz) < 0.08
0.08 < fp (Hz) < 0.12
0.12 < fp (Hz) < 0.16
0.16 < fp (Hz) < 0.20
0.20 < fp (Hz) < 0.24
0.24 < fp (Hz) < 0.28
0.28 < fp (Hz) < 0.32
TOO FEW CASES

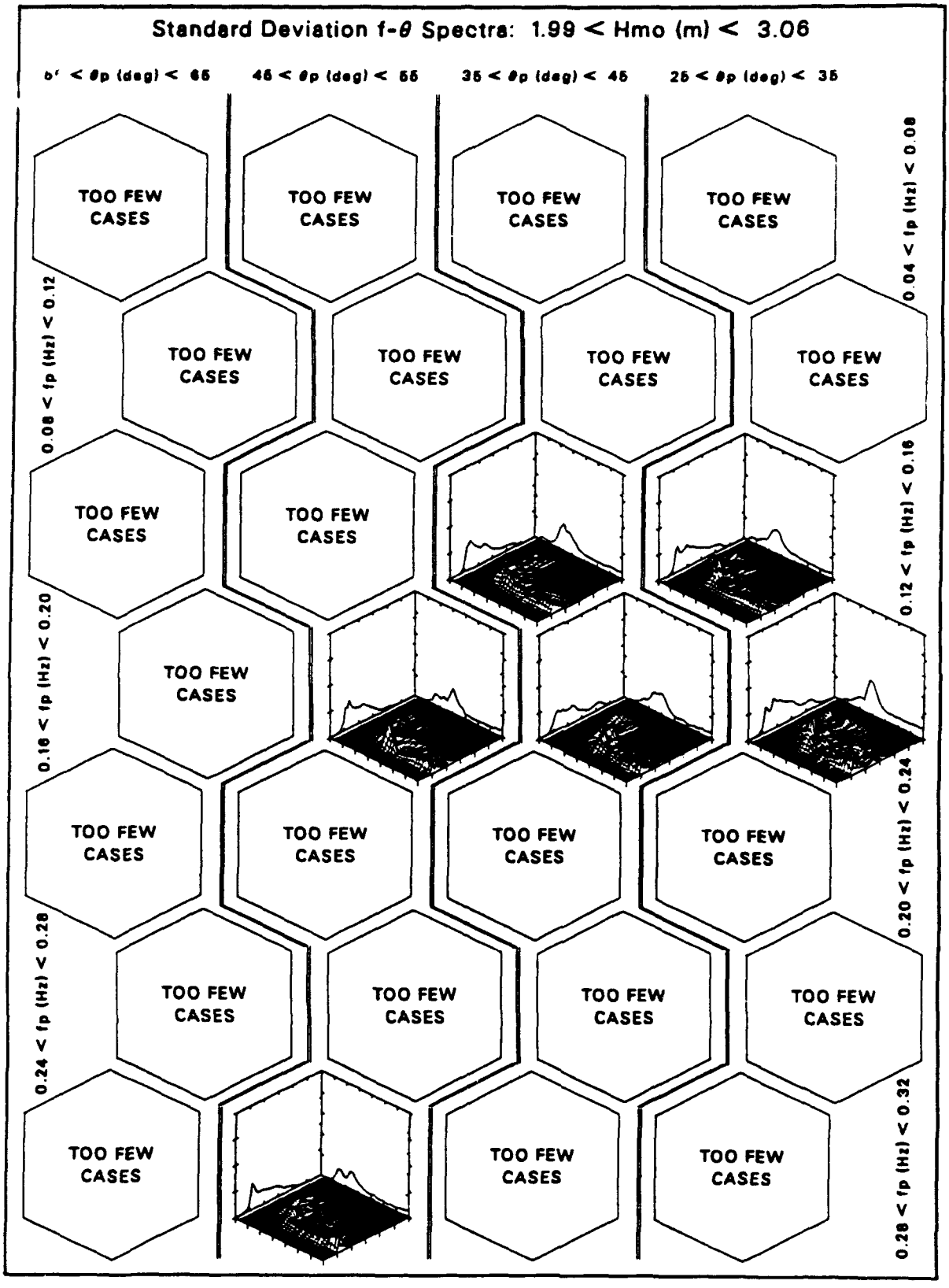
Standard Deviation f-θ Spectra: 1.99 < Hmo (m) < 3.06
65 < θp (deg) < 85
45 < θp (deg) < 65
35 < θp (deg) < 45
25 < θp (deg) < 35
0.04 < fp (Hz) < 0.08
0.08 < fp (Hz) < 0.12
0.12 < fp (Hz) < 0.16
0.16 < fp (Hz) < 0.20
0.20 < fp (Hz) < 0.24
0.24 < fp (Hz) < 0.28
0.28 < fp (Hz) < 0.32
TOO FEW CASES

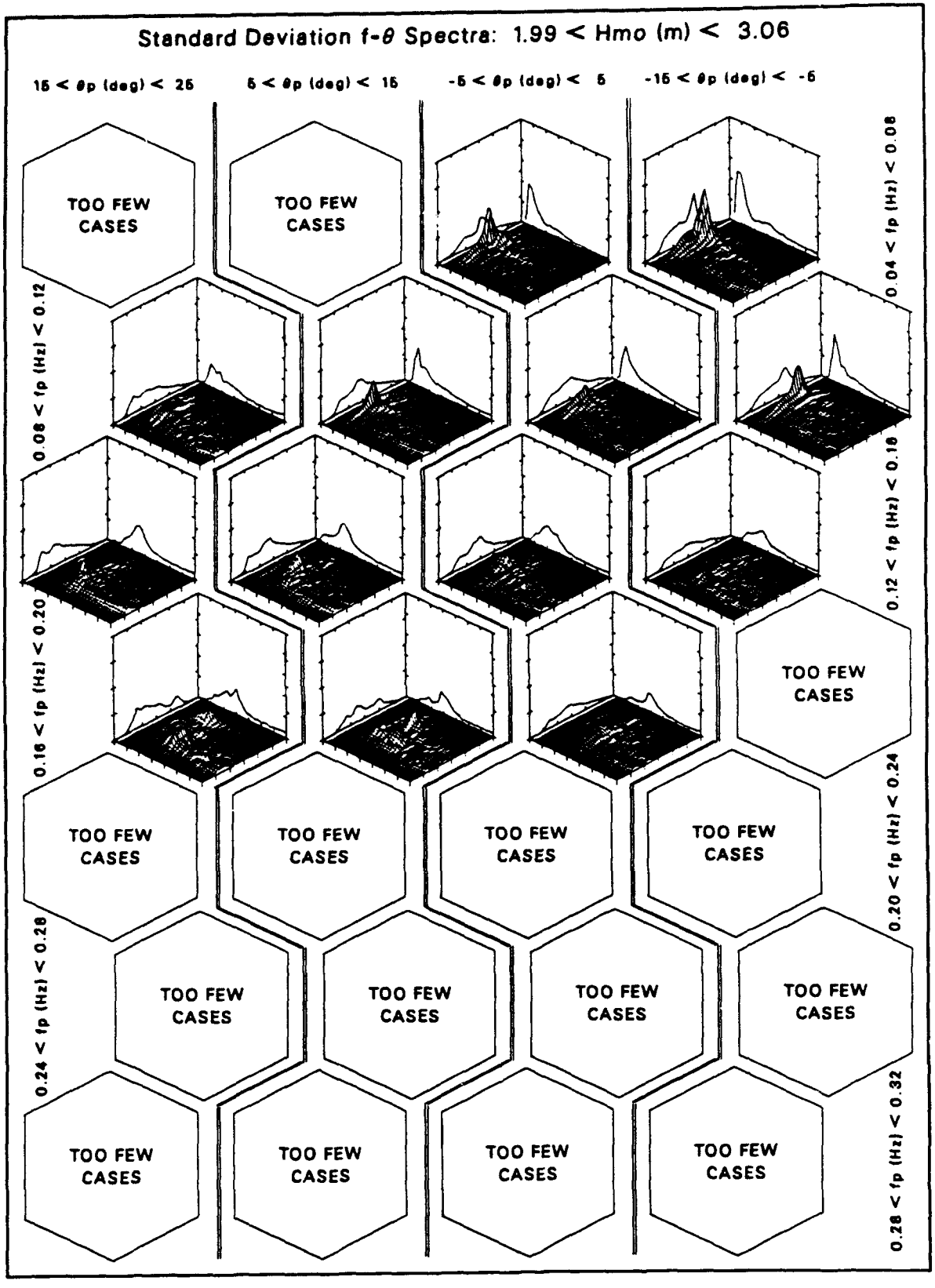
Standard Deviation f-θ Spectra: 1.99 < Hmo (m) < 3.06
15 < θp (deg) < 25
5 < θp (deg) < 15
-5 < θp (deg) < 5
-15 < θp (deg) < -5
0.04 < fp (Hz) < 0.08
0.08 < fp (Hz) < 0.12
0.12 < fp (Hz) < 0.16
0.16 < fp (Hz) < 0.20
0.20 < fp (Hz) < 0.24
0.24 < fp (Hz) < 0.28
0.28 < fp (Hz) < 0.32
TOO FEW CASES

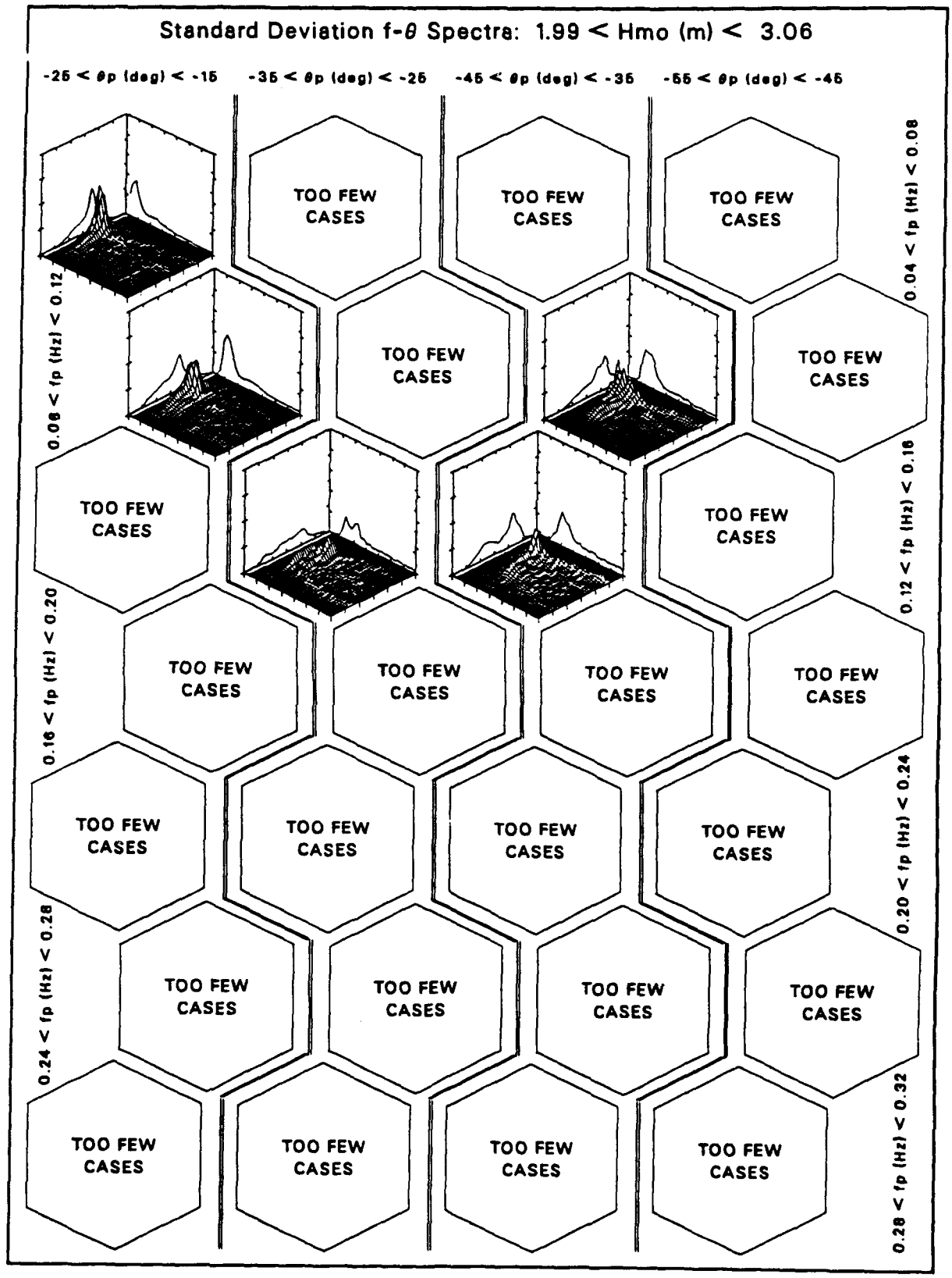
Standard Deviation f-θ Spectra: 1.99 < Hmo (m) < 3.06
-25 < θp (deg) < -15
-35 < θp (deg) < -25
-45 < θp (deg) < -35
-55 < θp (deg) < -45
0.04 < fp (Hz) < 0.08
0.08 < fp (Hz) < 0.12
0.12 < fp (Hz) < 0.16
0.16 < fp (Hz) < 0.20
0.20 < fp (Hz) < 0.24
0.24 < fp (Hz) < 0.28
0.28 < fp (Hz) < 0.32
TOO FEW CASES

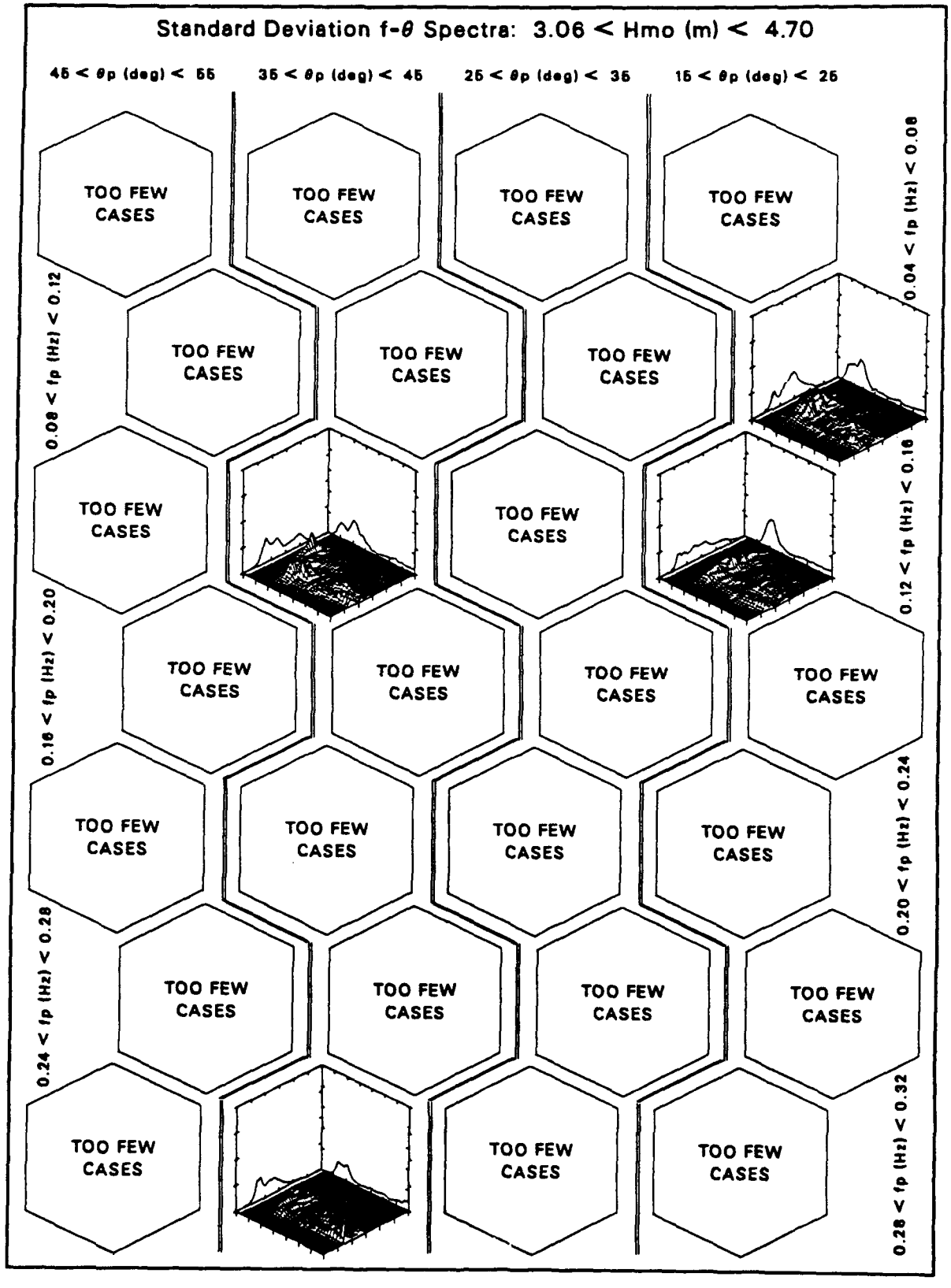
Standard Deviation f-θ Spectra: 3.06 < Hmo (m) < 4.70
45 < θp (deg) < 55
35 < θp (deg) < 45
25 < θp (deg) < 35
15 < θp (deg) < 25
0.04 < fp (Hz) < 0.08
0.08 < fp (Hz) < 0.12
0.12 < fp (Hz) < 0.16
0.16 < fp (Hz) < 0.20
0.20 < fp (Hz) < 0.24
0.24 < fp (Hz) < 0.28
0.28 < fp (Hz) < 0.32
TOO FEW CASES

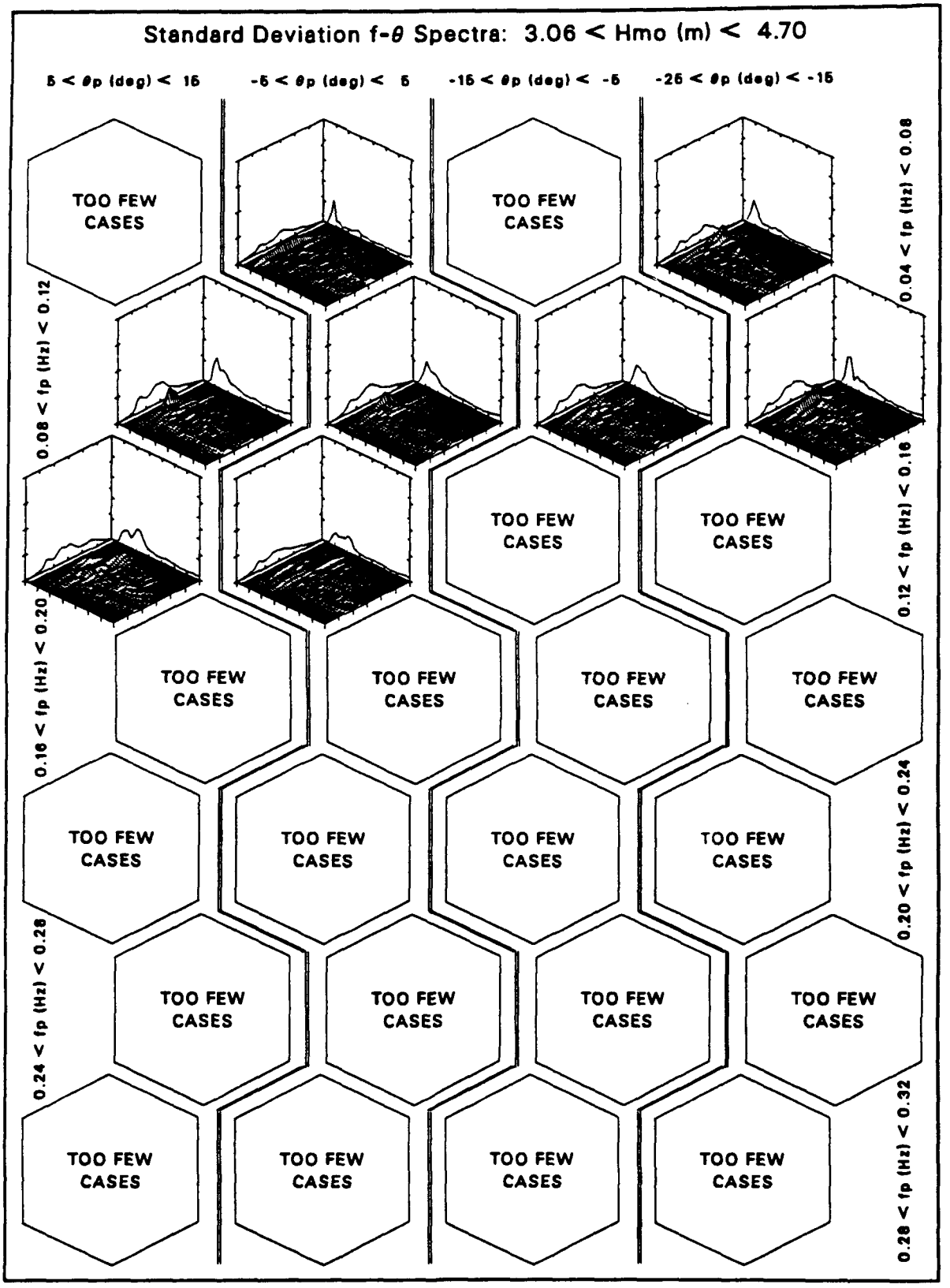
Standard Deviation f-θ Spectra: 3.06 < Hmo (m) < 4.70
5 < θp (deg) < 15
-5 < θp (deg) < 5
-15 < θp (deg) < -5
-25 < θp (deg) < -15
0.04 < fp (Hz) < 0.08
0.08 < fp (Hz) < 0.12
0.12 < fp (Hz) < 0.16
0.16 < fp (Hz) < 0.20
0.20 < fp (Hz) < 0.24
0.24 < fp (Hz) < 0.28
0.28 < fp (Hz) < 0.32
TOO FEW CASES

Appendix C
Figures Supporting Chapter 5

This appendix contains figures supporting the discussion in Chapter 5 regarding radiation stress tensor components S'_{xx}, the onshore transport of onshore wave momentum, and S'_{yy}, the alongshore transport of longshore wave momentum. These figures are placed here to reduce the space required in the main text, and because the arguments regarding these radiation stress components are rather similar to arguments given in Chapter 5 concerning radiation stress tensor component S'_{xy}, the onshore transport of longshore wave momentum.

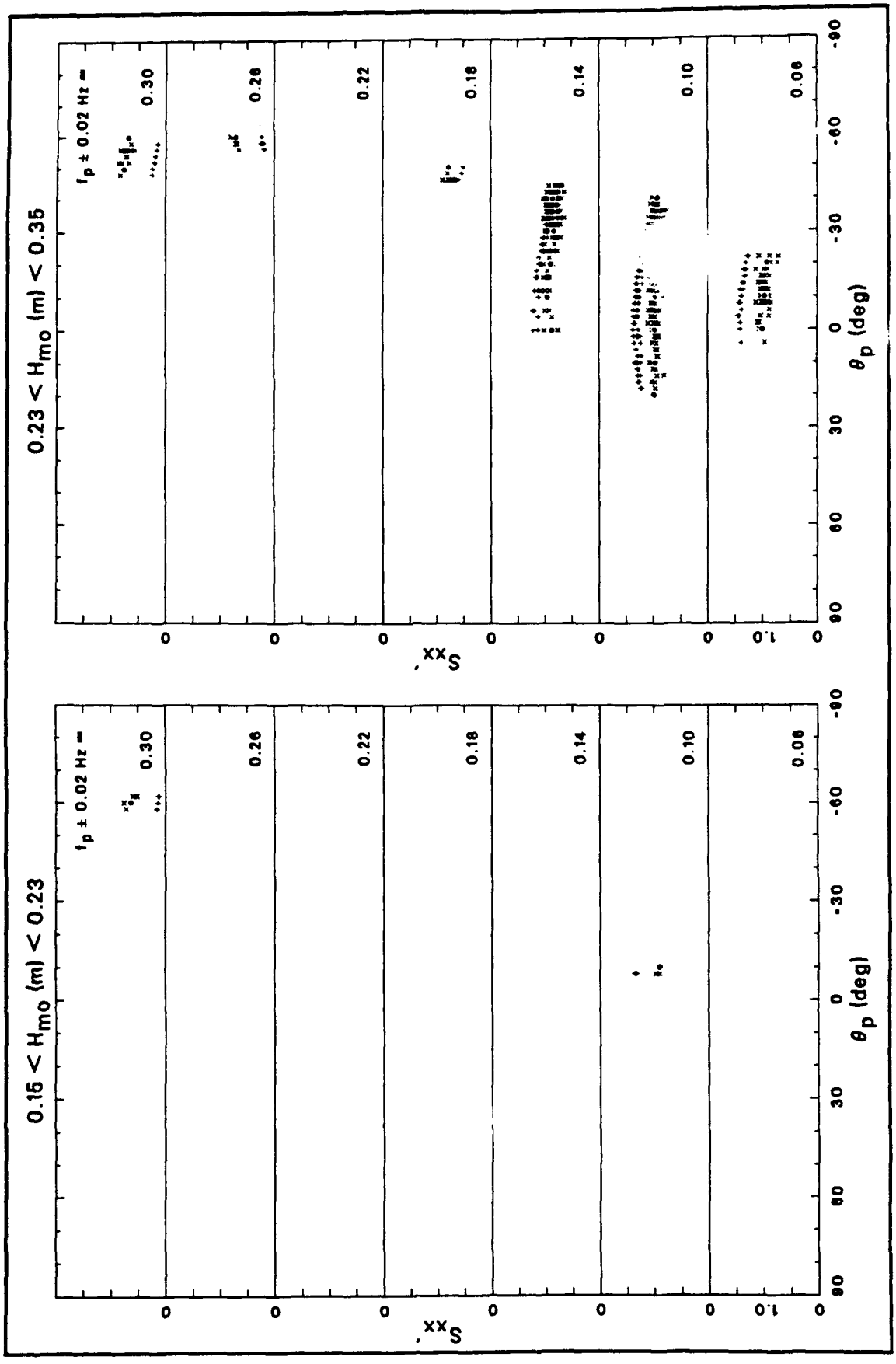

Figure C1. Estimates of S_{xx}' for wave heights between 0.15 and 0.35 m

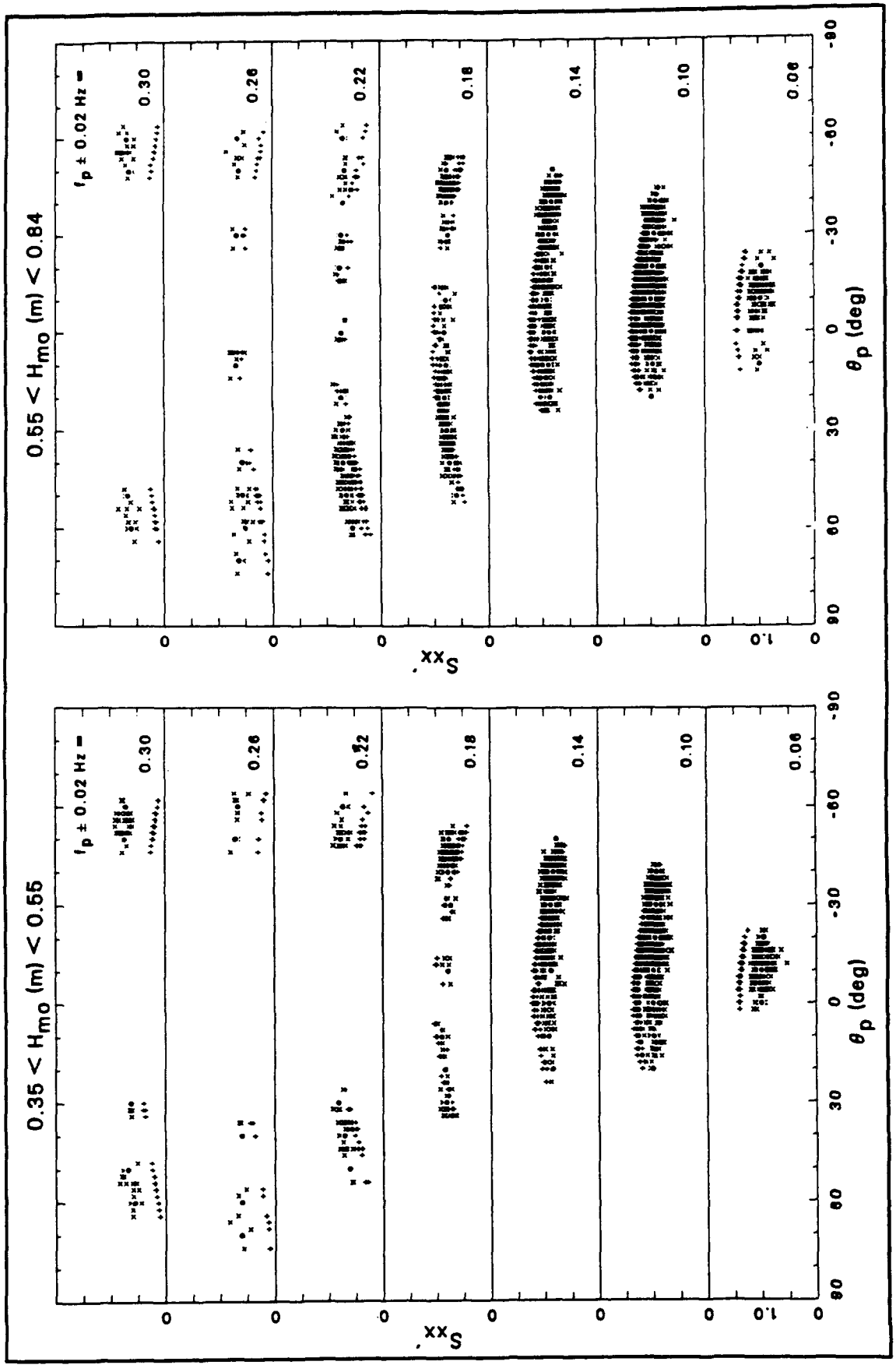

Figure C2. Estimates of S_{xx}' for wave heights between 0.35 and 0.84 m

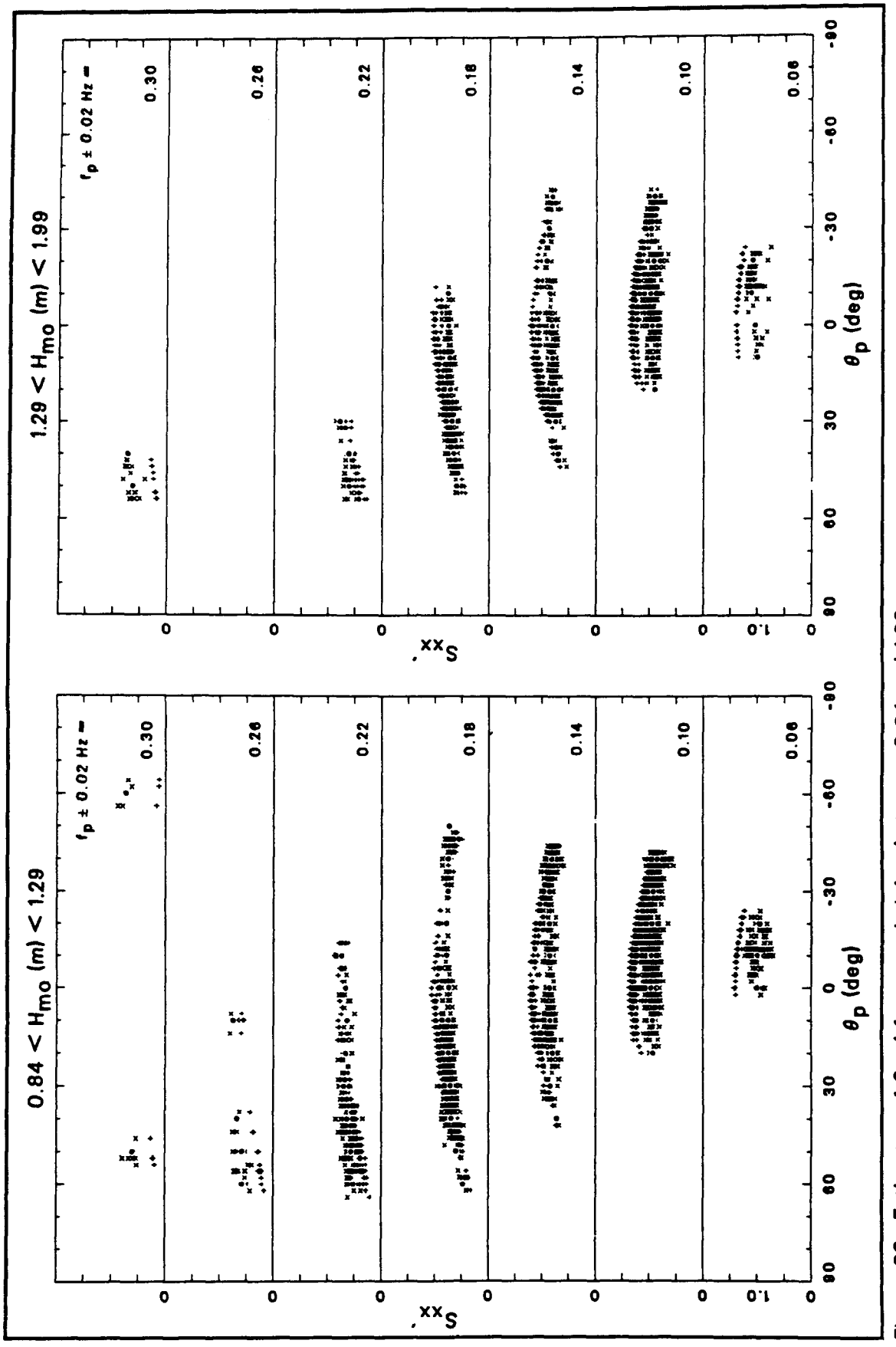

Figure C3. Estimates of $S_{xx'}$ for wave heights between 0.84 and 1.99 m

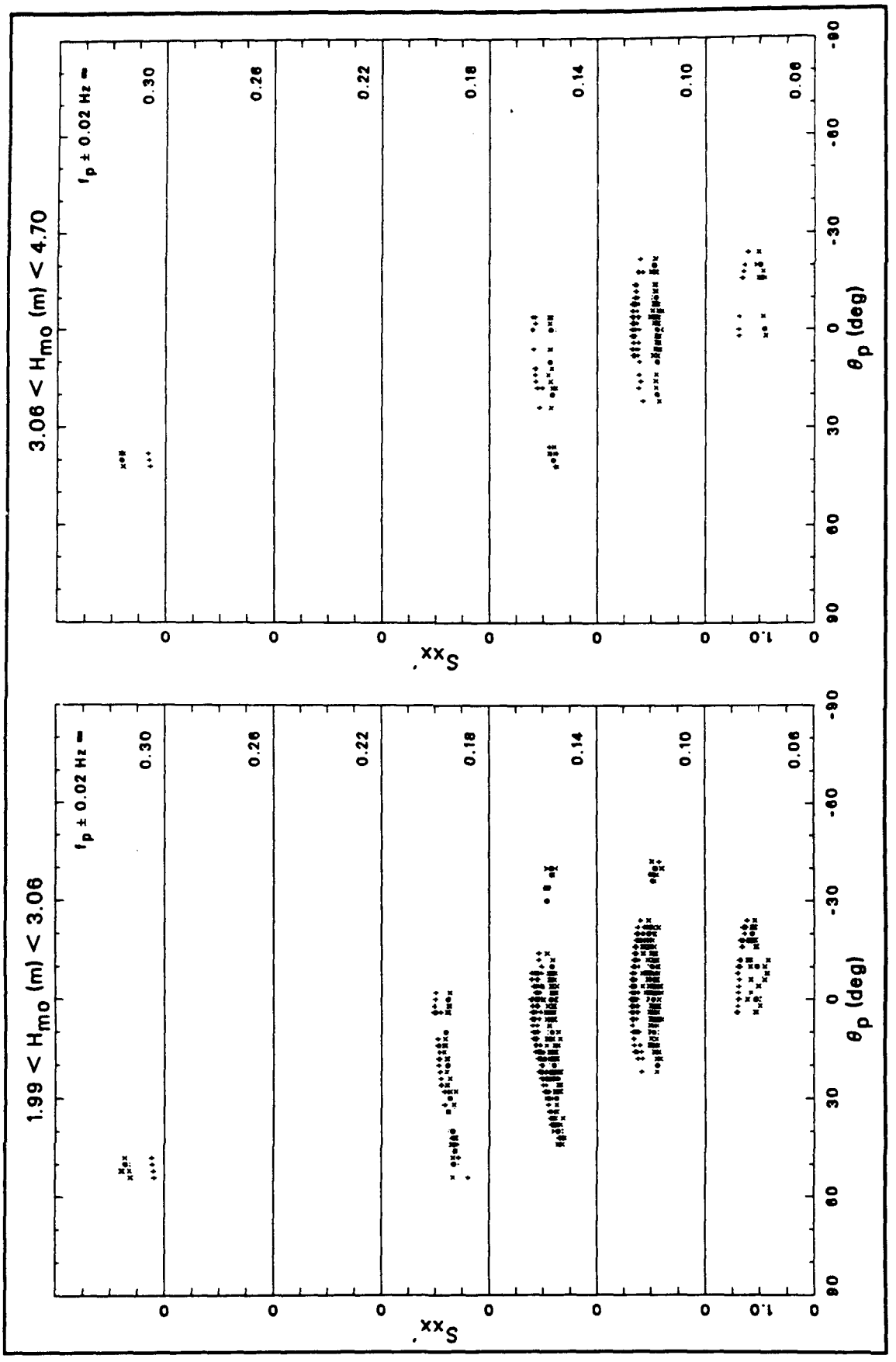

Figure C4. Estimates of S_{xx}' for wave heights between 1.99 and 4.70 m

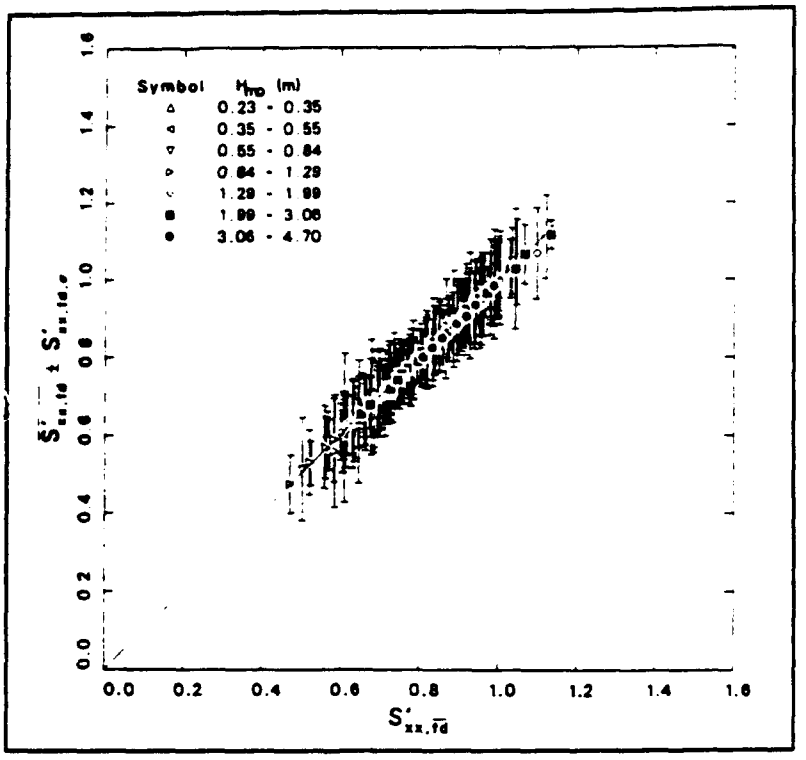

Figure C5. Correlation of S_{xx}' estimates from characteristic spectra with class statistics of constituent spectra

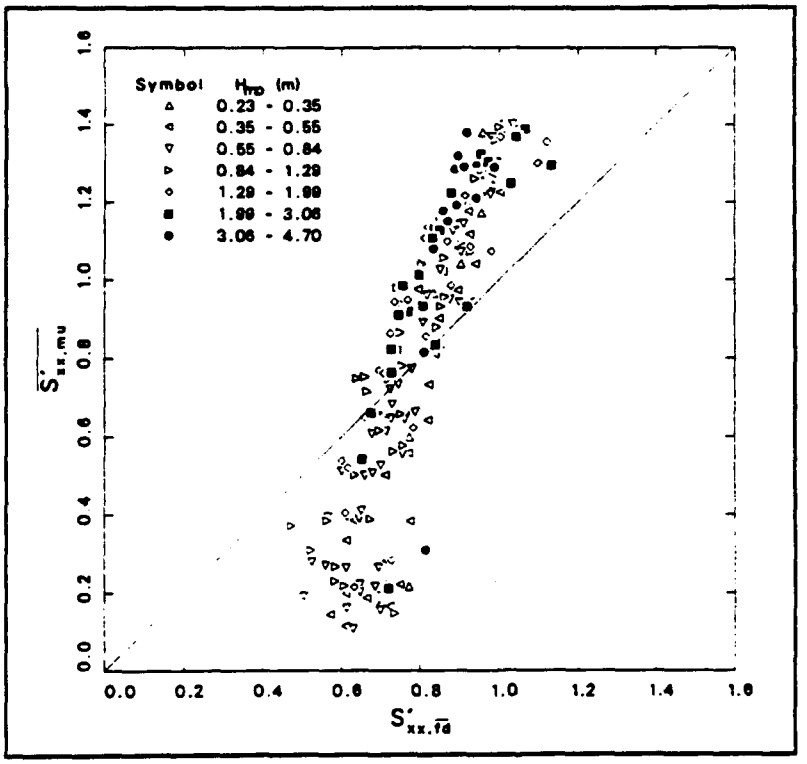

Figure C6. Correlation of S_{xx}' estimates from characteristic spectra with monochromatic, unidirectional class averages

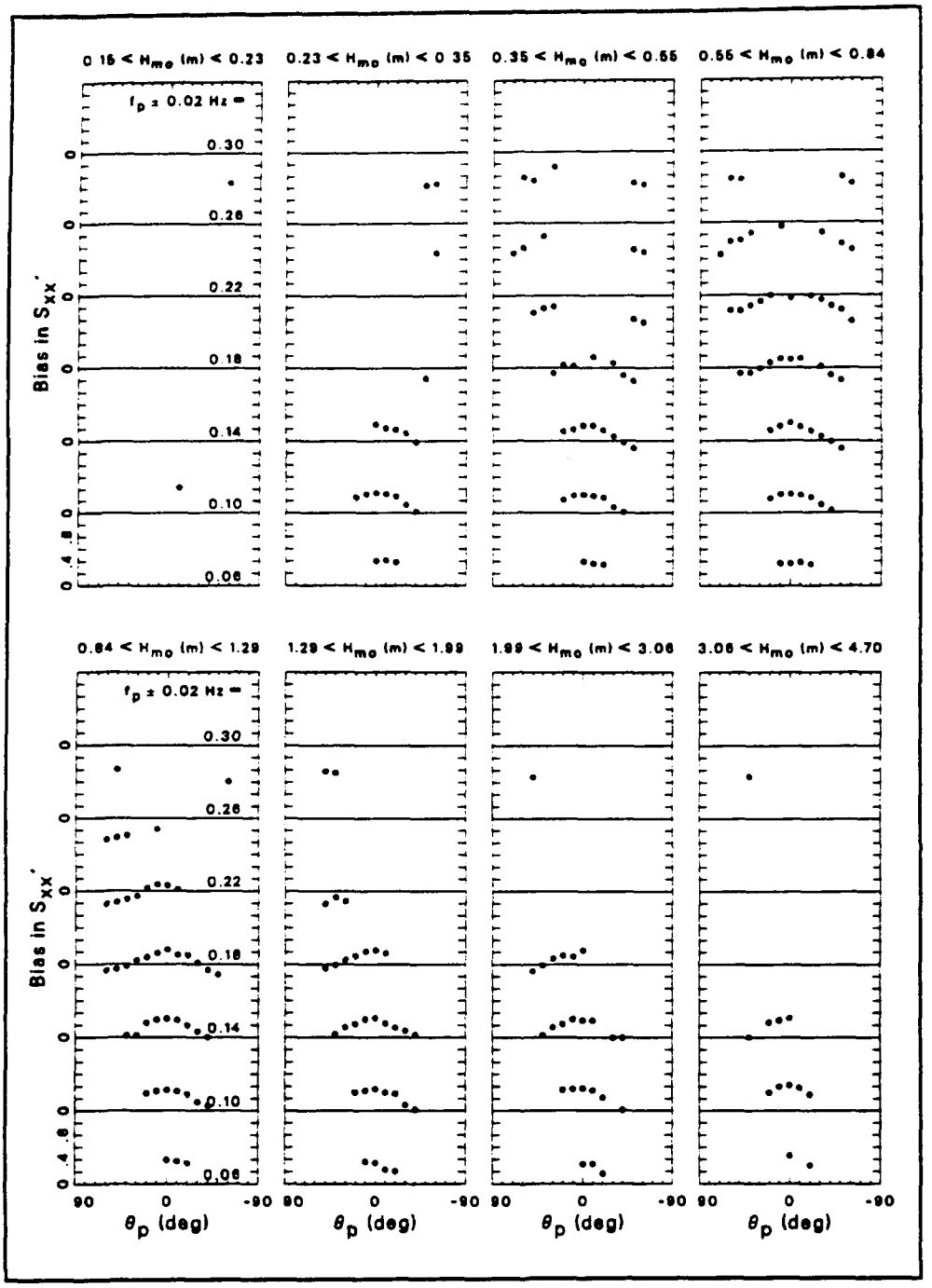

Figure C7. Bias in S_{xx}' estimates

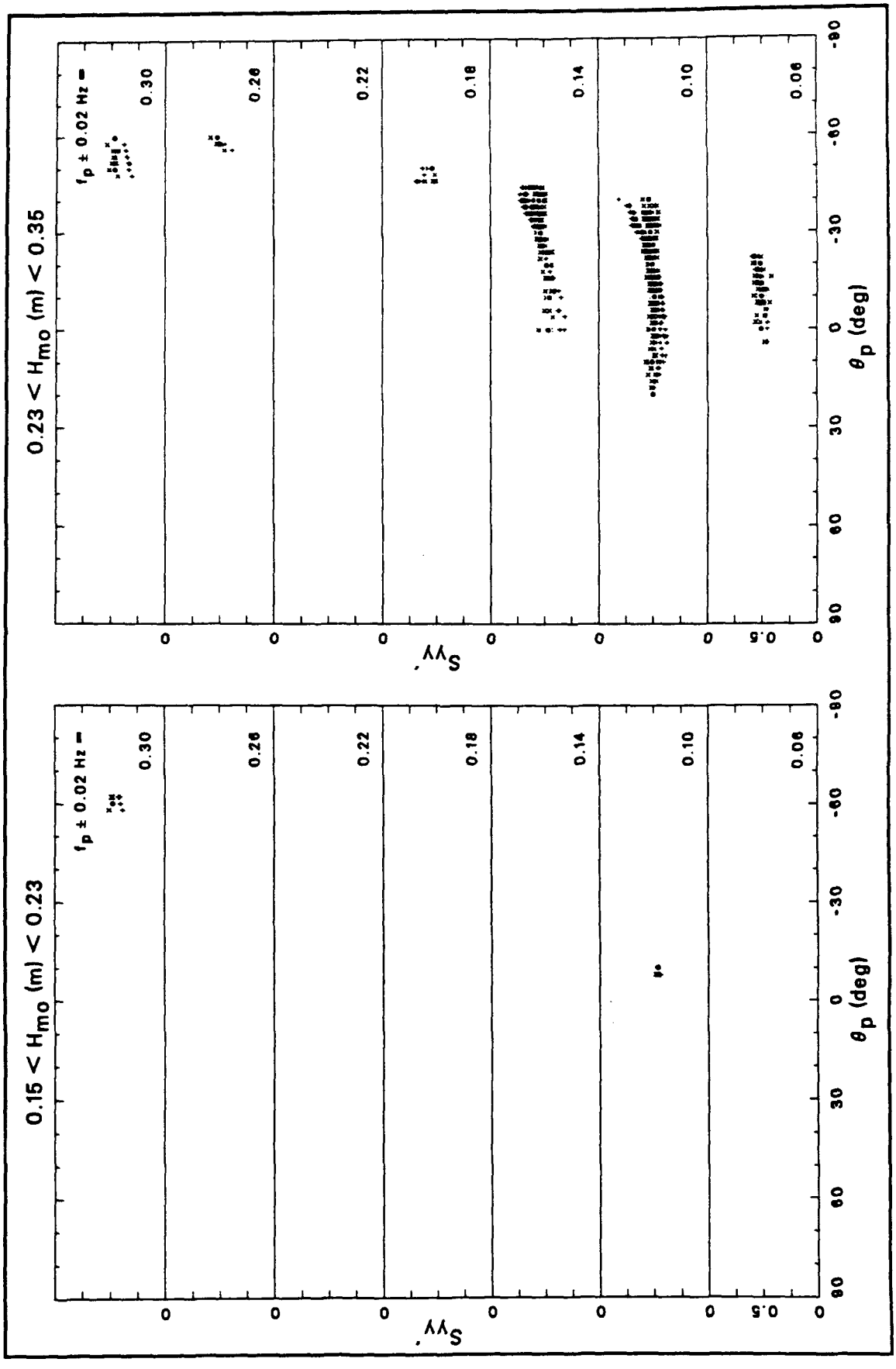

Figure C8. Estimates of S_{yy}' for wave heights between 0.15 and 0.35 m

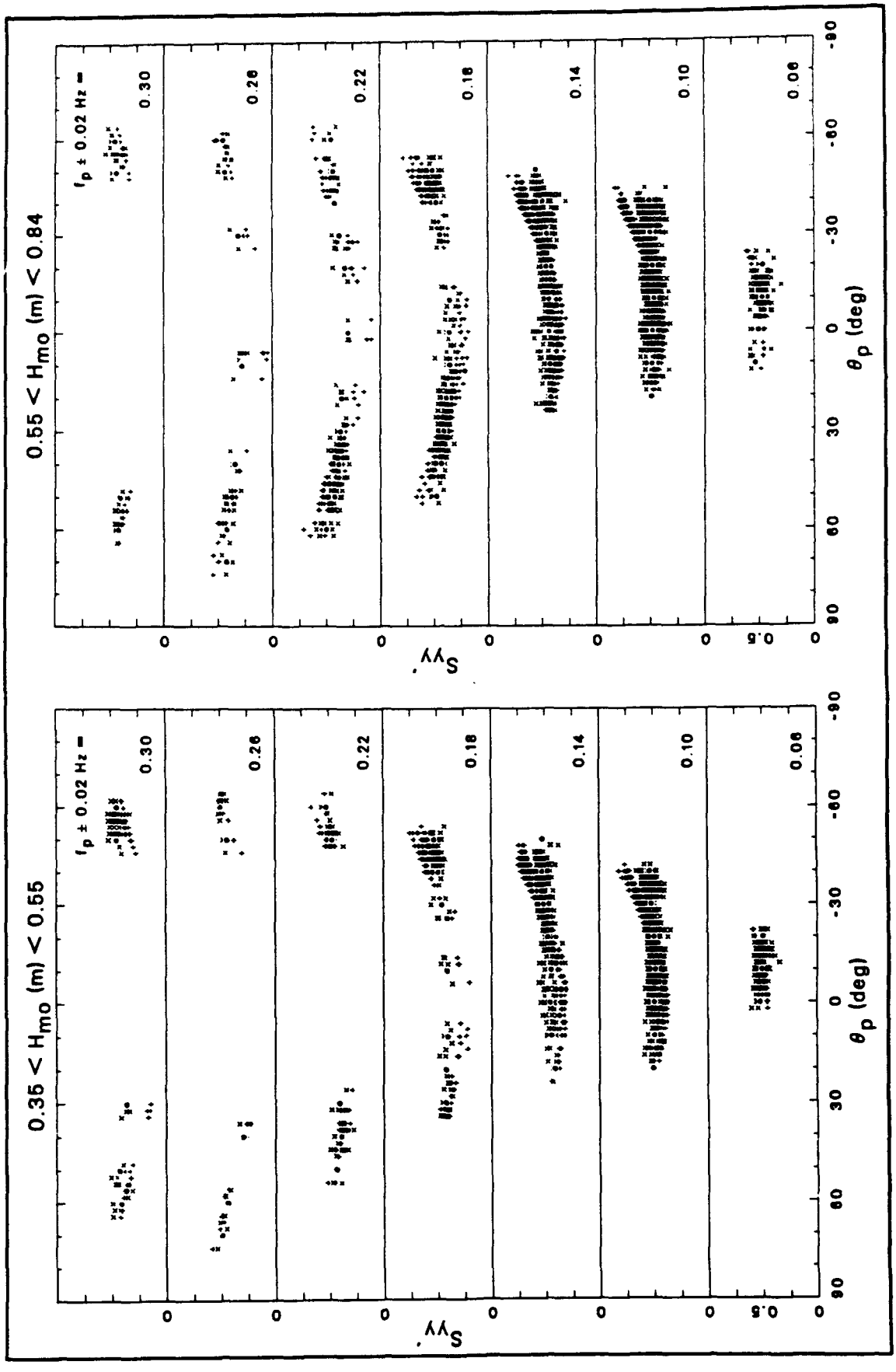

Figure C9. Estimates of S_{yy}' for wave heights between 0.35 and 0.84 m

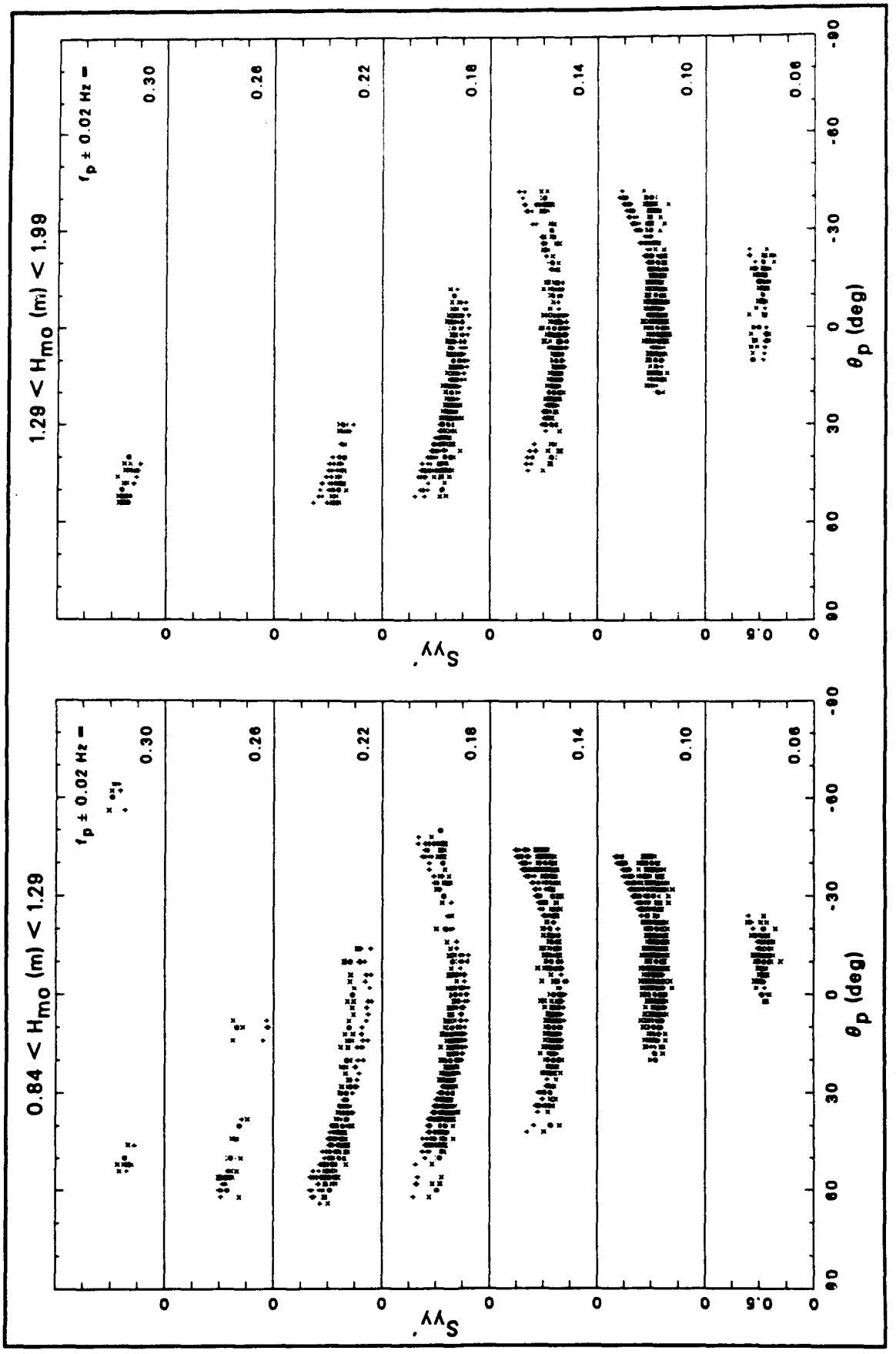

Figure C10. Estimates of S_{yy}' for wave heights between 0.84 and 1.99 m

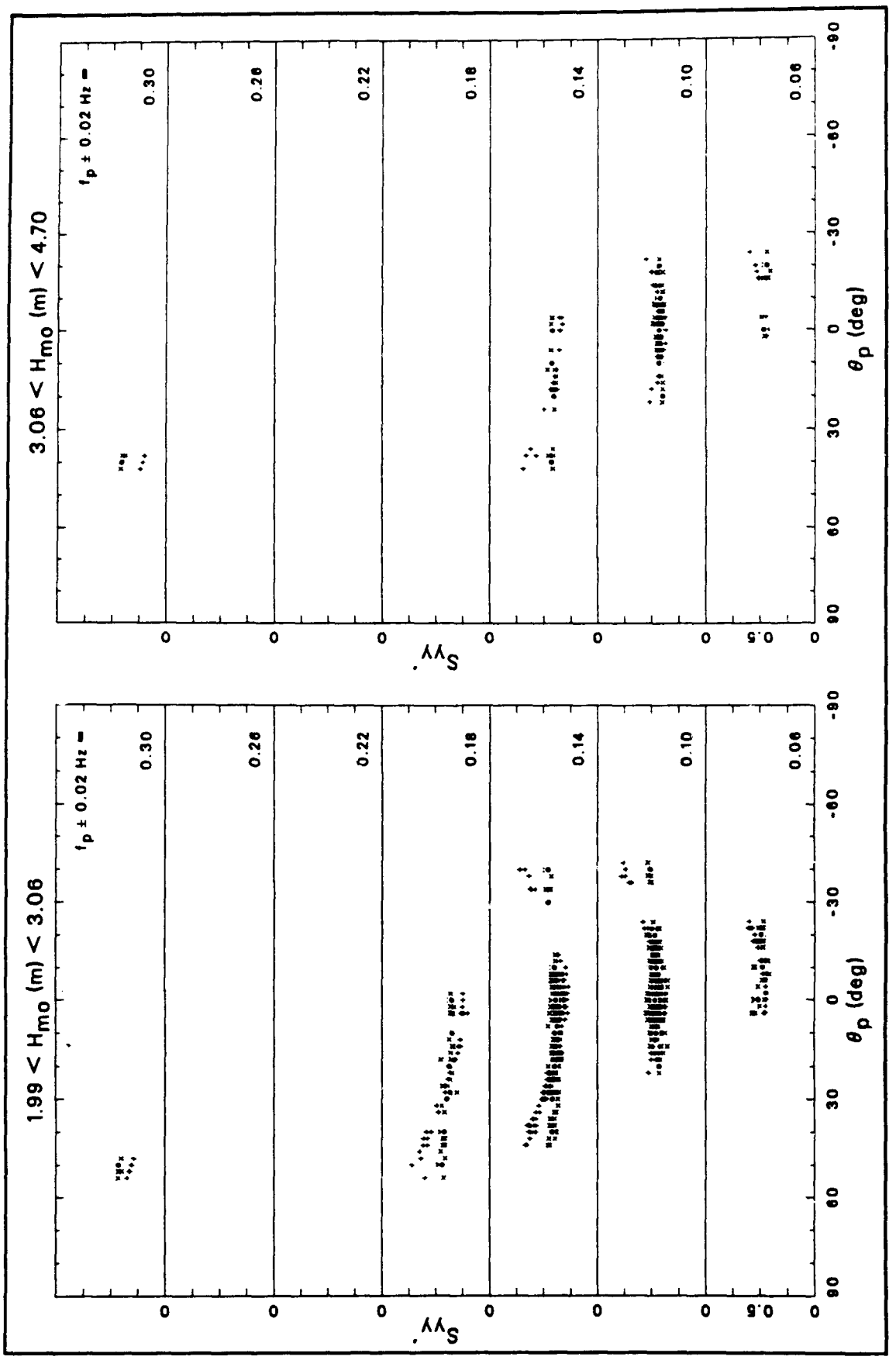

Figure C11. Estimates of S_{yy}' for wave heights between 1.99 and 4.70 m

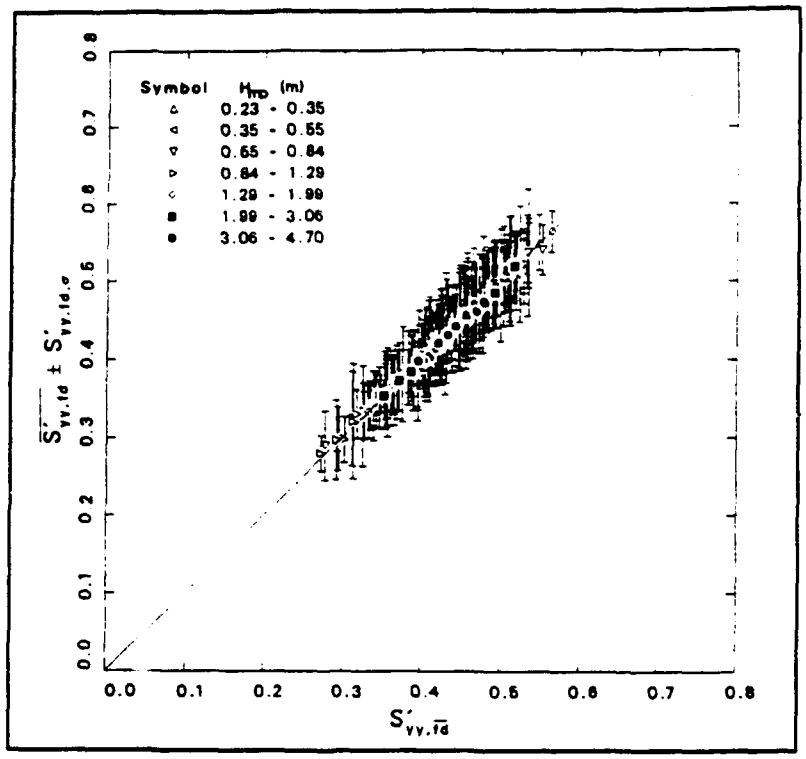

Figure C12. Correlation of S_{vv}' estimates from characteristic spectra with class statistics of constituent spectra

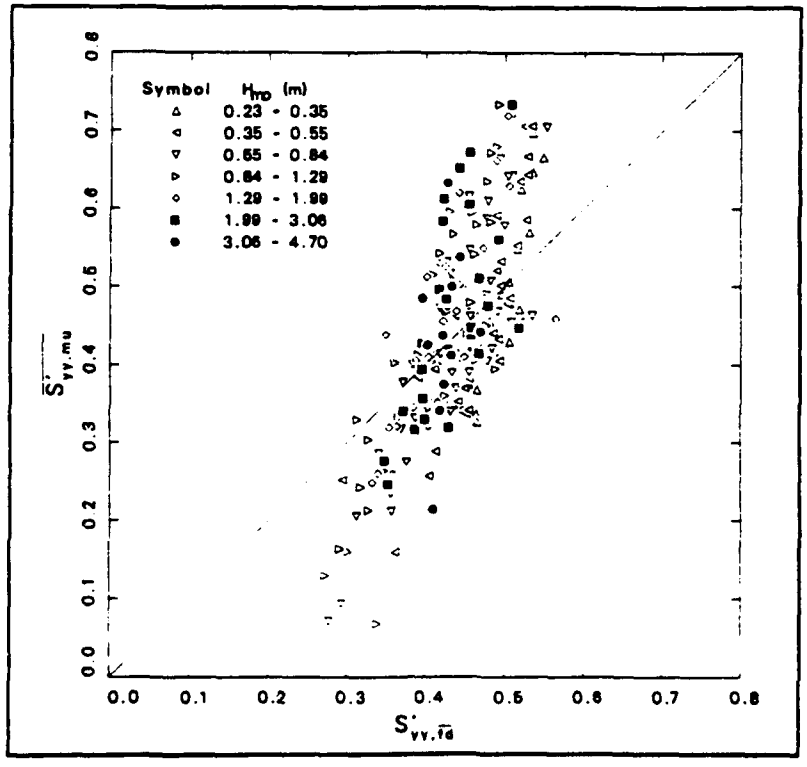

Figure C13. Correlation of S_{vv}' estimates from characteristic spectra with monochromatic, unidirectional class averages

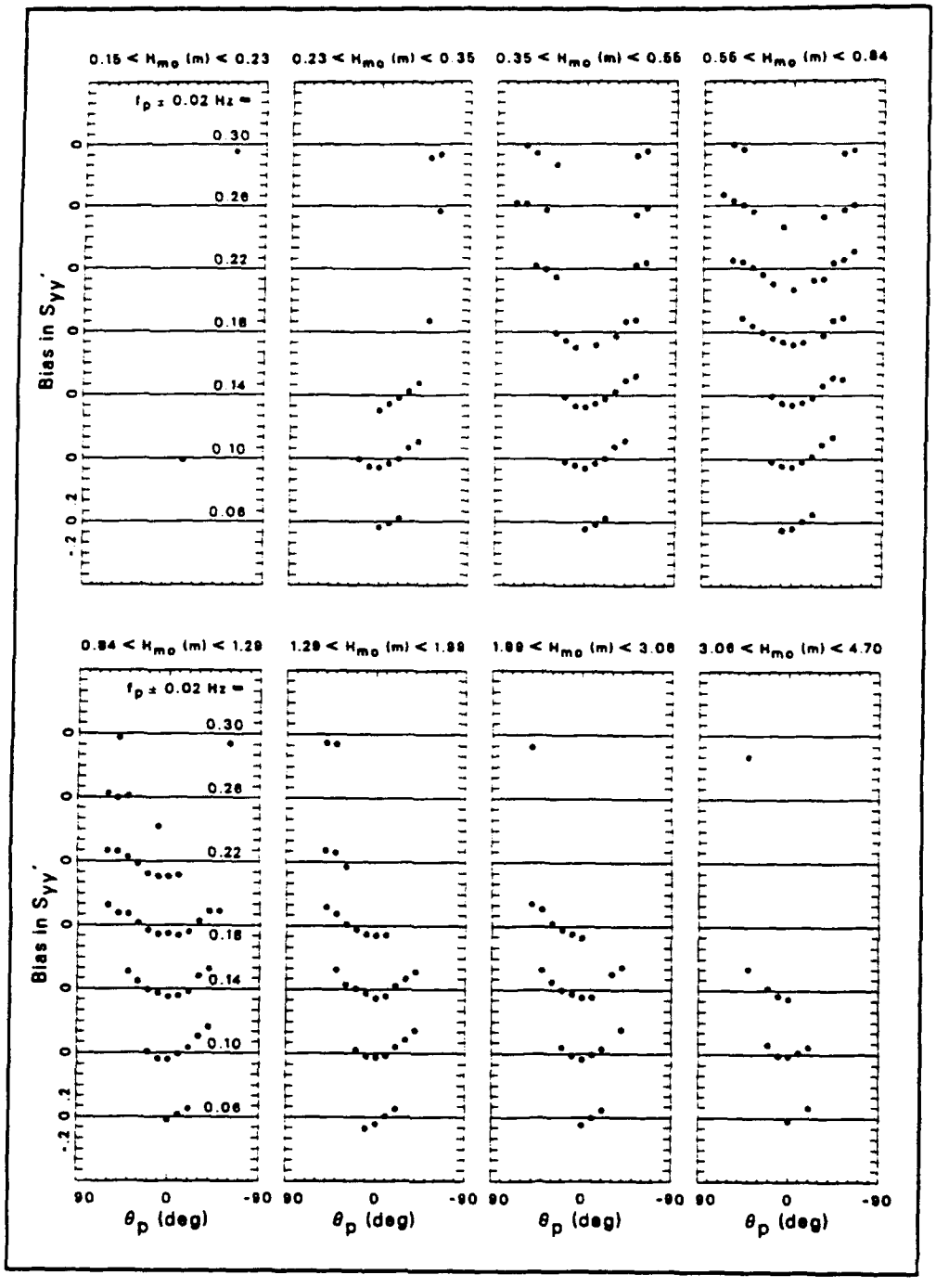

Figure C14. Bias in S_{yy}' estimates

Appendix D
Notation

$bias(H_{mo},f_p,\theta_p)$	A unidirectional, monochromatic estimate less the corresponding characteristic spectral estimate within a given three-parameter classification
$C(f_n,d)$	Wave phase speed at frequency f_n and water depth d
$C_g(f_n,d)$	Wave group velocity at frequency f_n and water depth d
d	Water depth
d_k	Water depth for k^{th} constituent spectrum
e_i	Trigonometric function
e_j	Trigonometric function
$e_1(\theta)$	cosine of an arbitrary angle θ
$e_2(\theta)$	sine of an arbitrary angle θ
f	Frequency
fd	Frequency-direction
f_n	n^{th} discrete frequency
f_p	Characteristic peak frequency
$f_{p,k}$	Characteristic peak frequency of k^{th} constituent spectrum
g	Gravitational acceleration

H	Wave height of monochromatic, unidirectional wave
H_{mo}	Energy-based characteristic wave height
$H_{mo,k}$	Characteristic wave height of k^{th} constituent spectrum
i	An index
j	An index
k	An index
K	Upper limit of index k
m	An index
M	Upper limit of index m
mu	Monochromatic, unidirectional
n	An index
N	Upper limit of index n
P_l	Longshore energy flux
$\hat{P}_l$	Corrected estimate of dimensional onshore transport of longshore wave momentum
P_l'	Dimensionless onshore transport of longshore wave momentum
$\hat{P}_l'$	Corrected estimate of dimensionless onshore transport of longshore wave momentum
$P_{l,fd}'$	Characteristic spectral estimate of P_l'
$\overline{P_{l,fd}'}$	Average frequency-direction spectral estimate of P_l'
$P_{l,fd,k}'$	k^{th} frequency-direction spectral estimate of P_l'
$P_{l,fd,\sigma}'$	Standard deviation of frequency-direction spectral estimate of P_l'

$P'_{i,mon}$	Monochromatic, unidirectional estimate of P'_i
$\overline{P'_{i,mon}}$	Average monochromatic, unidirectional estimate of P'_i
$P'_{i,mon,k}$	k^{th} monochromatic, unidirectional estimate of P'_i
$S(f_n)$	Discrete frequency spectrum
$\overline{S'}(f_n)$	Mean normalized frequency spectrum
$S'_\sigma(f_n)$	Standard deviation frequency spectrum
$S(\theta_m)$	Discrete direction spectrum
$\overline{S'}(\theta_m)$	Mean normalized direction spectrum
$S'_\sigma(\theta_m)$	Standard deviation direction spectrum
$S(f_n,\theta_m)$	Discrete frequency-direction spectrum
$\overline{S'}(f_n,\theta_m)$	Mean normalized frequency-direction spectrum
$S_k(f_n,\theta_m)$	k^{th} constituent frequency-direction spectrum
$S'_k(f_n,\theta_m)$	k^{th} normalized constituent frequency-direction spectrum
$S'_\sigma(f_n,\theta_m)$	Standard deviation frequency-direction spectrum
S_{ij}	General form of radiation stress tensor component
S'_{ij}	General form of dimensionless radiation stress tensor component
$\overline{S'_{ij,fd}}$	Average frequency-direction spectral estimate of S'_{ij}
$S'_{ij,fd}$	Characteristic spectral estimate of S'_{ij}
$S'_{ij,fd,k}$	k^{th} frequency-direction spectral estimate of S'_{ij}
$S'_{ij,fd,\sigma}$	Standard deviation of frequency-direction spectral estimate of S'_{ij}

$S'_{ij,mu}$	Monochromatic, unidirectional estimate of S'_{ij}
$\overline{S'_{ij,mu}}$	Average monochromatic, unidirectional estimate of S'_{ij}
$S'_{ij,mu,k}$	k^{th} monchromatic, unidirectional estimate of S'_{ij}
S_{xx}	Onshore transport of onshore wave momentum
$\hat{S}_{xx}$	Corrected estimate of dimensional onshore transport of onshore wave momentum
S'_{xx}	Dimensionless onshore transport of onshore wave momentum
$\hat{S}'_{xx}$	Corrected estimate of dimensionless onshore transport of onshore wave momentum
$S'_{xx,fd}$	Characteristic spectral estimate of S'_{xx}
$\overline{S'_{xx,fd}}$	Average frequency-direction spectral estimate of S'_{xx}
$S'_{xx,fd,k}$	k^{th} frequency-direction spectral estimate of S'_{xx}
$S'_{xx,fd,\sigma}$	Standard deviation of frequency-direction spectral estimate of S'_{xx}
$\overline{S'_{xx,mu}}$	Average monochromatic, unidirectional estimate of S'_{xx}
$S'_{xx,mu,k}$	k^{th} monochromatic, unidirectional estimate of S'_{xx}
S_{xy}	Onshore transport of longshore wave momentum
$\hat{S}_{xy}$	Corrected estimate of dimensional onshore transport of longshore wave momentum
S'_{xy}	Dimensionless onshore transport of longshore wave momentum
$\hat{S}'_{xy}$	Corrected estimate of dimensionless onshore transport of longshore wave momentum
$S'_{xy,fd}$	Characteristic spectral estimate of S'_{xy}

$\overline{S'_{xy,fd}}$	Average frequency-direction spectral estimate of S'_{xy}
$S'_{xy,fd,k}$	k^{th} frequency-direction spectral estimate of S'_{xy}
$S'_{xy,fd,\sigma}$	Standard deviation of frequency-direction spectral estimate of S'_{xy}
$\overline{S'_{xy,mm}}$	Average monochromatic, unidirectional estimate of S'_{xy}
S_{yy}	Alongshore transport of longshore wave momentum
$\hat{S}_{yy}$	Corrected estimate of dimensional alongshore transport of longshore wave momentum
S'_{yy}	Dimensionless alongshore transport of longshore wave momentum
$\hat{S}'_{yy}$	Corrected estimate of dimensionless alongshore transport of longshore wave momentum
$S'_{yy,ch}$	Characteristic spectral estimate of S'_{yy}
$\overline{S'_{yy,fd}}$	Average frequency-direction spectral estimate of S'_{yy}
$S'_{yy,fd,k}$	k^{th} frequency-direction spectral estimate of S'_{yy}
$S'_{yy,fd,\sigma}$	Standard deviation of frequency-direction spectral estimate of S'_{yy}
$\overline{S'_{yy,mm}}$	Average monochromatic, unidirectional estimate of S'_{yy}
$S'_{yy,mm,k}$	k^{th} monochromatic, unidirectional estimate of S'_{yy}
S_{11}	Alternate form for S_{xx}
S'_{11}	Alternate form for S'_{xx}
S_{12}	Alternate form for S_{xy}
S_{21}	Alternate form for S_{yx}, equal to S_{12}
S_{22}	Alternate form for S_{yy}

S'_{zz}	Alternate form for S'_{yy}
V_σ	Volume of standard deviation frequency-direction spectrum
W_{ij}	Dimensionless weighting function in radiation stress definition
δ_{ij}	Kronecker delta function
Δf	Discrete frequency bandwidth
$\Delta\theta$	Discrete direction arc
ρ	Water density
σ	Standard deviation
σ^2	Variance
σ_k^2	Variance represented by k^{th} constituent spectrum
θ	Generic direction variable representing an angle measured counterclockwise from shore normal
θ_m	m^{th} discrete direction
θ_p	Characteristic peak direction
$\theta_{p,k}$	Characteristic peak direction of k^{th} constituent spectrum

REPORT DOCUMENTATION PAGE

Form Approved
OMB No 0704-0188

1. AGENCY USE ONLY (Leave blank)	2. REPORT DATE	3. REPORT TYPE AND DATES COVERED
	January 1994	Final report

4. TITLE AND SUBTITLE
Three-Parameter Characterization of Shallow-Water Directional Wind Wave Spectra

5. FUNDING NUMBERS

6. AUTHOR(S)
Charles E. Long

7. PERFORMING ORGANIZATION NAME(S) AND ADDRESS(ES)
U.S. Army Engineer Waterways Experiment Station
Coastal Engineering Research Center
3909 Halls Ferry Road
Vicksburg, MS 39180-6199

8. PERFORMING ORGANIZATION REPORT NUMBER

9. SPONSORING/MONITORING AGENCY NAME(S) AND ADDRESS(ES)
U.S. Army Corps of Engineers
Washington, DC 20314-1000

10. SPONSORING/MONITORING AGENCY REPORT NUMBER
Technical Report CERC-94-1

11. SUPPLEMENTARY NOTES
Available from National Technical Information Service, 5285 Port Royal Road, Springfield, VA 22161.

12a. DISTRIBUTION/AVAILABILITY STATEMENT
Approved for public release; distribution is unlimited.

12b. DISTRIBUTION CODE

13. ABSTRACT *(Maximum 200 words)*

A 5-year, 6,759-case database of high resolution, shallow-water, frequency-direction spectra is examined by classifying spectra in discrete ranges of three parameters: characteristic wave height, spectral peak frequency, and spectral peak direction. Counting the number of cases in each classification reveals the distribution of the spectral population in the three-parameter domain. Averaging spectra within parametric classes defines characteristic spectra that can be used to describe nearshore wave conditions more completely when only three paramters are known or estimated. Though the resluts are specifically unique to the North Carolina outer banks experiment site (the Field Research Facility of the U.S. Army Engineer Waterways Experiment Station Coastal Engineering Research Center), they are illustrative of the variability of wave energy distributions possible in nature. Computation of longshore energy fluxes and radiation stress tensor components using characteristic spectra and the three-parameter guidance of the *Shore Protection Manual* reveals significant differences, and suggests that the ability to measure directional distributions of wave energy with high resolution is critical to the further improvement of modeling and predictive ability.

14. SUBJECT TERMS
Energy flux
Frequency-direction spectra
Radiation stress
Wave climate
Wave database
Wind waves

15. NUMBER OF PAGES
129

16. PRICE CODE

17. SECURITY CLASSIFICATION OF REPORT	18. SECURITY CLASSIFICATION OF THIS PAGE	19. SECURITY CLASSIFICATION OF ABSTRACT	20. LIMITATION OF ABSTRACT
UNCLASSIFIED	UNCLASSIFIED		